



Australian
National
University

**Multiscale study of the properties of hybrid
laser-welded Al-Mg-Si alloy joints**

By

Shaohua Yan

A thesis submitted for the degree of

Doctor of Philosophy

of The Australian National University

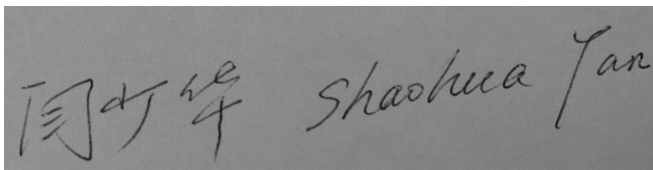
10th January 2019

© Copyright by Shaohua Yan

All Rights Reserved

Declaration

I hereby declare that this is completely my own work finished in the College of Engineering and Computer Science, The Australian National University, Acton, Australia. The content of this thesis has not been used or submitted in other universities or institutions for the reward of degree. It contains no materials that have been previously published or written by others except for the references appropriately acknowledged.

A rectangular image showing a handwritten signature. On the left, the Chinese characters '闫少华' are written in black ink. To the right of the Chinese characters, the name 'Shaohua Yan' is written in a cursive, handwritten style in black ink.

Signed

Shaohua Yan

January 2019

Dedication

To my family for their love and support

Acknowledgement

I would like to thank my supervisor Prof. Qinghua Qin for his knowledge, his generous guidance, and his encouragement. In these four years, I grew up from an infant in research to an adult under his selfless support. Your passion on the research will always drive me to go further in the academy. I also owe big thanks to my secondary supervisors, Dr. Yi Xiao, Dr. Li Li, and Dr. Shankar Kalyanasundaram. Without your help, I could not have finished my PhD research. I would like to take this opportunity to thank my supervisor in my Master study, Prof. Hui Chen of Southwest Jiaotong University. Without his support in my Master study, this PhD adventure would not have come true.

I am grateful for help from the members of the Advanced Materials Group. With you all, I could always get the feeling of sweet home. Special thanks to Dr. Bobin Xing and Dr. Haiyang Zhou. My research could not be carried out without talks and suggestions from you two.

I am grateful for help from members of Prof. Jodie Bradby's group in the Research School of Physics and Engineering, especially Larissa Houston. She taught me how to use the nanoindenter and how to conduct the microscale study.

I am grateful for support from the Centre for Advanced Microscopy and the Australian National Fabrication Facility ACT Node, especially Dr. Hua Chen, Dr. Felipe Kelmer.

I would like to thank lunch-time soccer at ANU. Whenever I was upset or tired in my research, playing soccer with you all could give me so much fun. And thank the singer Lei Zhao, listening to your songs could always inspire me to carry on no matter how upset I was.

Lastly, a million thanks to my parents for these years of support in my study. I owe great thanks to my wife, Yuan Nie, for your generous support in the uncertain adventure of life. Thank you for bringing me such a lovely daughter. You all make my life colourful and lovely.

I would like to acknowledge the financial support from China Scholarship Council and the beautiful country Australia.

Supervisor panel

Prof. Qinghua Qin, The Australian National University, Primary Supervisor and Chair

Dr. Yi Xiao, The Australian National University, Associate Supervisor

Dr. Li Li, The Australian National University, Associate Supervisor

Dr. Shankar Kalyanasundaram, The Australian National University, Associate Supervisor

Abstract

Hybrid laser welding has been increasingly used in joining aluminium alloys. Due to the nature of hybrid laser welding, the welded joint made from Al alloys typically fractures in the fusion zone, indicating that the fusion zone is the softest part of the joint. Thus, modifying the microstructure in the fusion zone and analysing the according mechanical properties is both academically and industrially of interest. In the first part of this research, it was focused on altering the microstructure of the fusion zone using two different filling materials, Al-Mg alloys and Al-Si alloys. The results showed that the mechanical properties of joints with Al-Si as filling material were stronger since the fusion zone features with smaller grain size and multiple-alloys solid solution. However, the fatigue properties and corrosion resistance of joints with Al-Si as filling material were weaker. The reason for such a distinct difference was investigated via theoretical calculation and fracture mechanism. The microstructure-properties relationship of hybrid laser welded AA6061 joints at macroscale was well understood through this research.

Motivated by understanding the mechanical properties at multiscale, the nano/microscale deformation of a single crystal of the fusion zone was investigated via pillar compression tests. These experiments showed that the strength of the fusion zone with Al-Mg as filling material was size-dependent, showing a “smaller is stronger” trend. Such size-dependent strength disappeared when the pillar’s diameter was greater than 3.3 μm . A theoretical model was built and used to analyse the observed size-dependent strength. Interestingly, the strength of the single crystal of the fusion zone with Al-Si as filling material was not size-dependent. Strong solid-solution effect was proposed for this unusual size effect according to theoretical calculation. With increasing dislocation densities, the size- and orientation-dependent strength for pillars in both FZs disappeared. A theoretical model was proposed to quantitatively

analyse the effect of solute elements, dislocation density, and size on the strength of pillars in FZs.

To link the microplasticity with macroscale plasticity, crystal plasticity finite element (CPFE) simulation was conducted. Firstly, microscale-mechanical-properties prediction of single crystals was applied to prove the validity and obtain the material parameters of CPFE simulation. Then, CPFE was successfully utilized to simulate the mechanical properties of the welded joint at macroscale based on the microplasticity obtained by the pillar compression at microscale.

Contents

Declaration.....	I
Dedication.....	II
Acknowledgement.....	III
Supervisor panel.....	V
Abstract.....	VI
Contents.....	VIII
List of Tables.....	XIII
List of Figures.....	XIV
Acronyms.....	XXIII
Chapter 1 Introduction and literature review.....	1
1.1 Introduction.....	1
1. 2. Literature review.....	3
1.2.1 Hybrid laser welding of Al alloys.....	3
1.2.2 Plasticity of the local zone.....	9
1.2.3 Crystal plasticity finite element simulation.....	14
1.2.4 Microscale testing.....	17
1.3 Motivation of this research.....	22
1.4 Outline of this thesis.....	23

Chapter 2 Effect of filling materials on the microstructure and mechanical properties of hybrid laser-welded Al-Mg-Si alloy joints	26
2.1 Introduction	26
2.2 Experimental methods.....	26
2.2.1 Hybrid laser welding	26
2.2.2 Sample preparation	28
2.2.3 Microstructure characterization	29
2.2.4 Property characterization at macroscale	30
2.3. Results	32
2.3.1 Microstructure of the joint	32
2.3.2 EBSD results of the joint	36
2.3.3 Microhardness and mechanical properties of the joint.....	39
2.3.4 Fatigue properties of the joint.....	43
2.3.5 Corrosion resistance of the joint.....	45
2.4. Discussion	48
2.4.1 Microstructure and strength model.....	48
2.4.2 Fatigue and corrosion properties	53
2.4.3 Selection of the filling materials.....	56
2.5 Conclusions	57
Chapter 3 Crystal plasticity of fusion zone in ER5 joint at microscale	59
3.1 Introduction	59
3.2. Experimental and simulation methods	59

3.2.1 Sample preparation	59
3.2.2 Microstructure characterization	61
3.2.3 Compression test.....	61
3.2.4 Molecular dynamic simulation	63
3.3. Results	64
3.3.1 Microstructure analysis of the FZ of bulk samples	64
3.3.2 Micropillar compression.....	66
3.3.3 Dislocation behaviour.....	69
3.3.4 Molecular dynamic simulation	71
3.4. Discussion	73
3.4.1 Orientation effect.....	73
3.4.2 Flow strength	74
3.4.3 Strength from micropillar to bulk.....	77
3.5. Conclusions	79
 Chapter 4 Microstructure versus size: nano/microscale deformation of FZ via pillar compression tests	
4.1 Introduction	81
4.2 Experimental and simulation methods	82
4.2.1 Experimental methods	82
4.2.3 Simulation methods	85
4.3 Results	86
4.3.1 Micropillar compression for the pillars without pre-deformation	86

4.3.2 Dislocation behaviour.....	88
4.3.3 Micropillar compression for pillars with pre-deformation	92
4.3.4 MD simulation results	94
4.4 Discussion	97
4.4.1 Effect of alloying on the size effect and strength	97
4.4.2 Effect of dislocation density	98
4.4.3 Possible mechanisms controlling the deformation	101
4.5 Conclusions	103
Chapter 5 Bridging the gap between microscale and macroscale deformation of the hybrid laser-welded Al alloy joints: experiment and simulation	105
5.1 Introduction	105
5.2 Methodology	105
5.3 Results	109
5.3.1 CPFÉ simulation on the single crystal of the ER5 pillar	109
5.3.2 CPFÉ simulation on the single crystal of ER4 pillar	113
5.3.3 CPFÉ on the compressive deformation behaviour of polycrystals.....	114
5.3.4 CPFÉ on the tensile deformation behaviour of polycrystals	116
5.4 Discussion	117
5.5 Conclusions	119
Chapter 6 Summary and outlook of this research	120
6.1 Summary of this thesis	120
6.1.1 Macroscale study of the microstructure and properties	120

6.1.2 Nano/microscale study of the plasticity of the fusion zone.....	121
6.1.3 Predicting plasticity from microscale to macroscale.....	123
6.2 Highlights.....	123
6.3 Future works.....	124
Bibliography	126
List of publications	149

List of Tables

Table 1-1 Comparison of arc welding, laser welding and hybrid laser welding [7].....	2
Table 1-2 Summary of the mechanical test results from the literature	7
Table 2-1 Chemical compositions of the base metal and filling materials (wt.%).....	26
Table 2-2 Details of the hybrid laser welding system used in this study.....	27
Table 2-3 Parameters for hybrid laser welding AA6061-T6 with different filling materials..	27
Table 2-4 Procedures for grinding and polishing samples.....	29
Table 2-5 KAM and dislocation density for both welds obtained from EBSD testing.	39
Table 2-6 Corrosion properties estimated from polarization curve.	47
Table 2-7 Measured properties from SSRT and Psc.	47
Table 2-8 Input parameters for the strength model.....	53
Table 2-9 Summary of the main results from manufacturing to properties in this paper.....	57
Table 4-1 Summary of crystallographic data of the selected grains.....	84
Table 4-2 Information of pre-deformed pillars machined from original larger pillars.....	93
Table 5-1 Material parameters used in ER5 pillar for crystal plasticity finite element simulation. The unit of C_{11} , C_{12} , C_{44} is GPa, of g_0 , g_∞ , and h_0 is MPa, and of γ_0 is s^{-1}	111
Table 5-2 Yield strength obtained from simulation the experiment for ER5 joints, the unit is MPa.	111
Table 5-3 Material parameters used in ER4 pillar for crystal plasticity finite element simulation. The unit of C_{11} , C_{12} , C_{44} is GPa, g_0 , g_∞ , and h_0 is MPa, and γ_0 is s^{-1}	114

List of Figures

Figure 1-1 Scheme of hybrid laser welding [10].	4
Figure 1-2 Effect of parameters on the porosity in a hybrid laser-welded AA6082 joint [12]..	6
Figure 1-3 Scheme for the mechanism that prevents porosity formation by increasing the arc current [14].....	6
Figure 1-4 (a) Nominal stress–displacement curve for the welded joint; (b) strain distribution measured by digital image correlation at three stages of the test as defined in (a) [41].....	10
Figure 1-5 Micro-hardness of the MIG welded joint and laser-MIG welded joint [16].....	12
Figure 1-6 (a) Position of the micro-tensile samples with respect to the fusion zone; (b) nominal stress–strain curves for the micro-tensile samples in the different zones of the weld assembly [41].....	13
Figure 1-7 Principle of the integrated chain modelling applied to a friction stir weld made of a 6005 Al alloy with the advancing speed of 1000 mm/min and the rotational speed of 1000 rpm. [51]	14
Figure 1-8 Scheme of the conceptual ingredients in CPFEM simulation. (a) case of one phase with dislocation as the deformation mechanism, (b) case of several phases, multiple orientations and two deformation mechanisms (dislocation and twinning). [60].....	16
Figure 1-9 (a) Cylindrical pillar machined by FIB, (b) scheme of compression test with a flat diamond punch, (c) stress-strain curves, (d) deformed morphology of the pillar [69].....	17

Figure 1-10 Shear flow stress normalized by shear modulus on appropriate slip system for most face-centred cubic (fcc) metallic micro- and nano-pillars tested in compression and tension to date [72]..... 18

Figure 1-11 In-situ TEM compression test on a <111>-oriented 160 nm-top-diameter Ni pillar, (a) high-dislocation-density pillar before compression, (b) dislocation-free pillar after the first compression, (c) after the second compression, (d) displacement-force curves for the first compression, (e) displacement-force curves for the second compression, (f) displacement-stress curves for two compression tests [78].21

Figure 1-12 (a) Dislocation-starvation state in Al crystal after 128 cycles, (b) plastic strain-stress for the Al crystals in as-fabricated state and dislocation-free state [79].....21

Figure 1-13 (a) Scheme of double-ended dislocation source turning into single-ended dislocation source, (b) distribution of single-ended dislocation sources in a finite sample [77].22

Figure 2-1 Hybrid laser welding system used in this study [16].28

Figure 2-2 The weld appearance and X-ray detected images of the ER4043 and ER5356 joint under optimized welding parameters.28

Figure 2-3 Schematic for the setup of the SSRT.31

Figure 2-4 Dimensions of the test sample used in the slow strain rate test, the thickness of the sample was 3.8 mm.32

Figure 2-5 Optical images of the hybrid laser-welded joint with ER5356 filling material, (a) centre of fusion zone, (b)overview of the fusion line between the HAZ and FZ, (c) HAZ, (d)equiaxed grains in the HAZ close to the fusion line, (e) base metal.34

Figure 2-6 Optical images of the hybrid laser-welded joint with ER4043 filling material, (a) overview of the microstructure near the fusion line, (b) the microstructure in the FZ, (c) the microstructure in the HAZ.35

Figure 2-7 SEM images and EDS results of the hybrid laser-welded joint. (a) overview of the FZ in the joint with ER5356 filling material, (b) enlarged view of the precipitates, and (c) the EDS results of the precipitates; (d) overview of the FZ in the joint with ER4043 filling material, (e) enlarged view of the precipitates, and (f) the EDS results of the precipitates. ...36

Figure 2-8. IPF images of the hybrid laser-welded joint, (a) FZ of the ER5356 joint, (b) HAZ of the ER5356 joint, (c) BM of the ER5356 joint, (d) FZ of the ER4043 joint, (e) HAZ of the ER4043 joint.38

Figure 2-9. (a) (c) (e) Pole figures of FZ, HAZ, and BM of the ER5356 joint, (b) and (d) pole figures of FZ and HAZ of the ER4043 joint.38

Figure 2-10 KAM maps of (a) FZ of the ER5356 joint, (b) FZ of the ER4043 joint, and (c) distribution of KAM of two different joints.39

Figure 2-11 Hardness profile of the welded joint with two different filling materials.....41

Figure 2-12 (a) Tensile stress-strain curves of ER5356 joint, ER4043 joint and the BM, (b) tensile strength and yield strength of the tested samples, (c)-(d) representative cross-section images of the fractured tensile test sample for ER5356 joint and ER4043 joint.41

Figure 2-13 Macroscopic view of the fracture of the tested sample after tensile tests, (a) the ER5356 joint, (b) the ER4043 joint.42

Figure 2-14 SEM observation on the fractured surface of (a) the ER5356 joint, (b) the ER4043 joint, and (c) the BM.....43

Figure 2-15 (a) S-N curves of the ER5356 joint and the ER4043 joint, (b) representative cross-section image of the fractured fatigue test sample for the ER5356 joint, (c) representative cross-section image of the fractured fatigue test sample for the ER4043 joint.44

Figure 2-16 Fatigue fracture of ER5356 joint, (a)~(b) crack initiation from pores, (c) striation during the propagation period, (d) fracture period.....45

Figure 2-17 Fatigue fracture of the ER4043 joint, (a)~(d) crack initiation from pores close to the surface, (e) striation during the propagation period, (d) fracture period.....45

Figure 2-18 Corrosion test results of the welded joint, (a) polarization curves, (b) and (c) stress-strain curves of the ER5356 joint and the ER4043 joint in SSRT, respectively.47

Figure 2-19 Predicted strength from the strength model from each considered strengthening mechanism.52

Figure 3-1 Procedure for TEM sample preparation using FIB.61

Figure 3-2 (a) Top view of a pillar under optical microscope in the nanoindenter, (b) flat-end punch for the compression test.62

Figure 3-3 Figures showing the sample bent instead of compressed during nanoindentation.63

Figure 3-4 Nanopillar for MD simulation.....64

Figure 3-5 (a) SEM image of the microstructure of the FZ, (b) EDS results for the areas indicated in (b) with white boxes.....65

Figure 3-6 TEM images for the bulk in the FZ, (a) coarsened phases, (b) fine phases in the area indicated in (a) by a red circle.....65

Figure 3-7 EBSD test results for the FZ, (a) IPF image, (b) KAM image, (c) PF image [22].66

Figure 3-8 Representative images of the pillars after compression, (a) 800 nm-diameter pillar with orientation [101], (b) 6.8 μm -diameter pillar with orientation [101], (c) 800 nm-diameter pillar with orientation [111], (d) 6.8 μm -diameter pillar with orientation [111].68

Figure 3-9 Representative stress-strain curves of (a) [101]-oriented pillars and (b) [111]-oriented pillars; (c) yield strength vs. diameter for the tested pillars with different orientations, (d) hardening angle vs. pillar diameter for the tested orientation.69

Figure 3-10 (a) Indication of TEM sample machined by FIB, (b) overview of the strained area (dark line), (c) Ga⁺ damaged zone, (d)-(g) dislocation and lattice distortion in the deformed pillar.70

Figure 3-11 (a) Indication of the TEM sample machined by FIB, (b) overview of the strained area (bright areas), (c)-(d) dislocations in the deformed area as indicated in (b) by red circles.71

Figure 3-12 MD simulation results, (a) stress-strain curves for orientations [101] and [111], (b) dislocation density during compression, (c) snapshot of microstructure evolution in the [101]-oriented sample under compression, (d) snapshot of microstructure evolution in the [111]-oriented sample under compression.72

Figure 3-13 Calculated critical shear stress according to Eq. 3-15 for (a) orientation [101] and (b) orientation [111]. The red points are the calculated CRSS, while the black points are the experimental ones. The contribution to the strength from τ_{source} , τ_{ss} , and τ_{d} is illustrated by green, magenta and blue dashed lines, respectively. (c) The normalized strength vs. normalized diameter for the tested pillars in this study, (d) yield strength vs. diameter for orientations [101] and [111].77

Figure 4-1 (a) (b) Selected orientations for pillar machining in the FZ of the ER4 joint, (c) selected orientations for the pillar machining in the FZ of the ER5 joint.....84

Figure 4-2 Model for molecular dynamic simulation for Al-Mg-Si alloys.86

Figure 4-3. Morphology of deformed pillars taken from the FZ of ER4 joint, (a)-(c) are 800 nm-diameter pillars with orientations of [101], [111], and [312]; (d)-(g) are 2000 nm-diameter pillars with orientations of [101], [111], [312], and [532].....87

Figure 4-4 (a) Representative stress-strain curves for [101]-oriented pillars taken from the FZ of ER4 joint, (b) Representative stress-strain curves for [111]-oriented pillars taken from the FZ of ER4 joint; (c) Yield stress vs. diameter for pillars taken from the FZ of ER4 and ER5 joint, respectively; (d) Normalized strength vs. normalized diameter for pillars taken from FZ of ER4 joint, respectively.88

Figure 4-5. TEM results for the [111]-orientated 800 nm-diameter pillars taken from the FZ of the ER4 joint, (a) overview of the deformed pillar, (b) dislocation structure near the slip offset as indicated in (a) with a square, (c) enlarged view of the site indicated in (b), (d) dislocation structure near the top of the pillar.90

Figure 4-6. TEM results for [101]-oriented pillars taken from the FZ of the ER4 joint, (a) overview for the 800 nm-diameter pillar, (b) dislocation structure near the top of the 800 nm-diameter pillar, (c) dislocation structure near the slip offset for the 2000 nm-diameter pillar, (d) enlarged view of the dislocation structure of the site indicated in (c).....91

Figure 4-7. (a) Dislocation density for pillars of the FZ taken from the ER4 joint, (b) dislocation density for pillars of the FZ taken from the ER5 joint.91

Figure 4-8. Procedure for making pillars from deformed larger pillars, (a) deformed 5.2 μ m-diameter ER5 pillar, (b) 3.2 μ m-diameter pillar made from deformed 5.2 μ m-diameter ER5 pillar, (c) deformed morphology of the pre-deformed 3.2 μ m-diameter pillar; (d) deformed 3.2 μ m-diameter ER4 pillar, (e) 2.3 μ m-diameter pillar made from deformed 3.2 μ m-diameter ER4 pillar, (f) deformed morphology of the pre-deformed 2.3 μ m-diameter pillar.93

Figure 4-9. (a) Representative stress-strain curves for previously deformed pillars taken from the FZ of the ER5 joint, (b) Normalized strength vs. normalized diameter for pre-deformed pillars taken from the FZ of the ER5 joint, (c) yield stress vs. diameter for pre-deformed pillars taken from the FZ of the ER5 joint; (d) representative stress-strain curves for pre-deformed pillars taken from the FZ of the ER4 joint, (e) yield stress vs. diameter for pre-deformed pillars taken from the FZ of the ER4 joint.....94

Figure 4-10 (a) Stress-strain curves from MD simulation for samples without initial dislocation density, (b) stress-strain curves from MD simulation for samples with initial dislocation density, (c) dislocation density evolution during compression.95

Figure 4-11 (a)-(c) Dislocation density evolution for [110]-oriented sample under different strains, (d) deformed morphology from experiment and simulation, (e) indication for dislocation types.....96

Figure 4-12 (a)-(e) Dislocation density evolution for [111]-oriented sample under different strains, (f) deformed morphology from experiment and simulation.....96

Figure 4-13 (a) Yield stress vs. diameter for the present study and Refs. [42, 168, 172], (b) effect of alloying and sample size on the yield stress of Al-based alloys (data from present study and Refs. [42, 168, 170-172]).98

Figure 4-14 Yield stress for ER4 pillars and ER5 pillars with and without pre-deformation.	101
Figure 4-15. (a) Diameter vs. τ_{CRSS} from experimental results and theoretical model for ER5 and pre-deformed ER5 pillars, (b) Diameter vs. τ_{CRSS} from experimental results and theoretical model for ER4 and pre-deformed ER4 pillars. The contribution to the strength from τ_{source} , τ_{ss} , and τ_{taylor} is illustrated by green, magenta and cyan dashed lines, respectively. For the pre-deformed pillars, the contribution to the strength from τ_{source} is illustrated by navy lines.	103
Figure 5-1 (a) High-speed train body made of aluminium alloys, (b) AA6061 welded by hybrid laser welding, (c) EBSD characterization of the cross-section of the FZ, (d) SC compression testing for the selected grain in (c), (e) dislocation-based mechanism, (f) CPFE employed to simulate the stress-strain curves for SC and polycrystal of the weld.....	108
Figure 5-2 CPFE simulation model of single crystal.....	109
Figure 5-3 Procedure for determining the material parameters used in CPFE simulation. ...	111
Figure 5-4 Stress-strain curves from both simulation and experiment for the orientation of (a) [101], (b) [111], (c) [-301], and (d) [101]-oriented 400nm-diameter sample.....	112
Figure 5-5 Von Mises stress of orientation (a) [101], (b) [111], (c) [-301]; SEM images for the deformed pillar of orientation (d) [101], (e) [111], and (f) [-301].	112
Figure 5-6 Stress-strain curves from both simulation and experiment for the orientation of (a) [10-1], (b) [111], (c) [31-2].	113
Figure 5-7 Von Mises stress and SEM images of the deformed morphology of orientation (a) [10-1], (b) [111], (c) [31-2].	114

Figure 5-8. (a) Polycrystal model for CPFÉ simulation, (b) results from the macro-mechanical model and experiments, (c) stress distribution in the model at the final tested strains..... 115

Figure 5-9 (a) CPFÉ polycrystal model for tensile test of the ER5 joint, (b) tensile stress-strain curves from experiment and simulation with the yield stress showing in the image, (c) Von Mises stress distribution after 5% strain in CPFÉ simulation..... 117

Figure 5-10 (a) Tensile stress-strain curves from experiment and simulation with the yield stress shown in the image, (c) Von Mises stress distribution after 5% strain in CPFÉ simulation..... 117

Acronyms

MIG Metal Inert Gas

TIG Tungsten Inert Gas

FZ Fusion Zone

PWHT Post Weld Heat Treatment

CPFE Crystal Plasticity Finite Element

FCC Face Centred Cubic

BCC Body Centred Cubic

SC Single Crystal

FIB Focused Ion Beam

CRSS Critical Resolved Shear Stress

BM Base Metal

AA Aluminium Alloy

EBSD Electron Back Scatter Diffraction

PIPS Precision Ion Polishing System

FESEM Field Emission Scanning Electron Microscope

TEM Transmission Electron Microscope

EDS Energy Dispersive Spectroscopy

EDM Electron Discharge Machining

SSRT Slow Strain Rate Test

KAM Kernel Average Misorientation

SCC Stress Strain Cracking

MD Molecular Dynamic

LAMMPS Largescale Atomic/Molecular Massively Parallel Simulator

CNA Common Neighbour Analysis

DXA Dislocation Extraction Algorithm

Chapter 1 Introduction and literature review

1.1 Introduction

Aluminium alloys and thin metal sheets [1-5] have found increasing usage in the structures of aircraft, high-speed train and automobiles. In the manufacturing process of these structures, welding is a primary choice due to its high efficiency and low cost. The commonly used welding process is fusion welding, such as metal inert gas (MIG) welding and tungsten inert gas (TIG) welding. As fusion welding may induce high heat input due to the low-density heat source, welded joints, especially made of heat-treatable aluminium alloys, have problems of high residual tensile stress, distortion, a wide heat affected zone, and poor mechanical properties. To obtain a desired welded Al alloys joint, high-density heat sources are usually needed.

It is worth noting that laser welding is considered an ideal welding method for joining aluminium alloys since its light energy can focus on a small spot and consequently induce key-hole welding. The fusion zone and heat affected zone in the laser-welded joint are therefore narrow, leading to a welded structure with low residual stress and small distortion. The fast welding process may bring problems of porosity and cracking, which can be detrimental for later in-service life. Also, the bridging ability is not favourable for laser welding. Furthermore, the laser is easily reflected by the aluminium alloys, causing low absorption efficiency.

In 1980, Steen [1] used laser and gas tungsten arc welding to join 3-mm-thick copper. Since then, hybrid laser welding has emerged in the academic and industrial worlds. This advanced welding method fosters the strength of laser welding and arc welding and circumvents the

weakness of both. Hybrid laser welding has been reported to feature high welding speed, good bridging ability, and high penetration [6]. Detailed comparisons of arc welding, laser welding, and hybrid laser welding are shown in Table 1-1 [7]. The resultant joint of hybrid laser welding presents relatively superior mechanical performance. Therefore, it is a preferable processing method for joint aluminium alloys considering from the viewpoint of both environment (less CO₂ emission and energy consuming) and the in-service life (long endurance under external loadings).

Nevertheless, the complex interaction of laser-arc and laser-aluminium alloys, makes accurate modelling of the welding process difficult, leading to difficulties in precisely modelling of the microstructure and mechanical properties. Moreover, the problems of the conventional welding methods (such as MIG and TIG welding) still exist in hybrid laser-welded joints. For example, porosity and cracks are always a concern in hybrid laser welding of Al alloys. How to avoid or minimise these problems while obtaining a sound welded joint is still an open question in both academic and industrial worlds. Besides, how to precisely mimic the performance of hybrid laser-welded Al alloy joints using simulation is still debated.

Table 1-1 Comparison of arc welding, laser welding and hybrid laser welding [7]

	Arc welding	Laser welding	Hybrid laser welding
Gap bridging	Good due to the use of filling materials	Bad	Good
Heat input	High heat input high residual stress and distortion	Low heat input low residual stress and distortion	Low heat input low residual stress and distortion
Cooling rate	Low cooling rate due to high heat input	High cooling rate causing high porosity	Relatively low cooling rate Less porosity
Welding efficiency	Low due to low welding speed	High	High
Welding stability	Unstable arc at higher welding speed	Unstable keyhole leading to porosity	Stable arc and keyhole due to interaction between laser and arc

1. 2. Literature review

1.2.1 Hybrid laser welding of Al alloys

1.2.1.1 Hybrid laser welding

As shown in *Figure 1-1*, a hybrid laser welding system is usually comprised of two welding processes, laser welding and arc welding. Typically used arc welding includes MIG welding and TIG welding. Based on wavelength, laser sources are classified into three major types: YAG laser, CO₂ laser, and fibre laser. A CO₂ laser source has the wavelength of 10.6 μm, which lowers the conversion efficiency. YAG and fibre laser have shorter wavelengths of 1.06 μm and 1.07 μm, respectively.

As can be seen from *Figure 1-1*, the position of the two heat sources is typically paraxially arranged, with the laser source being either in front of or behind the arc source. With the arc source in front, the absorption efficiency of the laser is increased due to the solid material turning into liquid state [8]. With the laser source in front, the porosity of the weld is reduced since the weld is well protected by the shielding gas and bubble has more time to escape from the welding pool. It is reported in Ref. [2] that a weld's quality can be affected by the source's position, which can change the microstructure of the weld regarding porosity, grain size, and loss of alloying elements. The shielding gases are typically applied through an arc welding torch to protect the welds from forming porosity and oxidized contaminations. In some cases, multidirectional shielding gas is given from the coaxial direction. However, the presence of multidirectional shielding gas can make the laser-arc plasma interaction more complex [9], such that the welding stability is reduced. Basically, shielding gas through the arc torch is sufficient to protect the welding pool.

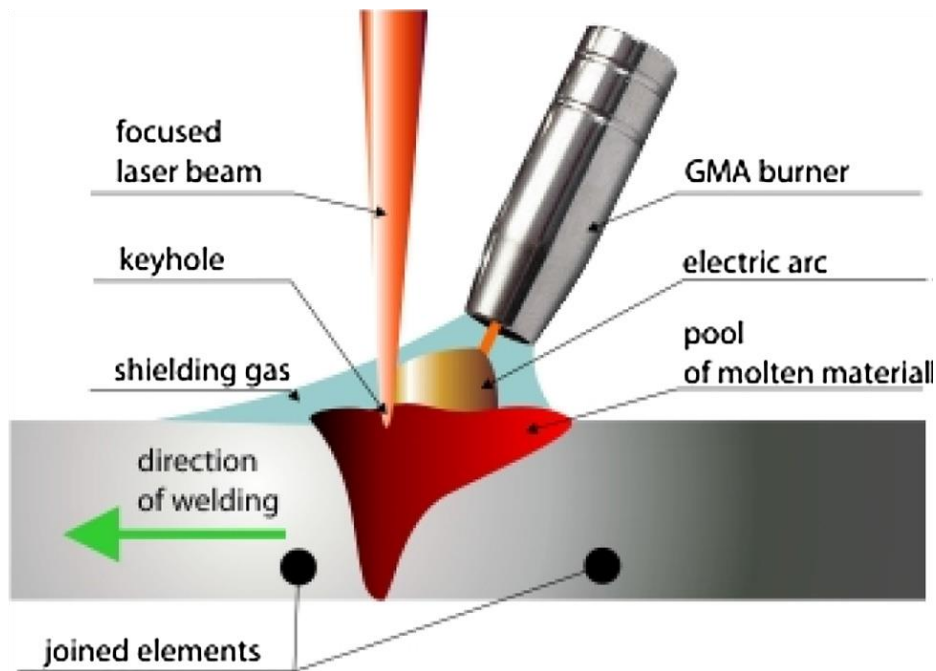


Figure 1-1 Scheme of hybrid laser welding [10].

1.2.1.2 Welding parameters of the hybrid laser welding

The hybrid laser welding process is controlled by many parameters, including the laser power, arc power, welding speed, distance between the arc and laser source, defocus of the laser, and shielding gas. The influence of these parameters is discussed in the review article [10]. It has been reported [11] that cracks were considered a critical problem for high-strength alloys (e.g., AA7xxx and AA2xxx). In contrast, this thesis work focuses on the material AA6xxx only, for which cracking is not the major concern in our experiments. Thus, only the influence of parameters on pores is discussed.

The porosity generated during hybrid laser welding can be attributed to two reasons, (a) the instability of the keyhole that can lead to macroscale pores, and (b) the trapped shielding gas that results in microscale pores. Macroscale pores can reduce the statistic and dynamic strength of the weld, whereas microscale pores can only influence the dynamic strength of the weld. Thus, efforts have been made to stabilize the welding process to avoid the formation of macroscale pores. Zhang et al. [12] studied the effect of the welding parameters arc welding

current, laser power, distance between laser and arc, defocusing amount, and welding speed on the porosity of laser-arc welded AA6082 joint. They reported that porosity could be reduced in many ways, such as increasing the arc welding current and laser powers and reducing the welding speed, as shown in *Figure 1-2*. Bunaziv et al. [13] tried to reduce coarsened porosity in hybrid laser-welded AA5083 joints by adjusting the trailing torch arrangement and the shielding gas. They found that the number of macroscale pores could be largely decreased with the MIG torch as the trailing heat source, and the shielding gas had no effect on the number of large pores. Seiji et al. [14] studied the influence of arc welding current on the porosity of hybrid laser-welded AA5052 joints and found that increasing the arc current reduced the porosity in the weld. Although the parameters used in the literature are different, the reported results indicated that increasing the arc current and decreasing the welding speed could reduce porosity. As shown in *Figure 1-3*, with an increase in the arc current, the ratio of the height to the width of the weld pool decreases. In other words, the distance for the bulb to escape from the surface of the pool is shortened, leading to easier annihilation of the bulb. Besides, slowing the weld speed could allow the bulb more time to move out of the weld pool.

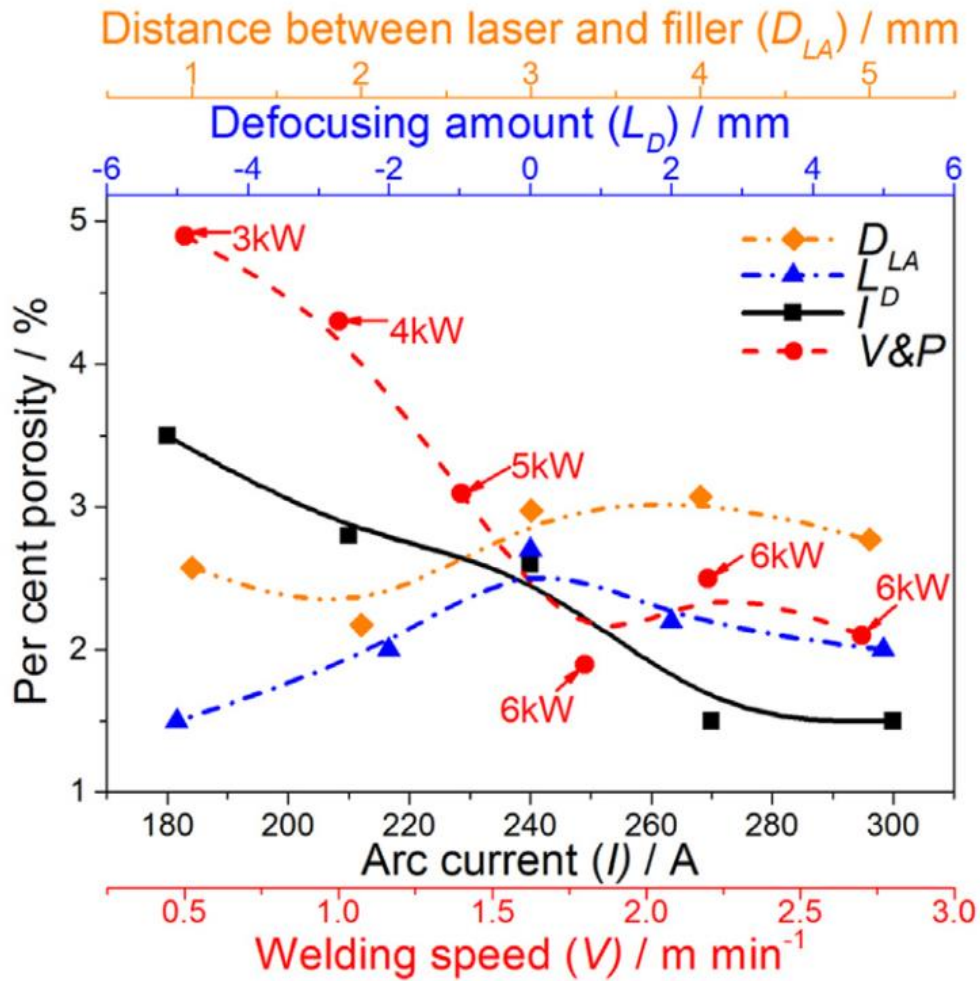


Figure 1-2 Effect of parameters on the porosity in a hybrid laser-welded AA6082 joint [12].

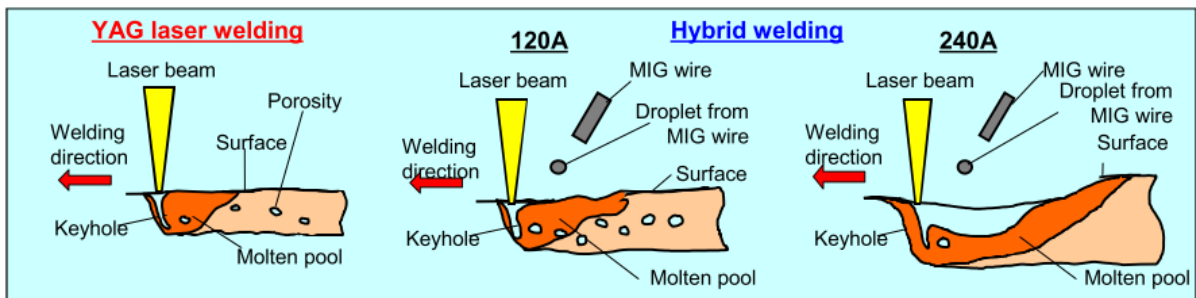


Figure 1-3 Scheme for the mechanism that prevents porosity formation by increasing the arc current [14].

2.1.3 Current problems related to the mechanical properties of hybrid laser welding of Al alloys

Hybrid laser welding is considered an ideal welding method for joining Al alloys. To understand its applicability, extensive efforts have been made to study the welding process,

microstructure, and mechanical properties. The results of these investigations show that problems still exist in this advanced welding process due to its thermal cycles, which are linked to coarse microstructure (precipitates and grain size), defects (cracks and pores), and loss of alloying elements (Mg and Zn) in the joint [2, 13, 15, 16]. Consequently, most samples fractured in the fusion zone (FZ) under tensile tests or fatigue tests [2, 15-21], as shown in *Table 1-2*, which indicates that the FZ is the softest part of the welded joint. It is impossible to eliminate the softening behaviour of the welded joint due to the nature of the fusion welding process. Nevertheless, the performance of welded joints can be improved by tailoring their microstructure.

Table 1-2 Summary of the mechanical test results from the literature

Base metal	Filling metal	Welding methods	Testing methods	Fractured zone	Source
AA5083	ER5183	Laser-MIG	Tensile test	Fusion zone	Ref. [2]
A7075-T6	ER5356	Laser-MIG	Tensile test	Fusion zone	Ref. [15]
AA5083	ER5356	Laser-MIG	Tensile test and fatigue test	Fusion zone	Ref. [16]
AA6005	ER5356	Laser-MIG	Tensile test	Fusion zone	Ref. [6]
AA6061	ER5356 and ER4043	Laser-MIG	Tensile test and fatigue test	Fusion zone	Ref. [22]
AA7N01	ER5356	Laser-MIG	Tensile test	Fusion zone	Ref. [23]
AA2219	ER2325 and ER5087	Laser-MIG	Tensile test	Fusion zone	Ref. [20]

One of the methods to resolve the problems mentioned above is to reduce the defects and evaporation of alloying elements by adjusting parameters of the welding process [2, 24]. Inappropriate welding processes can induce defects of cracks, large pores, and loss of alloying elements, which weaken the performance of the welded joint. Several authors [12, 15, 25, 26] have suggested that adjusting welding parameters, such as welding speed and the laser power/welding current could stabilize the welding process stable to achieve a sound welded joint. Besides the welding parameters, the welding atmosphere, especially the humidity, can also influence the porosity and the mechanical properties of welded joints, as indicated by Gou et al. [27].

Another way of increasing the mechanical properties or corrosion resistance of welded joints is to use post-weld heat treatment (PWHT). PWHT has been widely used to improve the properties of welds produced by TIG welding, friction stir welding, and MIG welding [28-30]. However, very few reports have discussed on the effects of PWHT on the properties of hybrid laser-welded Al alloy joints. Yan et al. [23] were the first to apply PWHT for improving the corrosion properties of hybrid laser-welded AA7N01 joints. The corrosion resistance of the welded joint could be improved through PWHT, but the strength deteriorated. Leo et al. [21] then investigated the role of PWHT on the microstructure and mechanical properties of AA5754 welds joined by hybrid laser welding, and reported that the microhardness and the mechanical properties of the heat-treated sample could be higher than those of the untreated sample.

Few researchers have attempted to modify the alloy composition in the welded joint by altering the filling materials. Zhang et al. [20] studied the microstructure and mechanical properties of hybrid laser-welded AA2219 alloys with the filling materials AlMg₅ and AlCu₇. They found that the higher strength of joints with AlMg₅ depended on two factors, a considerable number of S-Al₂CuMg phases and their pinning effect on the dislocation motion.

Wang et al. [31] investigated the effect of additional Ti and Sr on the microstructure and mechanical properties of AA4043 welding wire and AA6082 joints welded with such wire. They claimed that the tensile strength of the welds with modified wire was significantly improved. It is generally accepted that Al-Si alloys are most suitable for welding of Al-Mg-Si alloys because the ER4043 can maintain good fluidity during welding and thus reduce the proclivity to cracking. Therefore, the welding of Al-Mg-Si alloys in most published research has been finished using Al-Si wire [26, 31-35]. However, Al-Mg-Si alloys are sensitive to corrosion attack due to their higher Si content [36, 37], which means that the high-content-Si welds also corroded easily and thus their life-span was reduced under corrosive environment. Few studies have reported the corrosion resistance of the welds, although the corrosion attack could result in brittle failure and cause catastrophic accidents during service. Actually, sound Al-Mg-Si welds with Al-Mg wire have been obtained without cracks [6, 12]. That finding suggests that the manufacturing process is not a problem for welding of Al-Mg-Si alloys with either filling wire. The questions are what kind of wire should be used when hybrid laser welding of Al-Mg-Si alloys? What criteria should be taken into consideration when selecting the filling materials? More importantly, how would the welded joint maintain the in-service-life related properties unchanged or permit them to change very slowly over a long term (such as fatigue strength and corrosion resistance)?

1.2.2 Plasticity of the local zone

Because of the quick thermal cycles, the microstructure in welded joints is heterogeneous. More specifically, the FZ is filled with coarse microstructures (precipitates and grain size) and lacks alloying elements (Mg and Zn) [2, 13, 15], whereas the HAZ is made of coarsened or dissolved precipitates. The direct outcome of the varied microstructures is the heterogeneous spatial distribution of mechanical properties across the welded joint. Although

the weakest part of the joint is dependent on several factors (such as filling materials and base metal), results in the literature [2, 6, 13, 15, 16, 20, 21, 23, 38-40] show that most of such joints are broken in FZ under tensile testing, which indicates that the weakest part of the hybrid laser-welded Al alloy joints is in the FZ. As suggested by Puydt et al. [41], see *Figure 1-4*, the weakest part of the welded joint could withstand almost all the strains under external loading while other parts remained elastic. Thus, to some extent, the mechanical behaviour of the FZ determines that of the welded joint [41], especially in early-stage plasticity. Knowledge of the plasticity in the softest area in the welded joint is crucial to accurately predicting the mechanical properties of the hybrid laser-welded joint.

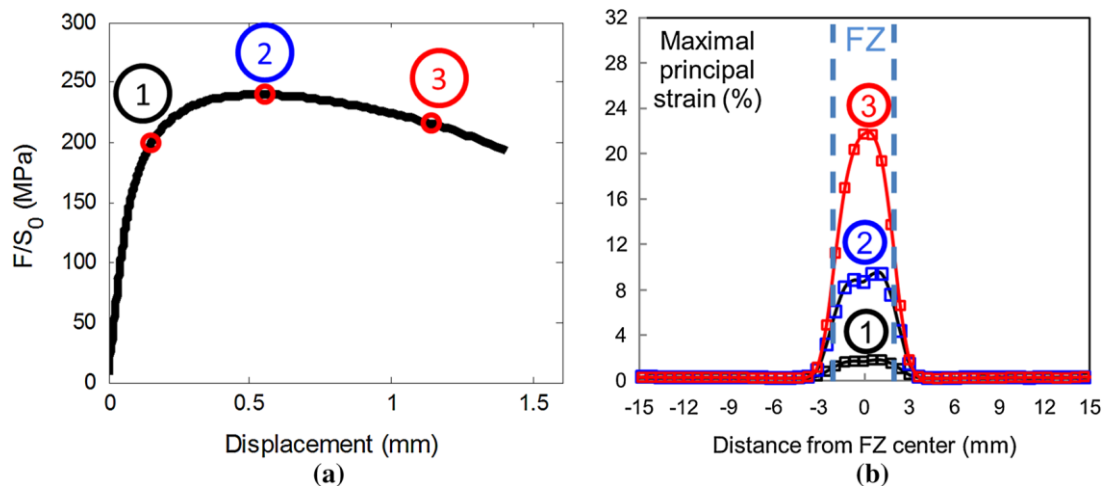


Figure 1-4 (a) Nominal stress–displacement curve for the welded joint; (b) strain distribution measured by digital image correlation at three stages of the test as defined in (a) [41].

The most direct way to obtain plasticity in welded Al alloy joints is the hardness test, as shown in *Figure 1-5*. The hardness in different zones thus can be obtained. The yield stress can be roughly obtained via multiplying the hardness value by 3.3 [42]. The softest zone of the welded joint can be identified by this method. But no information about the stress-strain curves can be derived from this test. Some authors [41] have used micro-tensile tests method, in which the sample's dimension is actually at mm scale, to obtain the stress-strain curves for local zones. As shown in *Figure 1-6*, the sample is taken from the FZ and HAZ along the

thickness direction and then subjected to tensile tests. The stress-strain curves for local zones (see *Figure 1-6b*) can be obtained with this method. Afterwards, numerical methods such as finite element methods [43-48] are employed to simulate the deformation process of the welded joint based on data of the stress-strain curves obtained from micro-tensile test method. The accuracy of this method is influenced by several factors, including the position at which the micro-tensile test sample is conducted, the welding parameters, and the boundary conditions [49]. Moreover, this method can only give the stress-strain data along the welding direction, but the industrially used alloys typically have texture either along or perpendicular to the welding direction. Thus, this test method may not obtain the mechanical properties of the welded joint and predictive ability of this method is limited.

Some authors [49, 50] have tried to predict the plasticity of the welded joint by considering the microstructure evolution and finite element simulation. The best known model is integrated modelling, which consists of several sub-models [51]: a thermal model, a precipitation model, a yield strength and strain hardening model, and a finite element model of a transverse tensile test coupled with a damage model. The principle of this method is shown in *Figure 1-7*. The goal of this model is to predict the mechanical properties of the welded joint from the manufacturing process, so the simulation results can provide feedback to the adjustment of welding parameters for achieving a sound welded joint. By considering the microstructure changes/formation during the welding, this model can predict the microstructure-mechanical relationship with good accuracy. However, there are several limitations for integrated modelling to apply in the hybrid laser-welded Al alloys joint:

- (a) It is difficult to accurately model the hybrid laser welding due to the complex interaction of laser-arc, laser-materials etc. [52], which make it difficult to precisely predict the microstructure formed during welding. As a result, the accuracy of this model is not reliable for the hybrid laser welding process.

(b) The method relies on macro stress-strain curves as the input, but the information about how the microstructure reacts to external loading at the grain/micro scale is yet unknown.

(c) Industrial polycrystalline materials usually have crystalline textures and thus show anisotropic mechanical properties, and the model does not yet tackle this aspect.

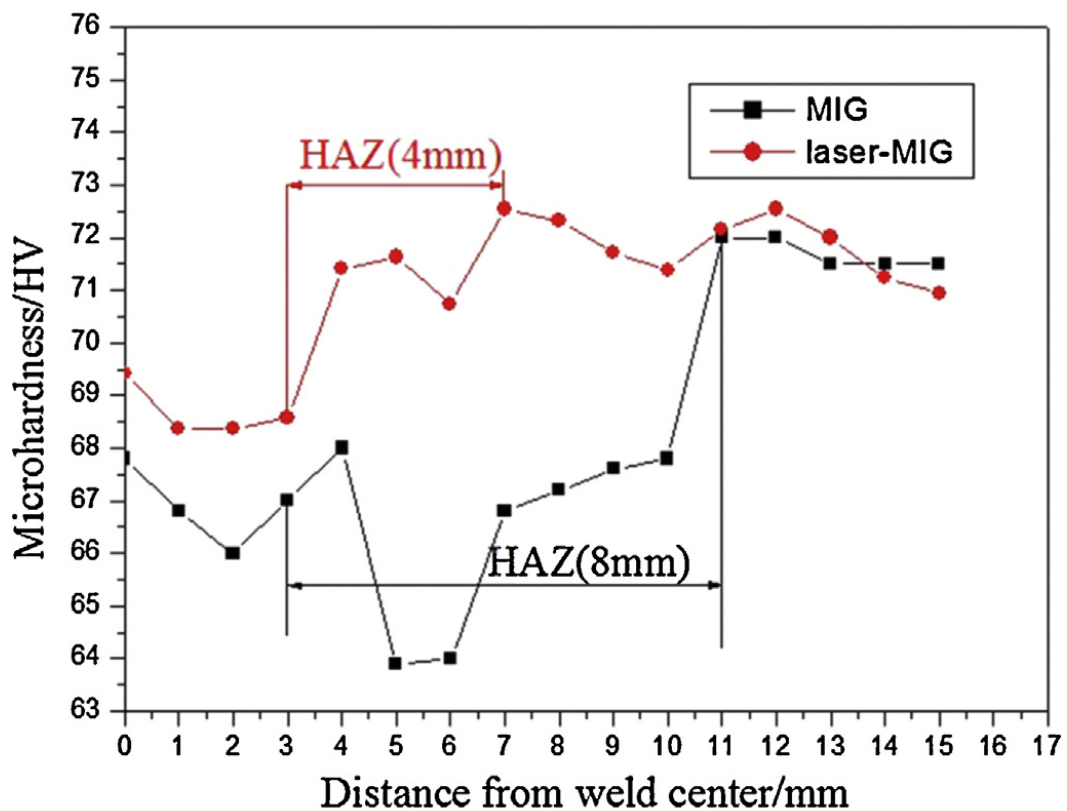


Figure 1-5 Micro-hardness of the MIG welded joint and laser-MIG welded joint [16].

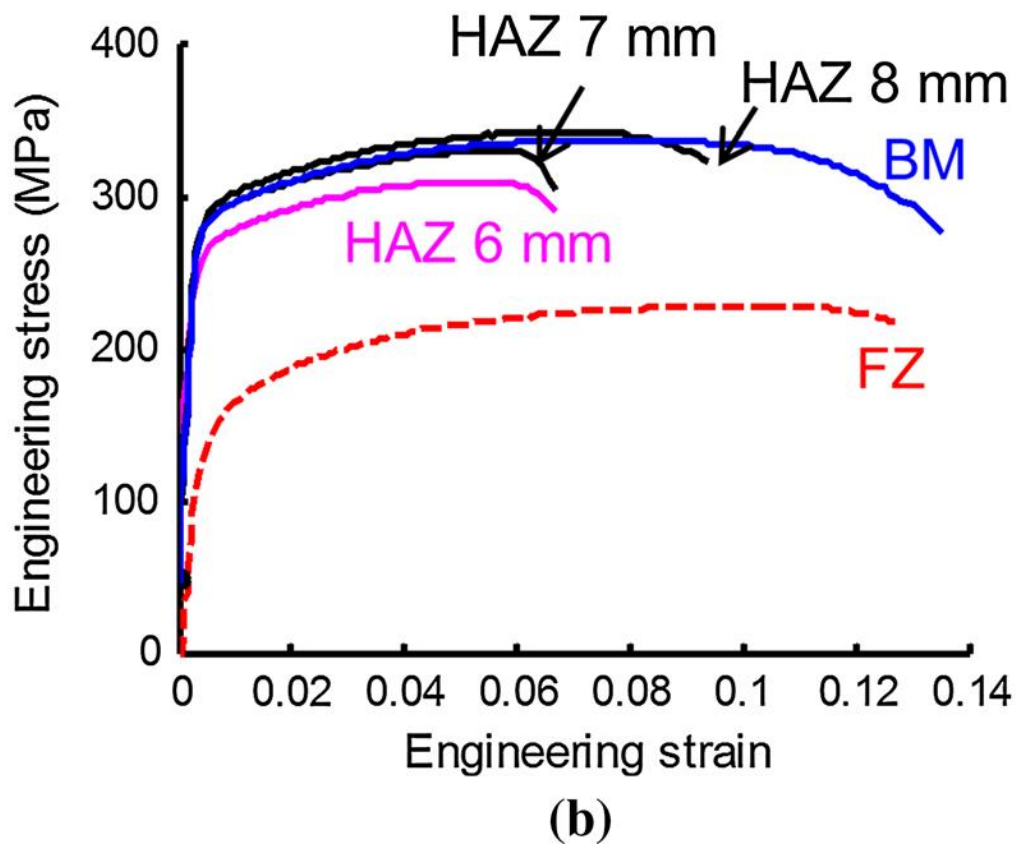
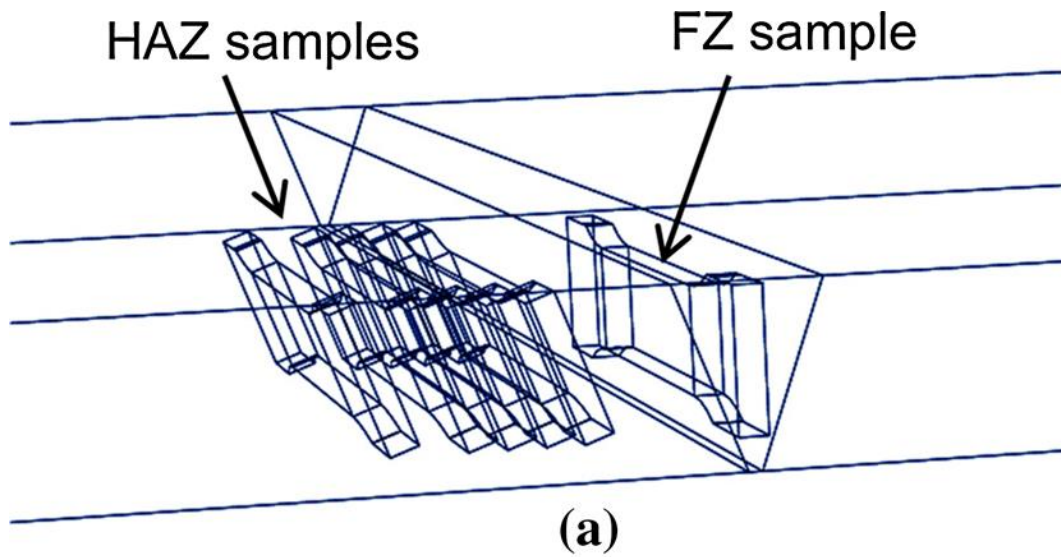


Figure 1-6 (a) Position of the micro-tensile samples with respect to the fusion zone; (b) nominal stress–strain curves for the micro-tensile samples in the different zones of the weld assembly [41].

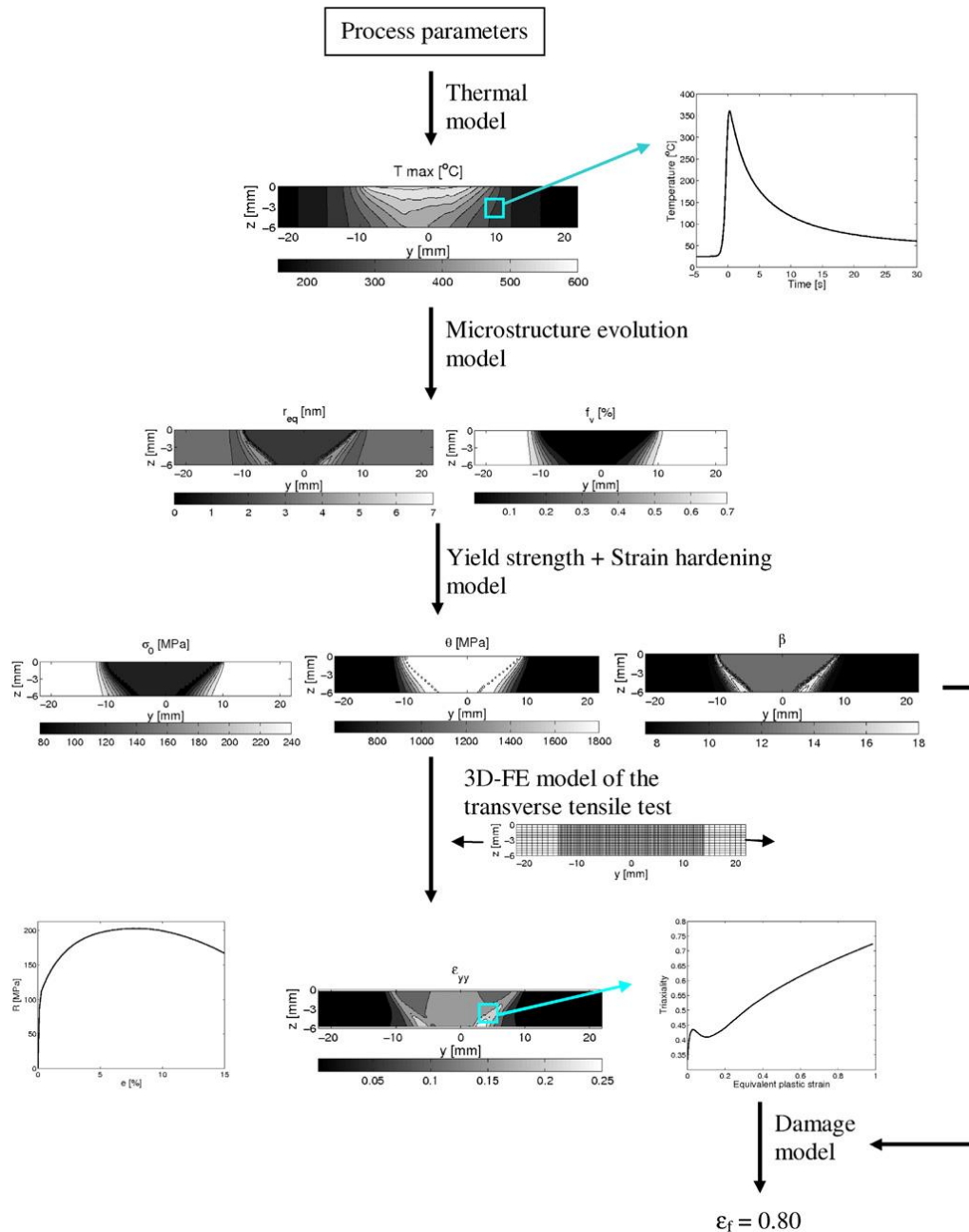


Figure 1-7 Principle of the integrated chain modelling applied to a friction stir weld made of a 6005 Al alloy with the advancing speed of 1000 mm/min and the rotational speed of 1000 rpm. [51]

1.2.3 Crystal plasticity finite element simulation

Prediction of the mechanical properties of metallic components, which is performed by traditional finite element simulation [43, 53-58] with software such as Abaqus and Ansys, is more or less based on macroscale stress-strain data, with limited links between the microstructure and mechanical properties. However, the quantitative relationship between

microstructure and mechanical properties can not only allow precise prediction of the material, but also shed new insights on designing the structural components [59]. As shown in *Figure 1-8*, crystal plasticity finite element (CPFE) simulation can apply knowledge of single grain deformation with the mechanism(s) of dislocation/twinning (or both) to explore the deformation behaviour of polycrystal bulk, paving a new way for the design of engineering applications [60].

The power of CPFE simulation has been demonstrated in describing the anisotropic mechanical behaviour of single-crystalline and polycrystalline samples [60]. For instance, Zhang et al. [61] used CPFE to successfully predict the anisotropic yield behaviour of polycrystalline materials. Pinna et al. [62] employed a CPFE model to accurately predict the crystal texture and grain structure in FCC metal under deformation. Chandra et al. [63] applied CPFE simulation to predict the deformation behaviour of single-crystal and polycrystal Cu samples under tensile test, and the results showed good agreement between experiments and simulation. These cases prove that the CPFE model can give accurate prediction of the plastic deformation of metals.

The accuracy of the CPFE model relies on the mechanical-deformation data of single crystal, which determines the materials parameters used in CPFE simulation. Most of the mechanical experiments for welded joints have been performed using polycrystalline samples, which causes difficulty in determining the mechanical properties of a single crystal (SC), as stress in individual grains can differ [64, 65]. One direct way to determine the mechanical deformation of a SC is to deform the SC using compressive or tensile testing on a large/macro SC [66, 67]. This is mainly applicable for pure metal which can be grown into a macro single crystal. For alloys, the SC may be obtained by the Bridgman technique [64]. Nevertheless, the grain size in the fusion zone is only a few tens of micrometres [22] because of the rapid solidification process. Such small grains make it impossible to obtain mechanical properties of SC utilising

macroscopic testing methods. Thus, a new method that can obtain the mechanical properties of single crystals is needed.

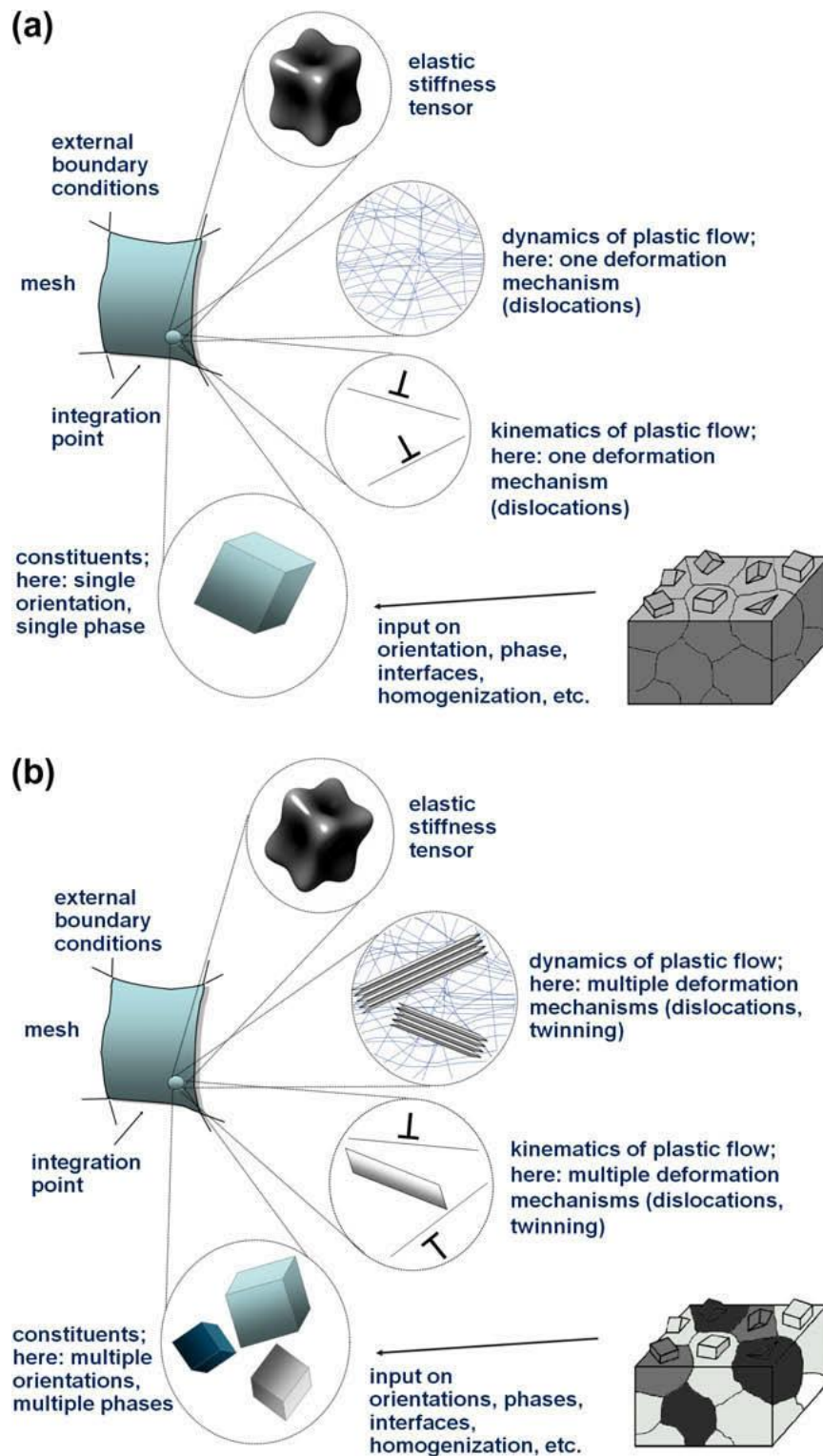


Figure 1-8 Scheme of the conceptual ingredients in CPFE simulation. (a) case of one phase with dislocation as the deformation mechanism, (b) case of several phases, multiple orientations and two deformation mechanisms (dislocation and twinning). [60]

1.2.4 Microscale testing

1.2.4.1 Single metallic crystals

Uniaxial compression technology was introduced in 2004 by Uchic et al. [68] for study of the small-scale mechanical properties of cylindrical Ni and its alloys' micro-pillars attained by focused ion beam (FIB). As shown in *Figure 1-9*, a cylindrical pillar at microscale is made using FIB, then it is compressed using a diamond flat punch in a nanoindenter (*Figure 1-9b*). The stress-strain curves obtained are different from those obtained at macroscale. As seen in *Figure 1-9c*, the stair-like strain burst can be seen in the plastic strain period, and the yield stress is much higher than that of the bulk. The deformed morphology of the pillar features slip offsets (*Figure 1-9d*).

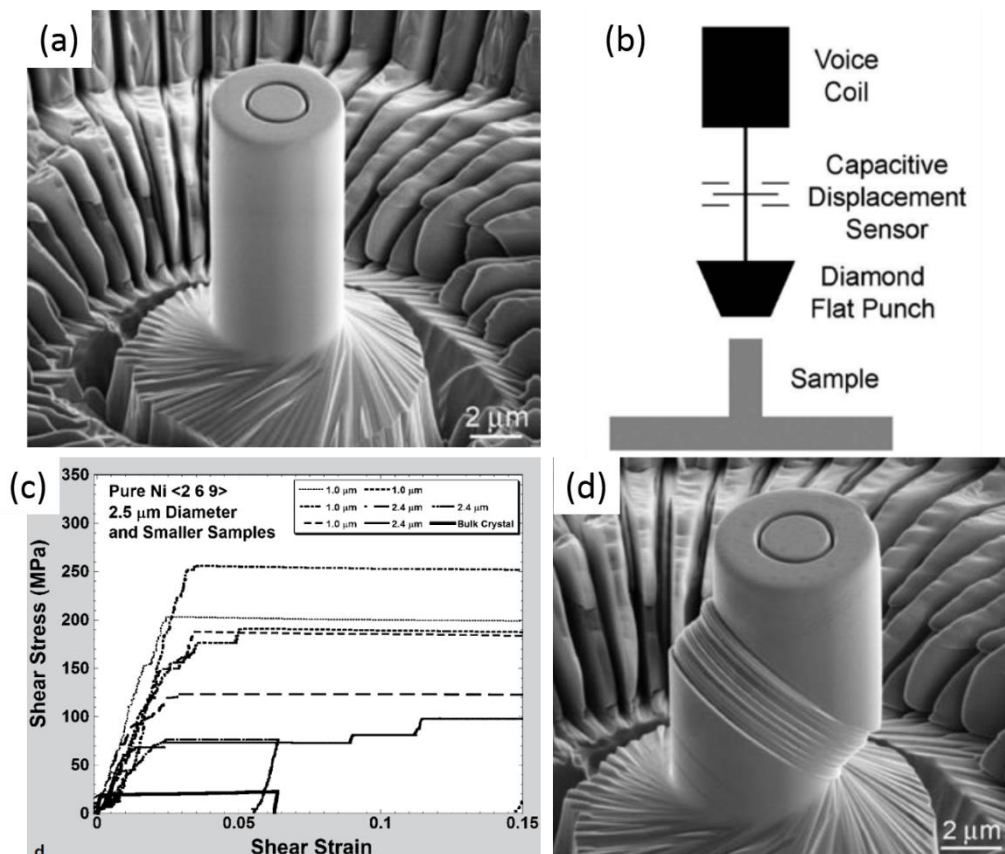


Figure 1-9 (a) Cylindrical pillar machined by FIB, (b) scheme of compression test with a flat diamond punch, (c) stress-strain curves, (d) deformed morphology of the pillar [69].

Subsequently, Greer and colleagues used the same method but at smaller scale (nanoscale) to study the mechanical properties of SC Au, which showed unprecedented strength nearly 50 times greater than that of its bulk form [70]. Using this methodology, much attention has been paid to other pure FCC metals, such as Cu, Al. Most experiments have clearly demonstrated that the flow strength of SC at nano/microscales strongly depends on the sample size, as shown in *Figure 1-10*. The relationship between flow stress and the sample diameter can be described by the power law [71]:

$$\frac{\tau}{\mu} = A\left(\frac{D}{b}\right)^m \quad \text{Eq. 1-1}$$

where τ is the critical shear stress, μ is the shear modulus, D is the sample's diameter, b is the magnitude of the Burgers vector, m is the size exponent. The average of the size exponent for the FCC metal is -0.66 according to this equation.

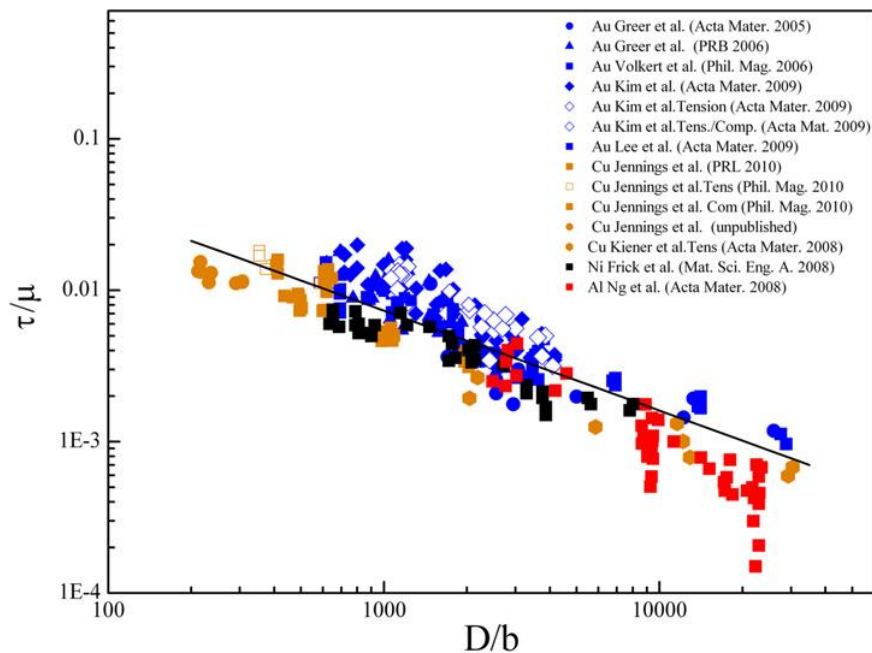


Figure 1-10 Shear flow stress normalized by shear modulus on appropriate slip system for most face-centred cubic (fcc) metallic micro- and nano-pillars tested in compression and tension to date [72].

1.2.4.2 Alloying metallic system

Although higher strength can be obtained at nano/micro scales, the main drawback is the strain burst that lowers the liability at such scales. Through in-situ experiments, it has been found that such strain bursts are due to the slip offset and dislocation movement. To maintain/obtain smooth stress-strain curves, some researchers have tried to locate a barrier to dislocation movement, such as precipitates and solute atoms, in the pillar via alloying.

Girault et al. [73] used the same testing technique to study the mechanical behaviour of Ni-based MA6000 alloys containing 20-30nm-sized oxide dispersoids and 275-300 nm-sized precipitates. Their results showed that the exponent for size effect was about -0.04 ± 0.02 , much lower than that of the Ni pillar. They attributed this finding to the fact that finer particles in the alloys could effectively impede the dislocation movement and concluded that the deformation behaviour of such alloys was predominantly determined by the internal obstacle spacing rather than the diameter of the external sample. The absence of a size effect on the strength at nano/micro scales was also reported in a dual-phase steel by Ghassemi-Armaki et al. [74]. However, there are other researchers who have argued the size effect on strength is still applicable for an alloying system. Gu et al. [42] studied the microscale deformation behaviour of AA2025 with two different age statuses, naturally aged and peak-aged. Their results revealed a much weaker size-dependent strength compared to pure Al, because of the internal precipitates. Raghavan et al. [75] reported size-dependent strength in a solid-solution strengthened high entropy alloy FeCrCoMnNi, and they found a lower sized exponent (-0.32). These studies imply that the strength at small scales is determined not only by the sample size but also by the internal microstructure.

1.2.4.3 Governing mechanisms

Since dislocation is the only carrier of plasticity in the nano/micro regime, several dislocation-based mechanisms have been formulated to explain the observed size effect. The

most favoured explanations are the dislocation starvation model proposed by Greer and Nix [76] and the single-ended dislocation source model proposed by Parthasarathy et al. [77].

The dislocation starvation model is acceptable at nanoscale. In a nanometre-sized pillar, the dislocation travels over only a very short distance before escaping from the free surface, thus reducing the possibility of dislocation multiplication. In other words, dislocations show a preference to annihilate from the sample rather than interacting with each other, which results in a dislocation-starvation state. To maintain the plastic flow, higher stress is required to nucleate new mobile dislocations. Direct evidence supporting dislocation starvation was first reported in an in-situ TEM nano-compression experiment of submicron nickel pillars [78], as shown in *Figure 1-11*. The experiment demonstrated that a pillar containing high density dislocation could be made dislocation free by compressing the pillar. This phenomenon, termed “mechanical annealing”, supports the unambiguous evidence of source-limited deformation, where hardening occurs through the progressive exhaustion of dislocation sources, causing dislocation starvation. Based on this idea, Wang et al. [79] also observed dislocation-starvation states in a 500nm-thick Al single crystal by cyclic loading, as shown in *Figure 1-12a*, and applied cyclic loading to remove the dislocation defect and strengthen the crystal with small volumes (*Figure 1-12b*).

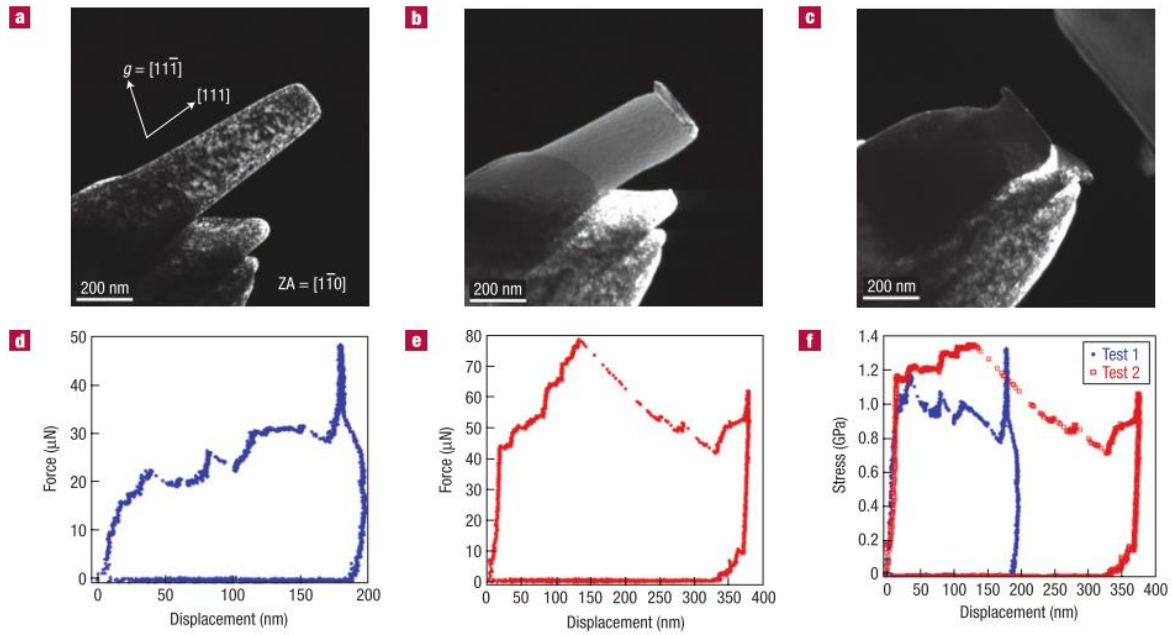


Figure 1-11 In-situ TEM compression test on a $\langle 111 \rangle$ -oriented 160 nm-top-diameter Ni pillar, (a) high-dislocation-density pillar before compression, (b) dislocation-free pillar after the first compression, (c) after the second compression, (d) displacement-force curves for the first compression, (e) displacement-force curves for the second compression, (f) displacement-stress curves for two compression tests [78].

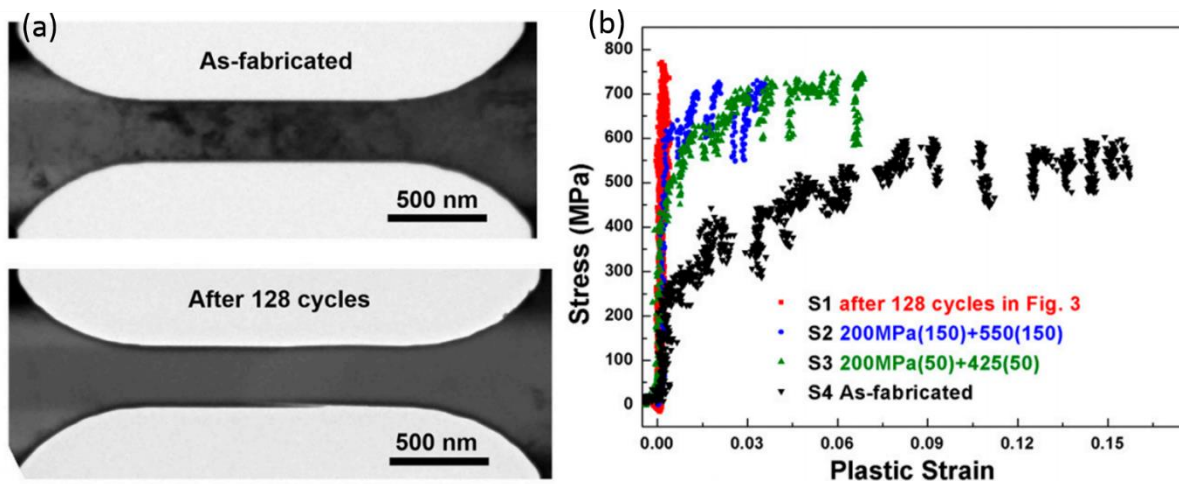


Figure 1-12 (a) Dislocation-starvation state in Al crystal after 128 cycles, (b) plastic strain-stress for the Al crystals in as-fabricated state and dislocation-free state [79].

At micron scale, the theory of the single-ended dislocation source is used to explain the observed size-dependent strength. In the microscale sample, as shown in *Figure 1-13a*, the double-ended dislocation sources would turn into single-ended sources because of the image force of the free surface. It is proposed that for such cases, the strength of the sample is

determined by the longest dislocation source, as shown in *Figure 1-13b*. And the critical resolved shear stress (CRSS) is calculated as [77]:

$$CRSS = \frac{\alpha Gb}{\bar{\lambda}_{max}} + \tau_0 + 0.5Gb\sqrt{\rho_{total}}$$

where α is a constant, G is the shear modulus, b is the magnitude of the Burgers vector, τ_0 is the friction shear stress, ρ_{total} is the total dislocation density, and $\bar{\lambda}_{max}$ is the effective maximum length of the dislocation source. This theory has been successfully applied to explain the size-dependent strength in micro-sized samples, such as FCC and body centred cubic (BCC) single crystals [80] and high entropy alloys [81].

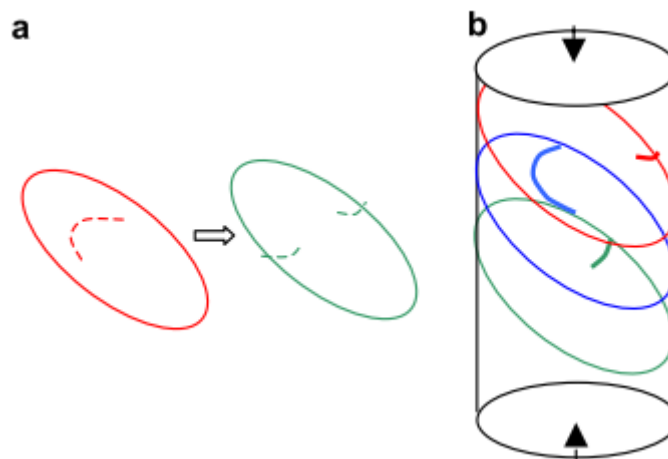


Figure 1-13 (a) Scheme of double-ended dislocation source turning into single-ended dislocation source, (b) distribution of single-ended dislocation sources in a finite sample [77].

1.3 Motivation of this research

The foregoing literature review reveals that impressive progress has been made in the hybrid laser welding of Al alloys, but several open questions remain for hybrid laser welding of Al-Mg-Si alloys, ranging from manufacturing to the prediction of properties:

- (a) Defects, such as porosity and cracks cannot be eliminated, but can be minimized to some extent by adjusting the welding process parameters. The manufacturing process

is not a problem for welding of Al-Mg-Si alloys with either filling wire (Al-Mg and Al-Si alloys). The question is: What kind of wire should be used when hybrid laser welding is used to join Al-Mg-Si alloys? What criteria should be taken into consideration when selecting the filling materials? More importantly, how would the long-term properties (such as fatigue and corrosion resistance) of the welded joint perform?

- (b) Can the plasticity in the fusion zone accurately predict the onset of plasticity in the hybrid laser-welded AA6061-T6 joint although the fusion zone withstands almost all of the strains under external loading (see Ref. [41])?
- (c) The micropillar compression test provides a way of measuring the mechanical properties of a single crystal even when the grain size is small. But the strength at nano/microscales can be influenced by the size and internal microstructure of the sample. Fusion zone is a part of aluminium alloys subjected to strong thermal cycles and rapid solidification processes. The question is: Is the size-dependent strength still effective for the single crystal in the fusion zone? If so, is there a critical size from which the size effect disappears? How does the welding process (e.g., the choice of the filling materials) affect the size effect?
- (d) If the plasticity of single crystal is not determined by its size, how could this data could be used to predict the onset of plasticity of the hybrid laser-welded joint via CPFPE simulation?

1.4 Outline of this thesis

In this thesis, the properties of hybrid laser-welded AA6061-T6 joints are studied from nanoscale to macroscale via nanoindentation and macroscale testing methods. Chapter 1

reviews current studies of the hybrid laser welding of Al alloys, from the manufacturing process to the mechanical properties obtained by experiments and simulation at various scales.

In Chapter 2, different filling materials, ER5356 (Al-Mg alloys) and ER4043 (Al-Si alloys), are used for joining AA6061-T6 by the hybrid laser-MIG welding method. The microstructure, mechanical properties, and service-related properties are studied to provide a guideline for the selection of appropriate filling materials when hybrid laser welding such alloys. Furthermore, a strength model is constructed and used to predict the yield strength of the hybrid laser-welded AA6061-T6 joint.

In Chapter 3, the nano/microscale crystal plasticity of the fusion zone in the hybrid laser-welded AA6061-T6 with ER5356 as filling material is studied via compressing cylindrical pillars in a nanoindenter. The effect of crystal orientation and pillar's diameter on the mechanical deformation behaviour of the fusion zone at nano/microscale is investigated.

In Chapter 4, comparisons of the nano/microscale crystal plasticity in the fusion zone with different microstructures are made via the compression on a pillar in a nanoindenter. The yield strength at the nano/microscale is controlled not only by the pillar's size but also by the inner microstructure. A theoretical model is built and used to quantifying the effect of alloying, orientation, size and dislocation density on the nano/microplasticity of fusion zone.

In Chapter 5, CPFEM simulation is used to predict the mechanical behaviour of SC in fusion zones. Based on the microplasticity, the behaviour of bulk under compressive and tensile testing is predicted by finite element simulation the crystal plasticity. This chapter, shows, for the first time, the nano/microscale plasticity of the fusion zone and its link to the mechanical properties at macroscale.

In Chapter 6, the summary of this thesis is presented based on the results in Chapters 2-5. Opportunities for future multiscale study of hybrid laser-welded Al alloy joints are suggested.

Chapter 2 Effect of filling materials on the microstructure and mechanical properties of hybrid laser-welded Al-Mg-Si alloy joints

2.1 Introduction

In this chapter, a series of investigations is conducted to examine the influence of filling materials on the microstructure and properties of hybrid laser-welded AA6061-T6 joints, which are first characterized. Then a strength model is constructed and used to explore the strengthening mechanism. A summary is made of the performance of both welded joints to shed light on the selection of appropriate filling materials when welding AA6061-T6 alloys by the hybrid laser welding method.

2.2 Experimental methods

2.2.1 Hybrid laser welding

The base metal (BM) used in this study was aluminium alloy (AA) 6061-T6, which is commonly used in structures of automobiles, high-speed trains, and aerospace craft, with the dimensions of 250 mm×250 mm×4 mm. The filling materials were ER5356 and ER4043 with the diameter of 1.6 mm. ER5356 was Al-Mg alloys and ER4043 was Al-Si alloys. The chemical compositions of the BM and filling materials are listed in *Table 2-1*.

Table 2-1 Chemical compositions of the base metal and filling materials (wt.%).

	Mg	Si	Cr	Mn	Fe	Cu	Zn	Ti	Al
AA6061-T6	0.8-1.2	0.4-0.8	0.04-0.35	0.15	0.7	0.15-0.4	0.25	0.15	Balanced
ER4043	0.05	4.5-6.0	-	0.05	0.8	0.3	0.1	0.2	Balanced
ER5356	4.8	0.1	0.1	0.15	0.4	0.1	0.1	0.13	Balanced

The AA6061-T6 plates were joined by a hybrid fibre laser welding system, as shown in *Figure 2-1*. Some details of the system are given in *Table 2-2*.

Table 2-2 Details of the hybrid laser welding system used in this study.

Welding parameters	Value range
Laser Power (P_L) /kW	0-4
Wavelength of the laser/ μm	1.07
Core diameter of the fibre/ μm	200
Defocusing distance (L_{d0}) /mm	0
Distance between laser beam and filler wire (D_{LA}) /mm	2
The angle of the laser beam to the welding direction / $^\circ$	75
The angle of the MIG torch to the welding direction / $^\circ$	56
Weld stick-out length /mm	12
Shielding gas flow rate / $\text{L}\cdot\text{min}^{-1}$	25
Shielding gas	Argon (99.999%)

To obtain a desired welded joint, several welding parameters (laser power, arc current, arc voltage, and welding speed) were applied in order to avoid welding defects or loss of alloying elements due to excessive heat input. The optimized parameters for the welding process used with two different filling materials are listed in *Table 2-3*. After welding, the welded plates were examined using an X-ray inspection system to see if any defects (e.g., porosity, cracks) were included in the weldments. As shown in *Figure 2-2*, no macro-pores or cracks existed in the joints, and the weld appearance of both was of high quality without undercut.

Table 2-3 Parameters for hybrid laser welding AA6061-T6 with different filling materials

Filling material	Arc current (A)	Arc voltage (V)	Laser power (kW)	Welding speed (m/min)
ER5356	148	24.4	2.3	1.2
ER4043	173	21.1	2.2	1.2

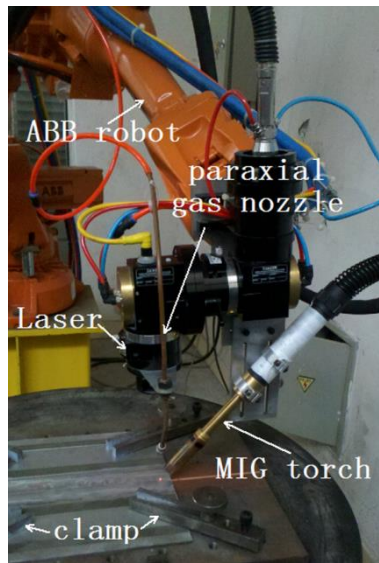


Figure 2-1 Hybrid laser welding system used in this study [16].

	ER5356 joint	ER4043 joint
Appearance		
X-ray detection		

Figure 2-2 The weld appearance and X-ray detected images of the ER4043 and ER5356 joint under optimized welding parameters.

2.2.2 Sample preparation

Samples of the welded joints were left for more than one month to minimize the effect of natural ageing on the mechanical properties, after which rectangular blocks about 1 mm³ in size were cut from the centre of FZ using a diamond saw at slow speed and with water as cooling lubricant. The samples were then mounted using resin. The mounted sample was ground and polished using the steps listed in *Table 2-4*. In the last step of the polishing process, 0.02 µm colloidal silica solution was applied to remove the deformed layer on the

surface of the sample. The well-polished sample was used for the electron backscatter diffraction (EBSD) testing and the subsequent tests. Transmission electron microscope (TEM) sample of the bulk FZ was prepared by an ion polishing method in a precision ion polishing system (PIPS).

Table 2-4 Procedures for grinding and polishing samples.

	Step	Grinding paper/polishing cloth	Polishing solution	Sample speed (RPM)	Plate speed (RPM)	Force (lbf/N)	Time (min)
Grinding	1	400 Grit SiC paper	water	300	300	22	5
	2	800 Grit SiC paper	water	300	300	22	5
	3	1200 Grit SiC paper	water	300	300	22	5
	4	2000 Grit SiC paper	water	300	300	22	5
Polishing	1	polishing cloth	6 μm polycrystalline diamond paste and glycol suspension	300	300	22	10
	2	polishing cloth	3 μm polycrystalline diamond paste and glycol suspension	300	300	22	10
	3	polishing cloth	0.02 μm colloidal silica solution	150	150	13	60

Note: All consumables were purchased from Allied High-Tech Products, Inc.

2.3.3 Microstructure characterization

The etching experiment was done using Keller's solution, which was composed of 2.5% HNO₃, 1.5% HCl, 1% HF, and 95% DI water. A light microscope was used to examine the microstructure in the welded joint. The microstructure of the samples was also examined under a Zeiss Ultraplus Field Emission Scanning Electron Microscope (FESEM). The chemical compositions of the matrix and the precipitates were measured using energy dispersive spectroscopy (EDS). The EBSD test was performed to obtain the grain size and orientation distribution in the fusion zone. The EBSD test was carried out under 20 KV acceleration voltages, 4 nA beam current, and 24.5 mm working distance. The step size of the test was 3 μm to obtain data accuracy and efficiency. The EBSD data was processed using commercial HKL software.

2.2.4 Property characterization at macroscale

After welding, the material in the HAZ was able to recover some strength due to natural ageing, but this effect was significant in the first month only (more accurately, the first 14 days) and decreased considerably during the subsequent ageing time (see Refs. [82, 83]). Thus, the welded joint was intended to be naturally aged for one month before any mechanical test was performed to minimize the ageing effect on the strength of the welded joint. All samples for the mechanical testing were taken from the welded joint in the direction perpendicular to the welding direction. Standard dog-bone samples for tensile tests were made using an electron discharge machining (EDM) method, the dimensions for the samples were similar to that in Ref. [6]. The tensile test was conducted at room temperature at displacement rate of 0.5 mm/min, and at least three samples were prepared for each joint type. The gage length for the tensile test was 100 mm. The tensile strength and yield strength were defined as the averaged results of the three tests for each joint. Fatigue samples were machined using the EDM method perpendicular to the welding direction. The surface of the

sample was carefully ground. The fatigue test was performed using a high-frequency machine at the stress ratio of $R=0.1$. The fracture surface of the fatigue sample was observed by SEM to identify fatigue crack initiation and the propagation mechanism.

To obtain information about the in-service life of the welded joint under a corrosive environment, the corrosion resistance of the welded joint was characterized by the potentiodynamic polarization test and the slow strain rate test (SSRT). The cross-section sample for the polarization test was first mounted using resin with the exposed area of 1 cm^2 . The sample was metallurgically polished and ultrasonically cleaned before the test. Then the sample was tested in 3.5 wt% NaCl solution at room temperature, with the applied potential ranging from -0.3 V to 0.6 V at the scanning rate of 0.5 mV/s . The slow strain rate test followed the standard of GBT 15970.7-2000 [84], the setup of SSRT is shown in *Figure 2-3*. Dimensions for the test sample are shown in *Figure 2-4*. The experiment was performed at the strain rate of $5 \times 10^{-6} \text{ s}^{-1}$ with some samples immersed in 3.5 wt% NaCl solution or in air.

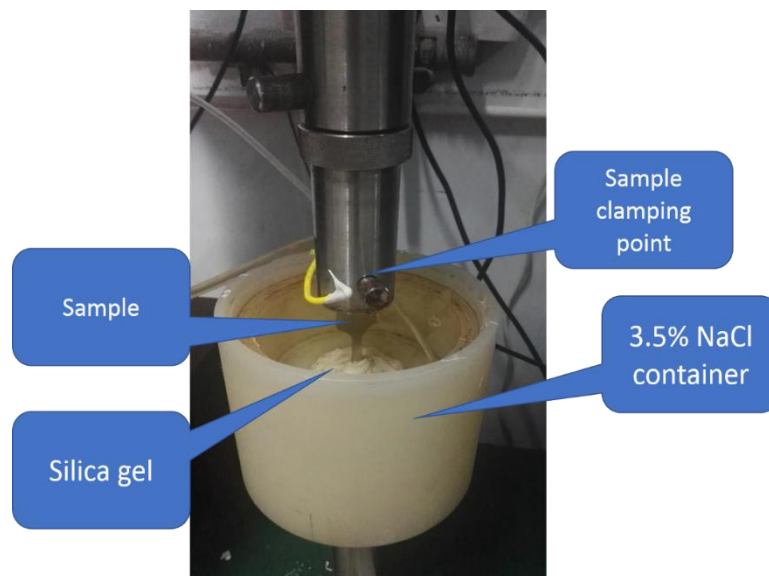


Figure 2-3 Schematic for the setup of the SSRT.

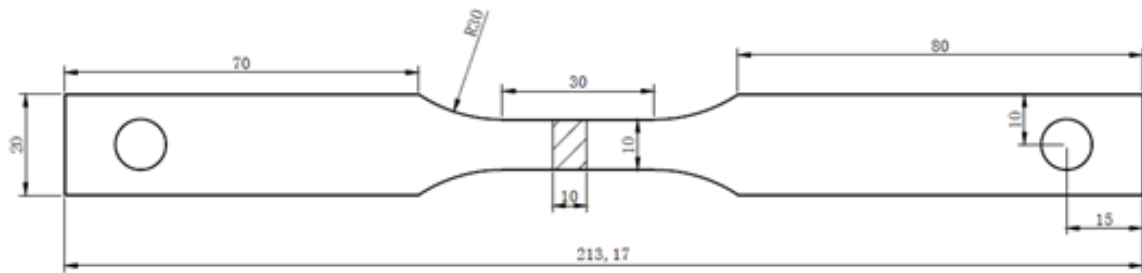


Figure 2-4 Dimensions of the test sample used in the slow strain rate test, the thickness of the sample was 3.8 mm.

2.3. Results

2.3.1 Microstructure of the joint

In *Figure 2-5a*, the centre of the FZ in the ER5356 joint exhibits a dendritic microstructure. Near the fusion line (*Figure 2-5b*), columnar grains are distributed perpendicular to the fusion line and towards the inner part of the FZ. Equiaxed grains can be found in HAZ close to the fusion line, as shown in *Figure 2-5d*. The absence of the equiaxed grains is due to the fact that the material close to the fusion line provides many sources for the crystal nucleation of the liquid metal during welding [85]. Fine grains with small precipitates occupy in the HAZ, as illustrated in *Figure 2-5c*. The BM seems to be filled with enlarged grains, as seen in *Figure 2-5e*. But the EBSD results show that the grain size in the BM is very small, as will be shown in *Figure 2-8c* later. Thus, the “dark lines” are not grain boundaries but are likely to be phases in the BM.

As in the ER5356 joint, the FZ in the ER4043 joint shows dendritic microstructure (see *Figure 2-6a and b*). However, pores can also be observed in the FZ, as marked with white circles in *Figure 2-6a*. The equiaxed-grain area is also found in the interface between the FZ and the HAZ, as shown in *Figure 2-6c*.

SEM and EDS were used to characterize the phases in FZ. From the SEM images (*Figure 2-7a and d*), the dendritic microstructure seen in the optical images (*Figure 2-5a and Figure 2-6b*) is the phase formed during the solidification of the welding process. As demonstrated in *Figure 2-7*, the phases in both joints are large, but have different shapes. The phases in the ER5356 joint (*Figure 2-7b*) are rod like, while those in the ER4043 joint (*Figure 2-7e*) are needle like. The difference between the phase shapes in the two types of joints is possibly attributable to the chemical composition and the solidification process. The EDS results show that the phase in the ER5356 joint is composed of Al, Mg, Si, Cu and Mn, while the phase in the ER4043 joint is made from Al, Mg, Si, Cu, Cr and Fe. Mg_2Si is reported to be the main precipitate in the Al-Mg-Si alloys [6], in accordance with the precipitates sequence [36]: solid solution (SS) \rightarrow spherical-shaped GP zones \rightarrow needle-shaped β'' \rightarrow rod-shaped β' and lath-shaped Q' \rightarrow β (Mg_2Si) and Si. However, if the Cu concentration is 0.9% higher, the resulting phases would be Q ($Al_4Mg_8Si_7Cu_2$) and Si. The Fe element tends to present in the form of Al_3Fe [86].

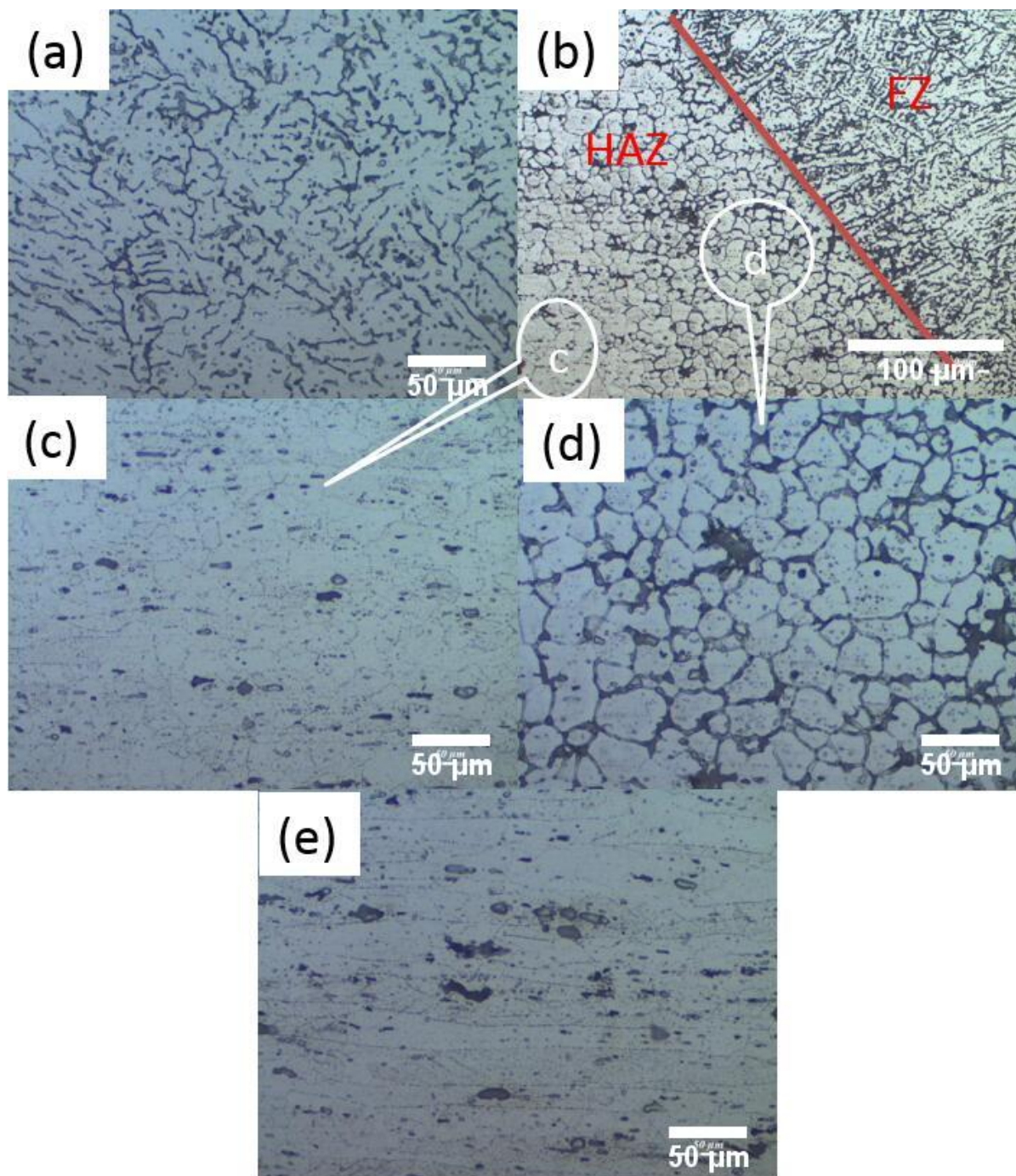


Figure 2-5 Optical images of the hybrid laser-welded joint with ER5356 filling material, (a) centre of fusion zone, (b) overview of the fusion line between the HAZ and FZ, (c) HAZ, (d) equiaxed grains in the HAZ close to the fusion line, (e) base metal.

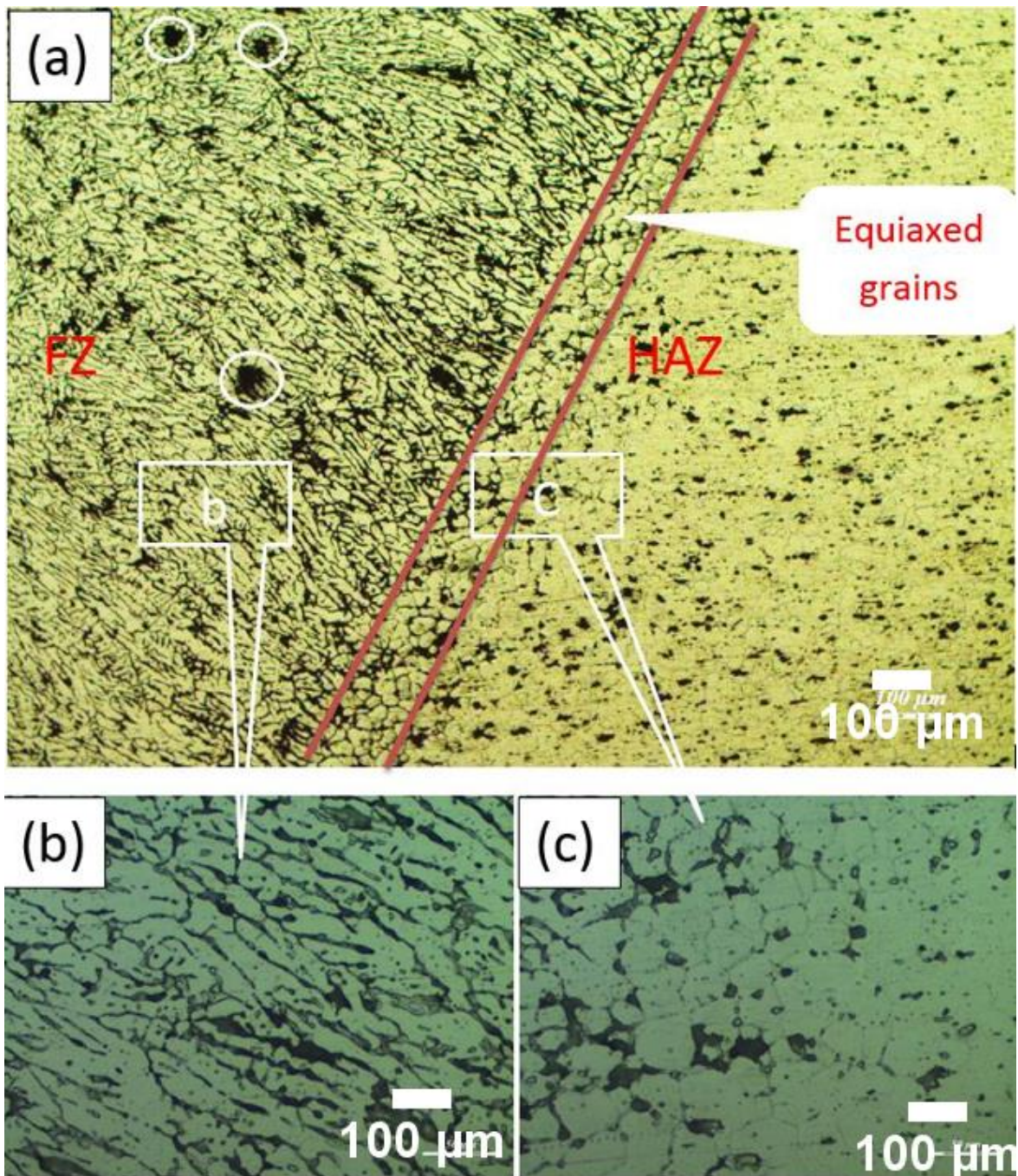


Figure 2-6 Optical images of the hybrid laser-welded joint with ER4043 filling material, (a) overview of the microstructure near the fusion line, (b) the microstructure in the FZ, (c) the microstructure in the HAZ.

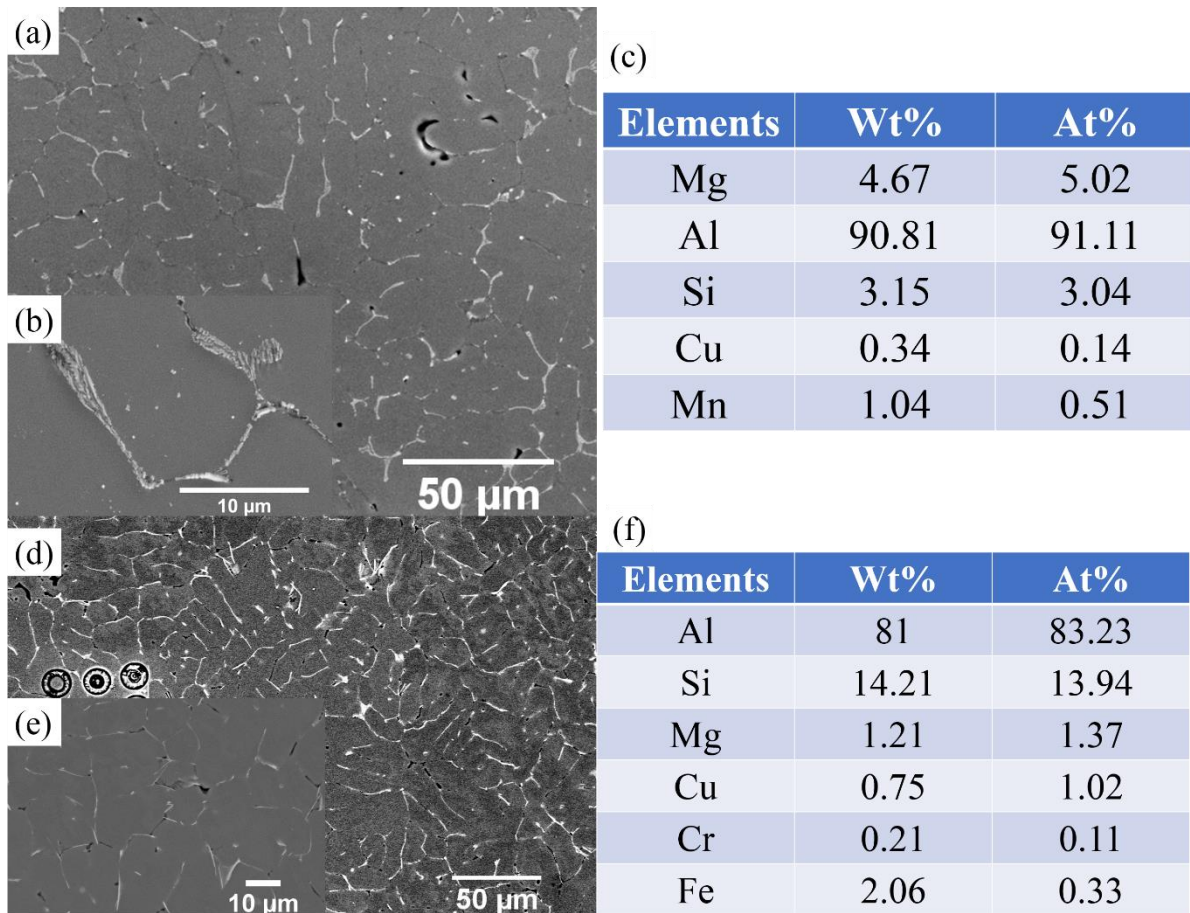


Figure 2-7 SEM images and EDS results of the hybrid laser-welded joint. (a) overview of the FZ in the joint with ER5356 filling material, (b) enlarged view of the precipitates, and (c) the EDS results of the precipitates; (d) overview of the FZ in the joint with ER4043 filling material, (e) enlarged view of the precipitates, and (f) the EDS results of the precipitates.

2.3.2 EBSD results of the joint

The results of the EBSD test are shown in *Figure 2-8*. The grain size in the FZ in both joints (*Figure 2-8a and d*) is larger than in the HAZ and BM. But the grain sizes in two FZs are different, possibly caused by different solidification processes in the welding process. According to the intercept measurement, the averaged grain size of the FZ in the ER5356 and ER4043 joints is $71\pm 53\ \mu\text{m}$ and $57\pm 51\ \mu\text{m}$, respectively. There is no grain size difference in the HAZ of both joints (see *Figure 2-8b and e*), which is $7\pm 4\ \mu\text{m}$. Surprisingly, the grain size in HAZ is the same as that in BM, as demonstrated in *Figure 2-8b and c*, indicating that the

heat input in the welding process does not cause grain coarsening in HAZ. However, the morphology and distribution of the precipitates in the HAZ may be changed in the heat cycles [15]. The pole figures of the two joints are illustrated in *Figure 2-9*. The FZs of both joints (*Figure 2-9a and b*) exhibit no texture, whereas the HAZ and BM have clear textures. The orientation and texture in the HAZ do not change much after the heat cycle.

The dislocation density in the FZ was also characterized through EBSD. The dislocation density (ρ) is related to kernel average misorientation (KAM) by the equation [87-89]:

$$\rho = \frac{\theta_{KAM}}{|b| \times \mu \times n} \quad \text{Eq. 2-1}$$

where ρ is the dislocation density, θ_{KAM} is the kernel average misorientation angle, b is the magnitude of the Burgers vector, μ is the step size of the EBSD test, and n is the number of nearest neighbours. The distribution of KAM for both joints is illustrated in *Figure 2-10*. Taking $b=0.284$ nm, $\mu=3$ μm , $n=2$, the calculated dislocation density of the welded joint is shown in *Table 2-5*. It can be seen from the results that the ER4043 joint has higher dislocation density than that of the ER5356 joint.

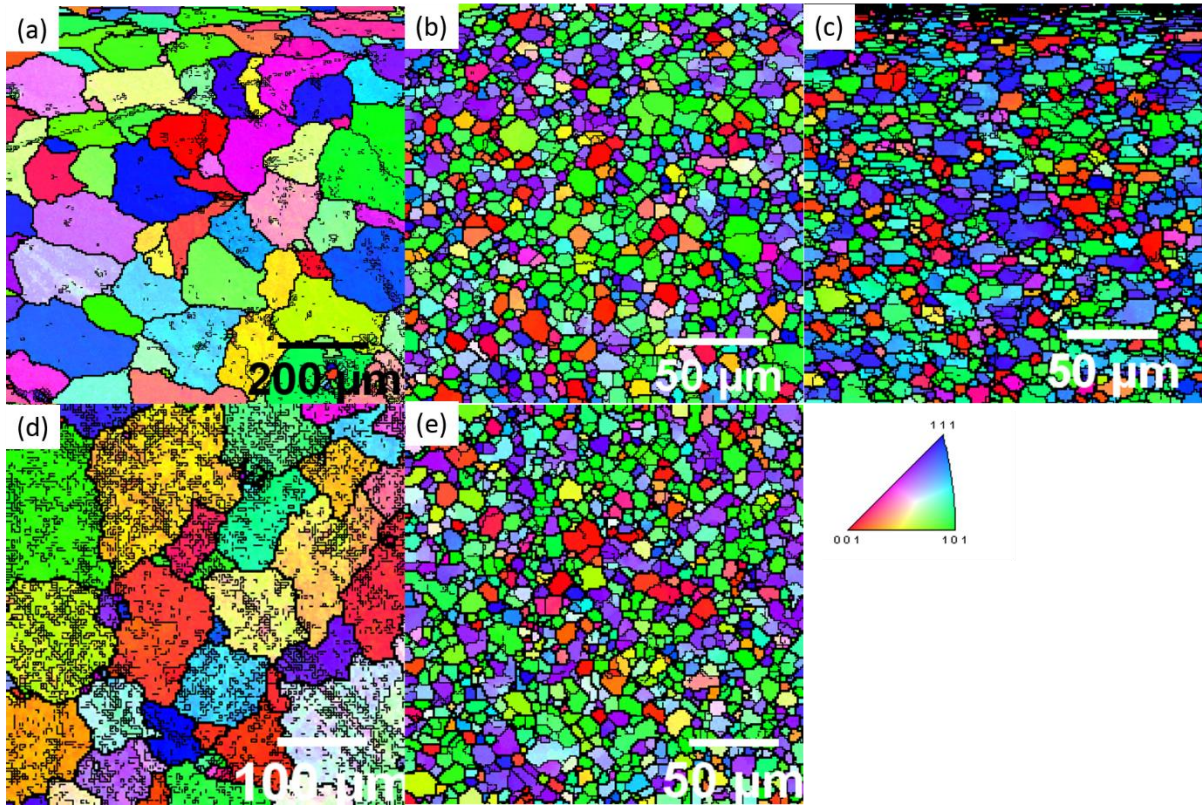


Figure 2-8. IPF images of the hybrid laser-welded joint, (a) FZ of the ER5356 joint, (b) HAZ of the ER5356 joint, (c) BM of the ER5356 joint, (d) FZ of the ER4043 joint, (e) HAZ of the ER4043 joint.

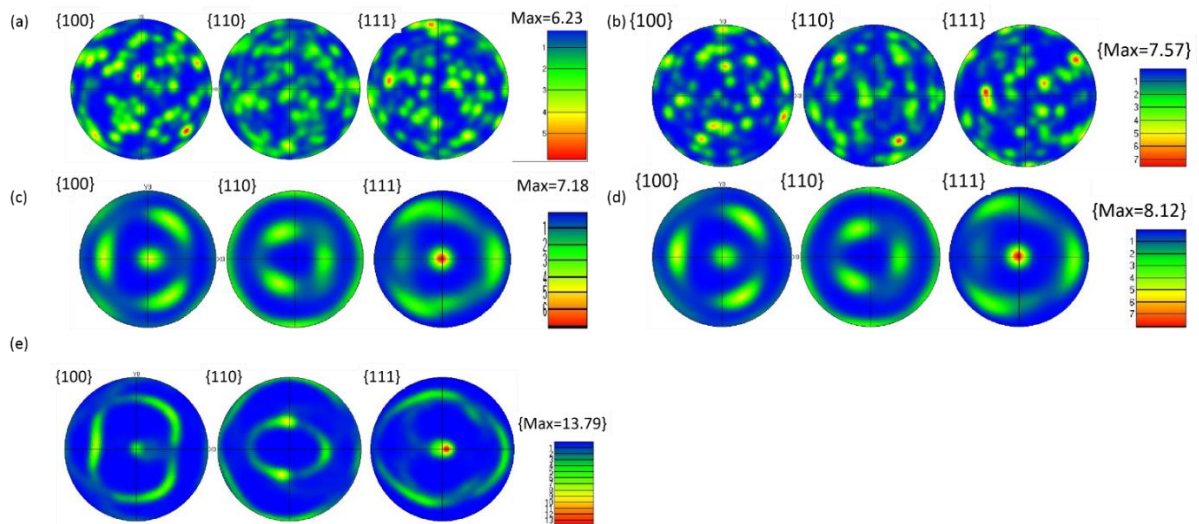


Figure 2-9. (a) (c) (e) Pole figures of FZ, HAZ, and BM of the ER5356 joint, (b) and (d) pole figures of FZ and HAZ of the ER4043 joint.

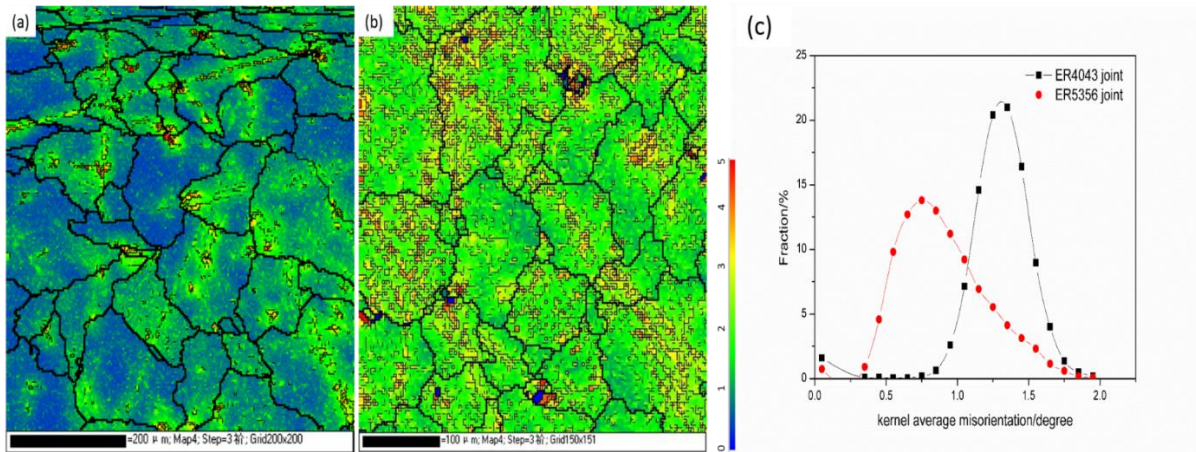


Figure 2-10 KAM maps of (a) FZ of the ER5356 joint, (b) FZ of the ER4043 joint, and (c) distribution of KAM of two different joints.

Table 2-5 KAM and dislocation density for both welds obtained from EBSD testing.

	ER5356 joint	ER4043 joint
KAM (degree)	0.897	1.289
ρ_{GND} (m^{-2})	9.19×10^{12}	1.32×10^{13}

2.3.3 Microhardness and mechanical properties of the joint

Figure 2-11 is the hardness profile of joints with different filling materials. The microhardness test was done on the centre of the cross section of the welded joint. The average hardness of the FZ in the ER4043 joint is higher than that of the ER5356 joint. The cause of the difference is discussed in Section 2.4.1. In the two joints considered, the lowest hardness is in the FZ, while the highest is in the BM. There is a decrease of hardness in the HAZ compared to that in the BM. As mentioned in Section 2.3.2, the grain size and the crystalline texture of BM and HAZ are the same. Thus, the change of precipitates in the HAZ is responsible for the reduction of hardness in the HAZ.

Figure 2-12a shows the tensile stress-strain curves for the BM and two joints. The corresponding tensile strength (at the fracture point or highest strength) and the yield strength

(0.2% offset) are shown in *Figure 2-12b*. The tensile strength of the ER5356 joint and ER4043 joint is 258 MPa and 307 MPa, respectively. The ER4043 joint shows greater strength than the ER5356 joint, which is consistent with the hardness results (*Figure 2-11*). Even though the strength is improved by altering the filling material to ER4043, it reaches only 80% of the BM's strength. However, its joint efficiency is greater than that of the laser-welded AA6061-T6 joint [17]. Although the ER4043 joint has greater tensile strength, its elongation is poorer than that of the ER5356 joint, as demonstrated in the tensile stress-strain curves in *Figure 2-12a*. The representative images showing the fractured portion of the tensile tested samples for the ER5356 and ER4043 joints are shown in *Figure 2-12c-d*. Both joints broken in the FZ, implying that the FZ is the softest area in the joint.

In *Figure 2-13*, macroscopic observation of the tensile fracture shows that both welded joints are broken in the FZ, with the fractured surface having a shear angle of $\sim 45^\circ$. This indicates that both welded joints failed in a ductile way. The SEM images of the fractured surface are presented in *Figure 2-14*. Dimples are distributed over the entire surface of the BM and the two joints. However, the dimples in the ER5356 joint (*Figure 2-14a*) are smaller and deeper than those in the ER4043 joint (*Figure 2-14b*), which explains why the higher ductility of ER5356 joint.

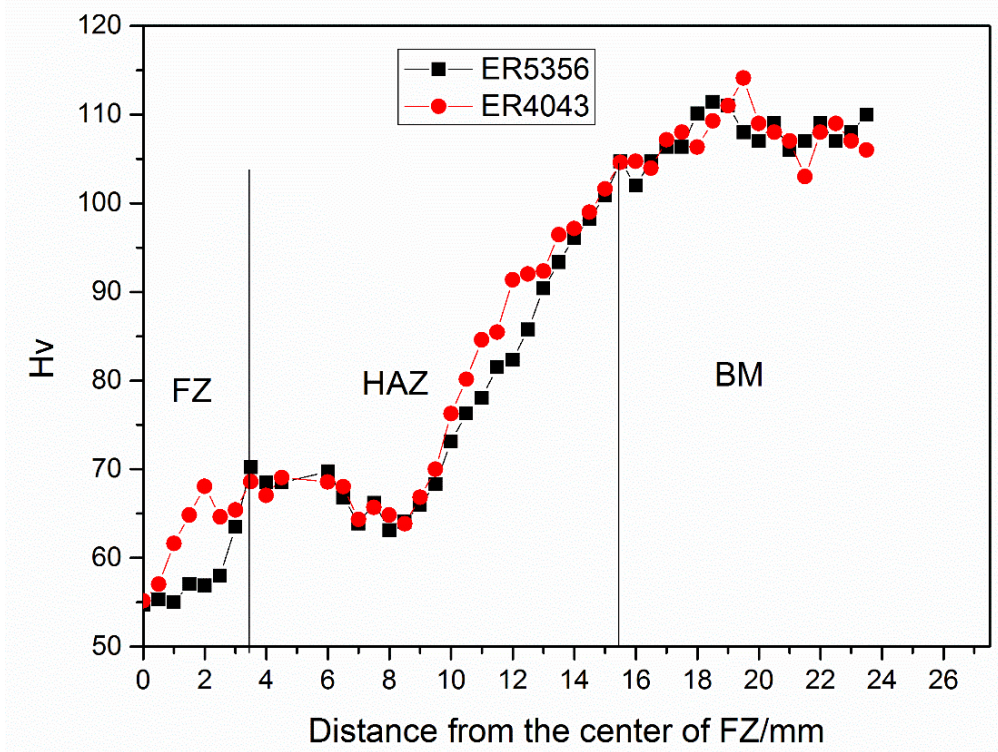


Figure 2-11 Hardness profile of the welded joint with two different filling materials.

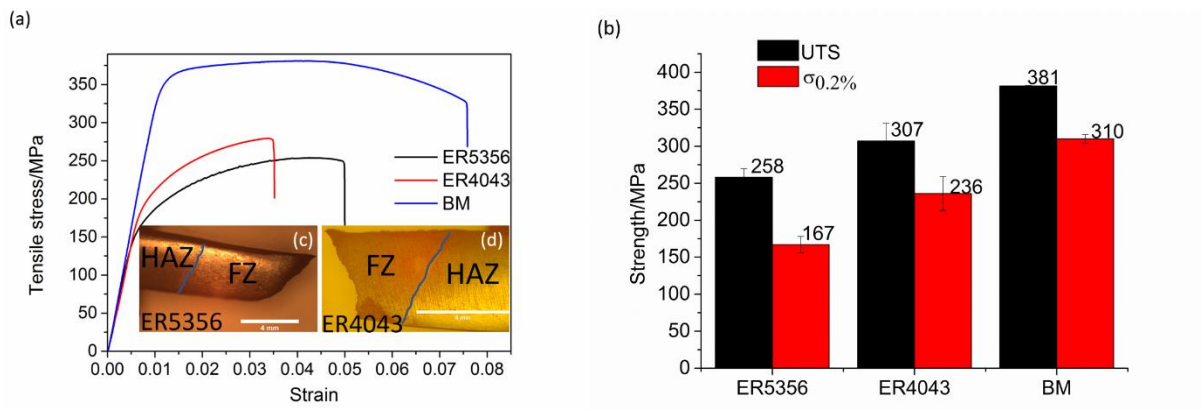


Figure 2-12 (a) Tensile stress-strain curves of ER5356 joint, ER4043 joint and the BM, (b) tensile strength and yield strength of the tested samples, (c)-(d) representative cross-section images of the fractured tensile test sample for ER5356 joint and ER4043 joint.

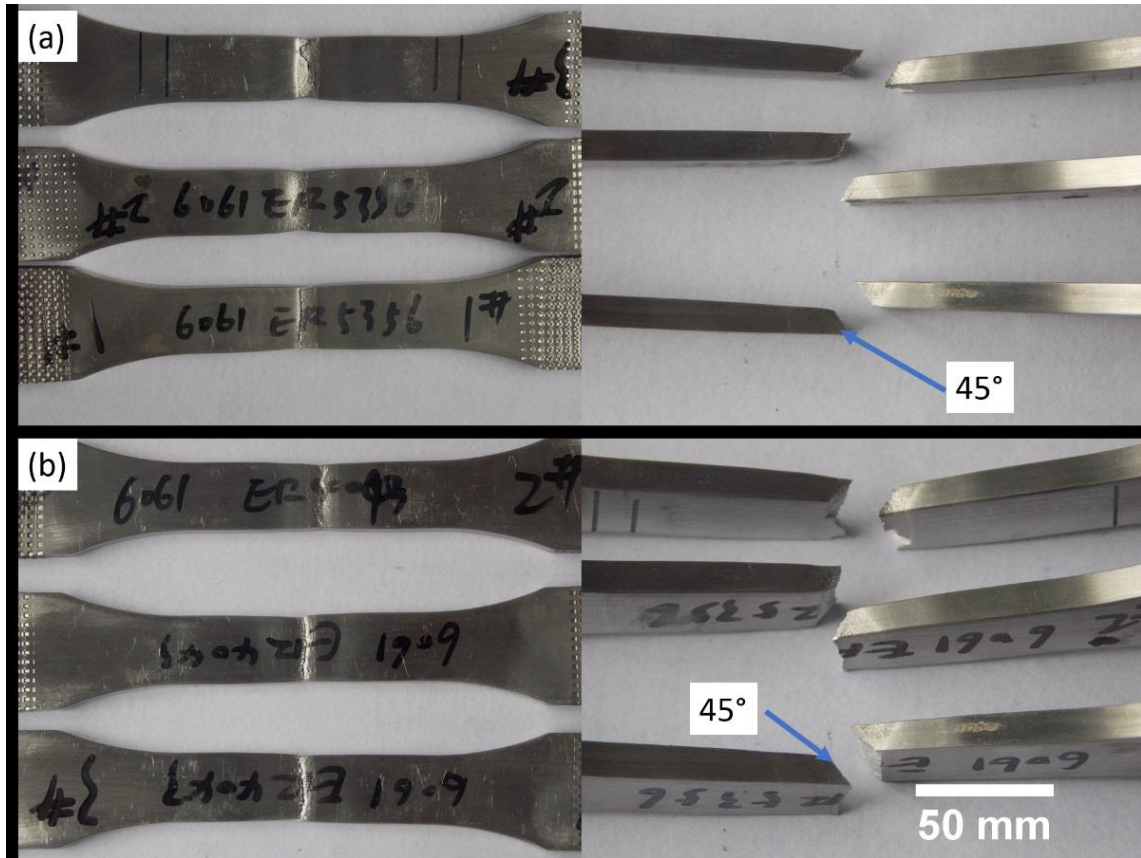


Figure 2-13 Macroscopic view of the fracture of the tested sample after tensile tests, (a) the ER5356 joint, (b) the ER4043 joint.

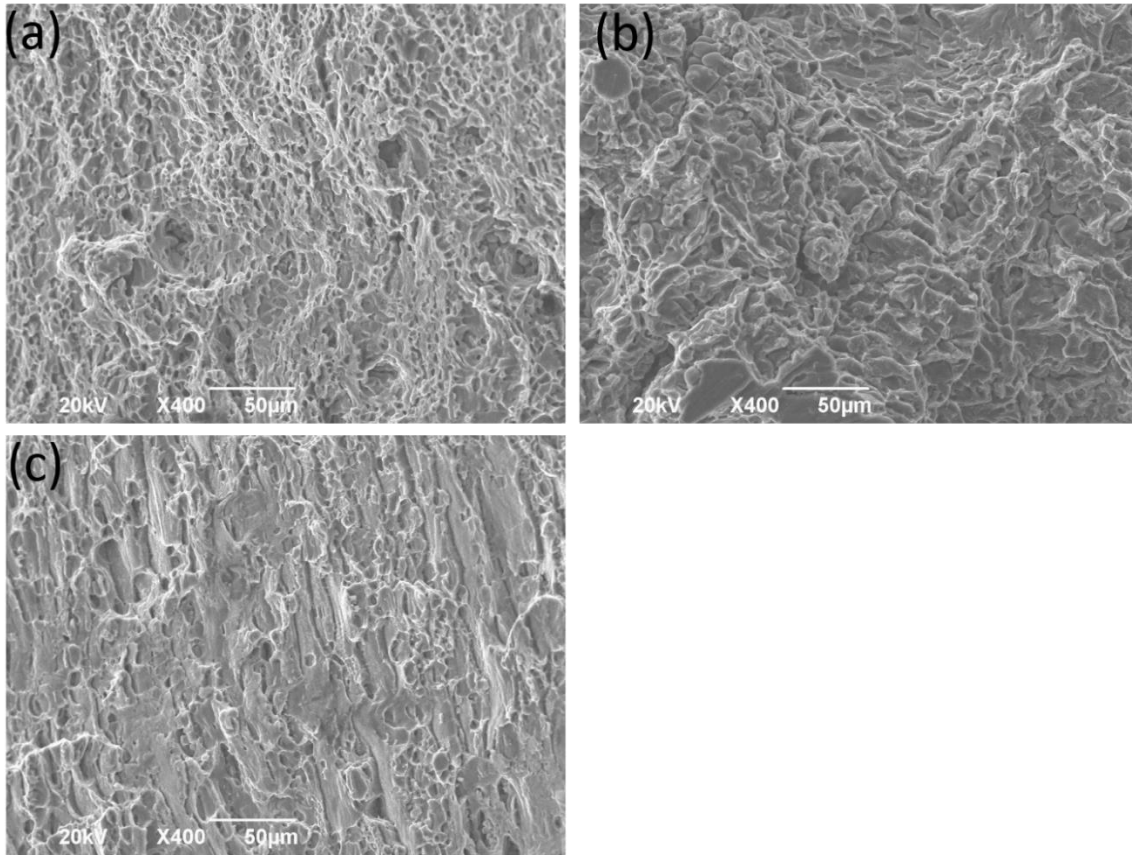


Figure 2-14 SEM observation on the fractured surface of (a) the ER5356 joint, (b) the ER4043 joint, and (c) the BM.

2.3.4 Fatigue properties of the joint

The fatigue properties (S-N curves) of the welded joint are shown in *Figure 2-15*. Since there is no plateau in the S-N curves of aluminium alloys [90], the fatigue life beyond the cycle number of 1×10^7 is called the fatigue strength in this study. As seen in *Figure 2-15*, the fatigue life of both joints increases with decreasing applied stress. The fatigue strength of the ER5356 joint is 105 MPa, which is about 63% of its yield strength. The ER4043 joint shows the fatigue strength of 95 MPa (40% of its yield strength). The fatigue strength of the ER5356 joint and ER4043 joint reached 47% and 43% of that of the BM [91], respectively. As mentioned in Section 2.3.3, the tensile strength of the ER4043 joint is greater than that of the ER5356 joint. But the fatigue strength of the joints shows the opposite pattern. As illustrated in *Figure 2-15b-c*, the fatigue test samples of both joints fracture in the FZ.

SEM images of the fractured surface are shown in *Figure 2-16* and *Figure 2-17*. For the ER5356 joint, the fatigue crack initiates from the pores, as demonstrated in *Figure 2-16a* and *b*. In the propagation period (*Figure 2-16c*), some striations can be seen on the surface. In the fracture period, dimples occupy the entire area, a finding which is similar to that from the tensile test. Similarly, the fatigue fracture of the ER4043 joint starts from sites with multiple pores (*Figure 2-17a-d*). Since elastic behaviour was dominant under high-cycle loadings, cracks initiated from defects. In *Figure 2-17a-d*, pores can be seen in the entire cross-sectional surface of the fractured sample. Compared to the ER5356 joint, the pores in the ER4043 joint are much bigger and more intensive. Sites with pores can act as stress concentration sites during cyclic loading and are the preferable places for crack initiation. This finding may explain why the fatigue life of the ER4043 joint is shorter.

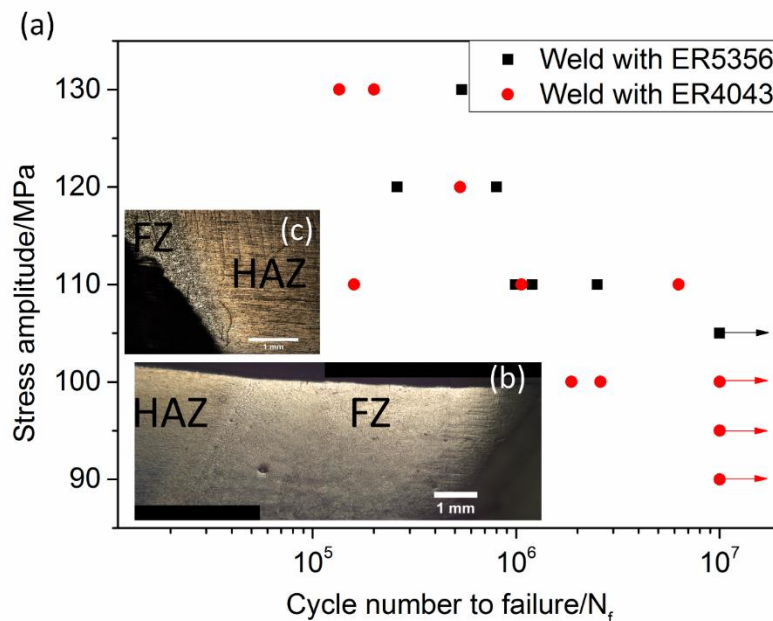


Figure 2-15 (a) S-N curves of the ER5356 joint and the ER4043 joint, (b) representative cross-section image of the fractured fatigue test sample for the ER5356 joint, (c) representative cross-section image of the fractured fatigue test sample for the ER4043 joint.

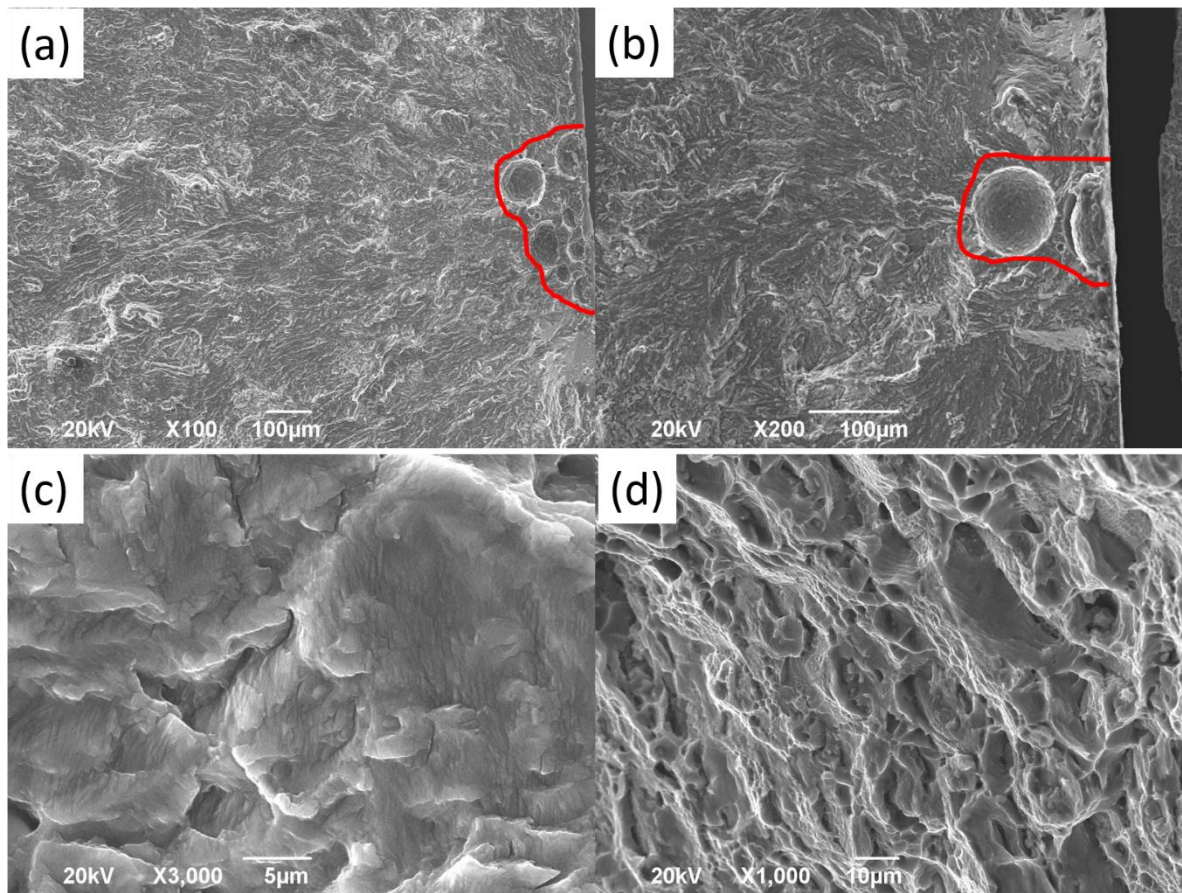


Figure 2-16 Fatigue fracture of ER5356 joint, (a)~(b) crack initiation from pores, (c) striation during the propagation period, (d) fracture period.

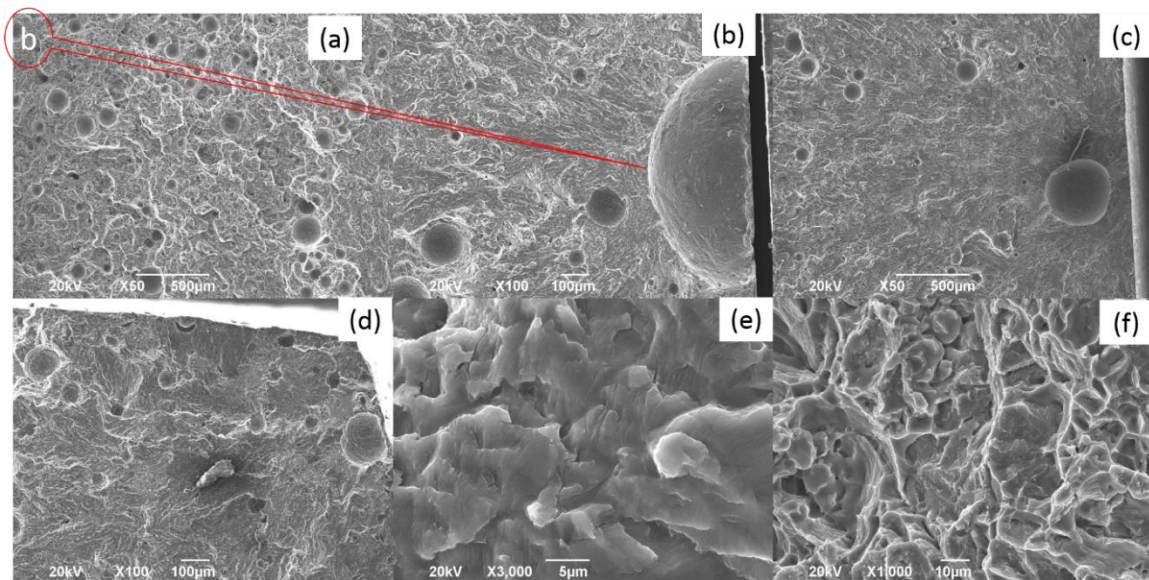


Figure 2-17 Fatigue fracture of the ER4043 joint, (a)~(d) crack initiation from pores close to the surface, (e) striation during the propagation period, (d) fracture period.

2.3.5 Corrosion resistance of the joint

Figure 2-18a shows the typical polarization curves of the welded joints and the BM. The values of corrosion potential (E_{corr}) and corrosion current (I_{corr}) are obtained from the polarization curves by the Tafel extrapolation method. As illustrated in *Table 2-6*, the FZ of the ER4043 joint has highest I_{corr} , $4.09 \times 10^{-6} \text{ A/cm}^2$, among the tested materials. The I_{corr} in the FZ of the ER5356 joint is slightly lower than that in the FZ of the ER4043 joint. The base metal shows the lowest value of I_{corr} . These results suggest that the BM has the best corrosion resistance, and that of the FZ of the ER4043 joint is poorest. The results of corrosion resistance of the ER4043 joint are constant with that in Ref. [33].

The typical stress-strain curves of the SSRT of the welded joint at room temperature are shown in *Figure 2-18b and c*. As seen from *Figure 2-18b*, the elongation and the tensile strength of the ER5356 joint are the same in air and 3.5 wt% NaCl solution. However, the elongation and strength of the ER4043 joint (*Figure 2-18c*) in 3.5 wt% NaCl solution are lower than those in air. To compare the susceptibility to stress strain cracking (SCC) of the two kinds of joints, the following equation described in Ref. [92] was used:

$$P_{SCC} = \frac{P_{NaCl}}{P_{air}} \quad \text{Eq. 2-2}$$

where P_{air} and P_{NaCl} are the values of the measured properties in air and 3.5 wt% NaCl solution, respectively, P_{SCC} is the SCC susceptibility indexed by the parameters of different properties. A lower P_{SCC} means higher SCC susceptibility. The measured properties and P_{SCC} are listed in

Table 2-7. Please note that the value in

Table 2-7 is the average of three tests under each condition. From

Table 2-7, the P_{SCC} of the ER4043 joint is lower than that in the ER5356 joint for all three properties, implying that the ER4340 joint is more prone to SCC.

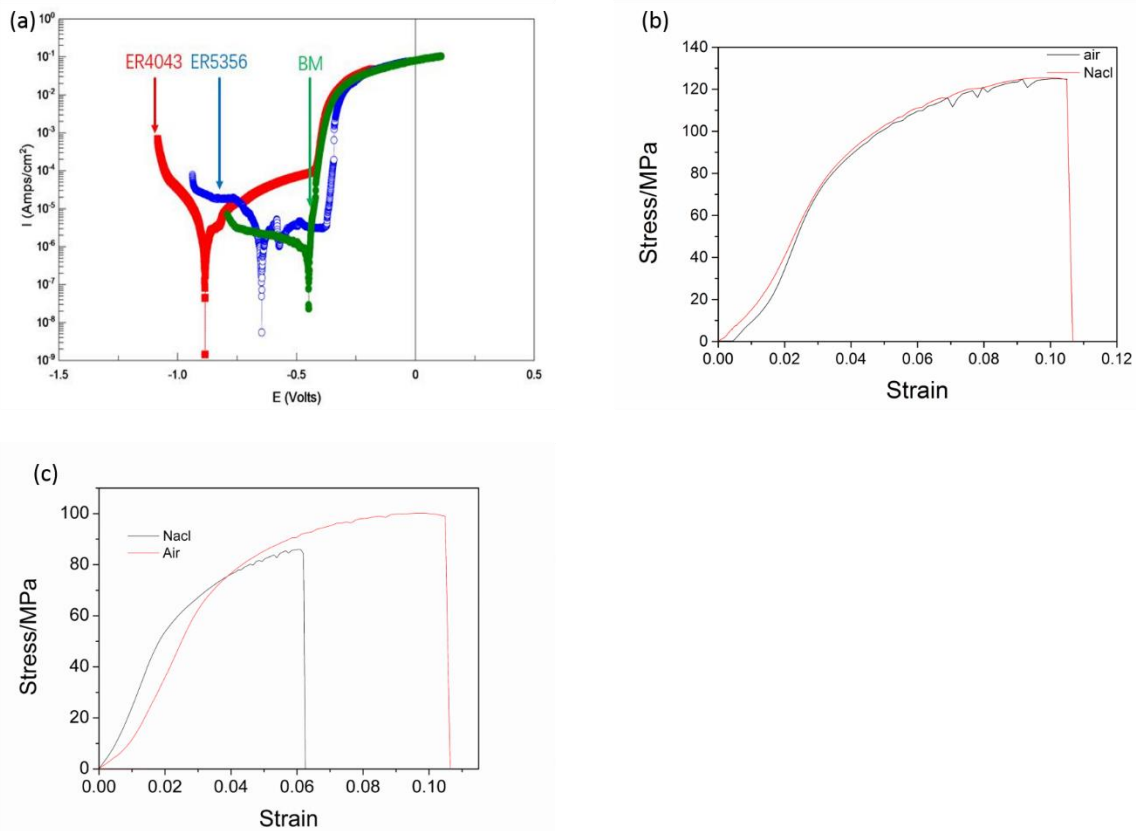


Figure 2-18 Corrosion test results of the welded joint, (a) polarization curves, (b) and (c) stress-strain curves of the ER5356 joint and the ER4043 joint in SSRT, respectively.

Table 2-6 Corrosion properties estimated from polarization curve.

Materials	E_{corr} (V)	I_{corr} (A/cm ²)
FZ of the ER4043 joint	-0.885	4.09×10^{-6}
FZ of the ER5356 joint	-0.647	3.88×10^{-6}
AA6061	-0.443	9.29×10^{-7}

Table 2-7 Measured properties from SSRT and P_{scc}.

Materials	Tested condition	UTS/MPa	P _{scc} in UTS	YS/MPa	P _{scc} in YS	Elongation/%	P _{scc} in elongation
ER4043 joint	Air	102	0.78	81	0.84	10.8	0.56
	3.5 wt% NaCl	80		68		6	
ER5356	Air	125	1.01	72	0.97	10.5	1.03

joint	3.5	126	70	10.8
	wt%NaCl			

2.4. Discussion

2.4.1 Microstructure and strength model

In the welding process, the microstructure of the welded joint is largely dependent on the thermal cycles, which are determined by the heat input. The heat input of the hybrid laser welding is from the laser and arc heat source. The heat input from the arc process is calculated as follows [93]:

$$Q_a = 0.75 \times \frac{A \times V \times 60}{v \times 1000} \quad \text{Eq. 2-3}$$

where A and V is the arc welding current and voltage, respectively, v is the welding speed.

The heat input from the laser is obtained from the equation [15]:

$$Q_l = 0.6 \times \frac{W \times 60}{v} \quad \text{Eq. 2-4}$$

where W is the laser power.

Applying the parameters in *Table 2-3* into *Eq. 2-3* and *Eq. 2-4*, the total heat input for the ER5356 and ER4043 joints are 20442 J/m and 20289 J/m, respectively. Although the heat inputs for the ER5356 and ER4043 joints are close to each other, the resulting microstructure is different. From Sections 2.3.1 and 2.3.2, the grain size in the FZ of ER4043 is smaller, but the microstructure has higher porosity and dislocation density. The difference may be attributed to the solidification process. In the hybrid laser welding process, the cooling rate is higher due to the higher welding speed and the microstructure is finer as a result. However, the fast cooling process leaves less time for the bubbles to escape from the surface of the welding pool, leading to higher porosity in the welded joint.

It is very difficult to measure the cooling rate of hybrid laser welding by an experimental method. (Perhaps molecular dynamic simulation could provide some clue). However, based on the EBSD results, the ER4043 joint has higher dislocation density and finer grain size. According to the work of Gao et al. [94], a faster cooling rate would result in higher dislocation density. Also, Bu et al. [95] indicated that higher dislocation density could be obtained with a faster cooling rate. The grain size could be finer with a rapid cooling process. There is supporting evidence for this proposition in the literature [96, 97]. Therefore, the cooling rate for the ER4043 joint may be higher than that for the ER5356 joint. Moreover, the cooling rate for welding can be given as [98] :

$$\frac{\partial T}{\partial t} = \omega \frac{\partial^2 T}{\partial x^2} \quad \text{Eq. 2-5}$$

where $T(x, t)$ is the temperature distribution function, which depends on coordinate x and time t , and ω is thermal diffusivity. It can be seen from the [Eq. 2-5](#) that the higher thermal diffusivity leads to a faster cooling rate. The thermal diffusivity for Al-Mg and Al-Mg-Si alloys is $\sim 4.4 \times 10^{-5} \text{ m}^2/\text{s}$ and $6.4 \times 10^{-5} \text{ m}^2/\text{s}$, respectively. Thus, the Al-Mg-Si alloy has a faster cooling rate.

The tensile test results suggest that the tensile strength of the joint could be improved by altering the filling materials. For Al alloys, the yield strength of the welded joint can be expressed by the equation [99, 100]:

$$\sigma_{total} = \Delta\sigma_{gb} + M \times [(\Delta\sigma_d + \Delta\sigma_p)^{1/2} + \Delta\sigma_0 + \Delta\sigma_{ss}] \quad \text{Eq. 2-6}$$

where σ_{total} is the yield strength of the welded joint, $\Delta\sigma_{gb}$ is the increment of grain boundary strengthening, M is the Taylor factor, $\Delta\sigma_d$ is the increment of dislocation strengthening, $\Delta\sigma_p$ is the increment of precipitation strengthening, $\Delta\sigma_0$ is the increment of intrinsic strengthening, $\Delta\sigma_{ss}$ is the increment of solid solution strengthening.

$\Delta\sigma_{gb}$ can be expressed by the Hall-Petch equation:

$$\Delta\sigma_{gb} = K \times d^{-\frac{1}{2}} \quad \text{Eq. 2-7}$$

where d is the grain size, and K is a material constant.

Impurity elements, such as Mg and Si, contribute to improvement of strength by solid solution strengthening. The contribution from such strengthening can be expressed as [101]:

$$\sigma_{ss} = \sum_j K_j C_j^{\frac{2}{3}} \quad \text{Eq. 2-8}$$

where C_j and K_j are the concentration and the scaling factor of the j^{th} alloying element, respectively. According to the EDS results, only Mg is considered as the solute element for the ER5356 joint, while Mg and Si are the solute elements for the ER4043 joint.

The following equation is used to express the strengthening from precipitation [101]:

$$\Delta\sigma_p = \frac{\bar{F}}{bL} \quad \text{Eq. 2-9}$$

where L represents the mean effective particle spacing in the slip plane, \bar{F} represents the mean obstacle strength. With Friedel formalism [102], L can be expressed by the mean particle size \bar{r} and the volume fraction f , then [Eq. 2-9](#) can be further written as:

$$\Delta\sigma_p = \frac{1}{b\bar{r}} (2\beta Gb^2)^{-\frac{1}{2}} \left(\frac{3f}{2\pi}\right)^{\frac{1}{2}} \bar{F}^{\frac{3}{2}} \quad \text{Eq. 2-10}$$

The mean obstacle strength, \bar{F} , can be expressed by [103]:

$$\bar{F} = \begin{cases} 2\beta Gb^2 \frac{r}{r_c}, & r < r_c \\ 2\beta Gb^2, & r > r_c \end{cases} \quad \text{Eq. 2-11}$$

where β is a constant, G is the shear modulus, r is the radius of the precipitate, r_c is the critical radius of shearing. As shown in [Eq. 2-11](#), the mean obstacle strength is determined by the particle/precipitate type, which is characterized by the radius of the precipitates. The

inequality, $r < r_c$, indicates weak particles, while strong particles are characterized by $r > r_c$. From the SEM results, r is greater than r_c from the present study, thus only the obstacle strength from the strong particle is considered.

The increment from dislocation strengthening can be obtained by [99, 104]:

$$\Delta\sigma_d = \alpha \times b \times G \times \sqrt{\rho} \quad \text{Eq. 2-12}$$

where α is a constant.

Making use of *Eq. 2-6* to *Eq. 2-12*, the total yielding strength of the welded joint can be expressed as:

$$\begin{aligned} \Delta\sigma_{total} = & Kd^{-\frac{1}{2}} + M\left\{\left[\frac{1}{b\bar{r}}(2\beta Gb^2)\left(\frac{3f}{2\pi}\right)^{\frac{1}{2}} + \alpha bG\sqrt{\rho}\right]^{\frac{1}{2}}\right. \\ & \left. + \sum_j K_j C_j^{\frac{2}{3}} + \Delta\sigma_0 \right. \end{aligned} \quad \text{Eq. 2-13}$$

With the parameters in *Table 2-8*, the contribution from each considered strengthening and the total yield strength for the two kinds of welded joints are shown in *Figure 2-19*. From the total yield strength, the predicted strength of the ER5356 joint is only ~ 8 MPa lower than the average yield strength from experiment, while for the ER4043 joint the predicted strength is 15 MPa lower than that from the experiment. But both predicted yield strengths are in the error range of the experimental yield strengths. This result indicates that our strength model can perfectly predict the yield strength of the hybrid laser-welded AA6061 joint. Moreover, from the quantitative calculation for each strengthening (*Figure 2-19*), the higher strength of the ER4043 joint is mainly attributed to the grain boundary strengthening and the solute strengthening. The lower increment from precipitation strengthening is possibly due to the coarsening formation of the particle during solidification.

The proposed model is built from the following perspectives:

- (1) As shown in *Figure 2-12c-d*, tensile test samples fracture in the FZ, and the most plastic zone is in the FZ. Based on this, it seems that the FZ withstands almost all the external load. Thus, almost all the yield strength present in the stress-strain curves is contributed from the FZ.
- (2) Based on the micron scale experiment which shows that only the FZ is deformed, as can be seen from *Figure 3-9*, the yield strength for the fusion zone is ~155 MPa. This is close to the predicted strength (159 MPa) from the strength model.
- (3) Based on the microhardness results (*Figure 2-11*), the average microhardness for the fusion zone is ~55 Hv, which is ~165 MPa flow strength according to the fact that the microhardness is one third of the flow strength [105]. This value is also very close the strength calculated from the model.

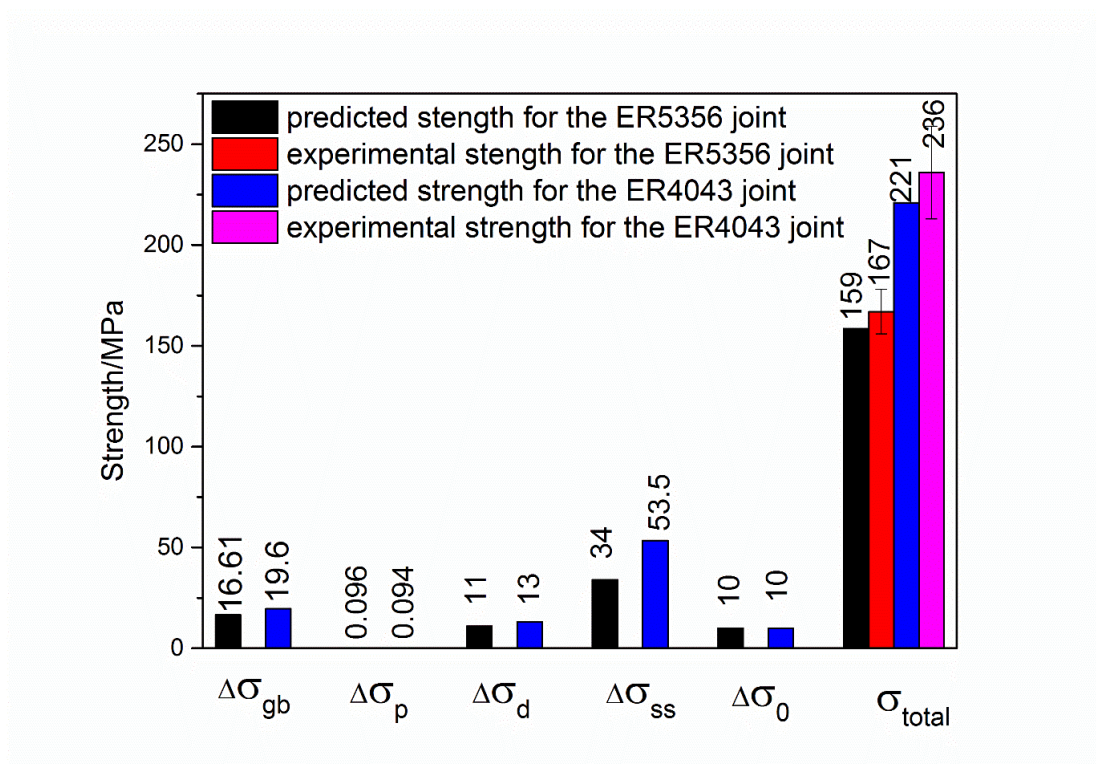


Figure 2-19 Predicted strength from the strength model from each considered strengthening mechanism.

Table 2-8 Input parameters for the strength model.

Description of parameter	Parameter	ER5356 joint	ER4043 joint	Origin
Constant in the expression of grain boundary strengthening	K	0.14	0.14	Ref. [106]
Grain size	D	71 μm	51 μm	Present study
Taylor factor	M	3.0	3.0	Present study
Magnitude of the Burgers vector	b	0.284 nm	0.284 nm	Ref. [101]
Mean particle size	\bar{r}	11.041 μm	11.471 μm	Present study
Constant in expression for the dislocation line tension in the precipitate strengthening	β	0.5	0.5	Ref. [101]
Shear modulus	G	26 GPa	26 GPa	Ref. [107]
Volume fraction of the precipitate	f	4.584%	4.499%	Present study
Constant in the expression of dislocation strengthening	α	0.5	0.5	Ref. [77]
Dislocation density	ρ	$9.19 \times 10^{12} \text{ m}^{-2}$	$1.32 \times 10^{13} \text{ m}^{-2}$	Present study
Scaling factor in the solid solution hardening model for Mg	K^{Mg}	29 MPa wt% ^{-2/3}	29 MPa wt% ^{-2/3}	Ref. [101]
Scaling factor in the solid solution hardening model for Si	K^{Si}	--	66.3 MPa wt% ^{-2/3}	Ref. [101]
Concentration of Mg	C_{Mg}	1.27%	0.34%	Present study
Concentration of Si	C_{Si}	--	0.46%	Present study
Intrinsic strengthening	$\Delta\sigma_0$	10 MPa	10 MPa	Ref. [108]

2.4.2 Fatigue and corrosion properties

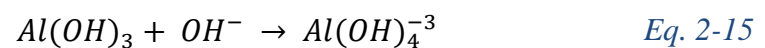
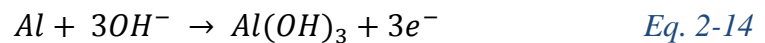
Although the ER4043 joint shows higher tensile strength than the ER5356 joint, the fatigue strength of the ER4043 joint is lower. Normally, the cyclic performance of materials

improves along with an increase in tensile strength, if the sample's surface condition is good and its fatigue behaviour is not governed by flaws/defects. However, if a defect or notch exists in the material, then the fatigue of materials would not be substantially improved with an increase in tensile strength. The fatigue performance of the weldment could be affected by several factors, such as external loading conditions (mean stress), material characters, surface condition, and the environment. Given that the external factors are the same for both tested joints, the only (or dominant) factor left is the material itself. As illustrated in *Figure 2-16* and *Figure 2-17*, the fatigue crack prefers to initiate from places surrounded by pores close to the sample surface.

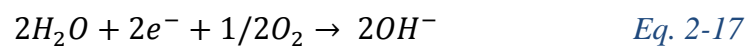
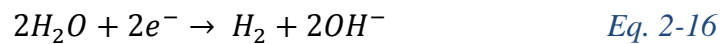
The effect of pores on the fatigue strength of aluminium alloys has been previously reported. Buffière et al. [109] used Synchrotron X-ray tomography and EBSD testing to identify the mechanism of crack initiation around pores. They found that the pore was the most crucial factor in reducing fatigue strength, especially at higher stress levels. Mayer [110] reported that 98.5% of the tested Al alloys cyclically failed with cracks initiated from pores. Gou et al. [27] studied the fatigue strength of welded AA7N01 joints with different porosity levels and found that the existence of pores was the main factor influencing the cyclic strength of such welded joints. Shen et al. [111] and Gaur et al. [112] also suggested that fatigue cracks of welded Al alloy joints preferred to initiate from pores, and they attributed this to the fact that pores could lead to high stress concentration under repeated loading conditions as demonstrated by a simulation method. Moreover, Wu et al. [113] studied the initiation and growth of the fatigue crack of a hybrid laser-welded AA7020 joint using synchrotron radiation X-ray computed microtomography and simulation. They reported that the pores close to the sample surface facilitated crack initiation. It can be concluded that pores can significantly reduce the fatigue strength of aluminium alloys and their welded joints. As can be seen in the fracture surfaces (*Figure 2-16* and *Figure 2-17*), there are more pores in the

ER4043 joint. As a result, a lower fatigue strength is shown.

The results of the potentiodynamic polarization and SSRT indicate that the ER4043 joint is more prone to corrosion attack. The aluminium alloys under NaCl solution would experience two corrosion processes, namely, anodic dissolution of Al and cathodic oxygen reduction (hydrogen evolution). The former process can be expressed by:



And the latter reaction is given as:



Ideally, the oxidized surface layer can protect Al alloys can be protected from being further corrosion. However, that layer is not stable and homogeneous, and contains flaws (i.e., pores, precipitates, and grain boundaries) where the localized corrosion potentials are different. Thus, the protective layer would be broken in the form of cathodic reaction from the site with flaws [114]. The localized corrosion potential difference is due to the elements added in the Al matrix, which form either solute solution or precipitates in the solidification process. Among the elements, Mg is known to reduce the corrosion potential of Al matrix, while Si, Cu and Fe tend to increase the corrosion potential [36]. During rapid solidification of the welding process, it is not possible for these elements to be evenly distributed in the Al alloys. As a result, the welded joint is susceptible to localized corrosion attack. The EDS results (*Figure 2-7*) show that, the Al matrix of the ER5356 joint contains Al and Mg elements whereas Al, Mg and Si are found in the ER4043 joint. The Si in the Al matrix partly increases the corrosion potential and destabilizes the protective oxide layer on the surface of the Al alloy [115], and accelerates the cathodic process [116]. Besides, more Si, Fe and Cu are

found in the precipitates in the ER4043 joint. It has been found [115] that the susceptibility of Al-Mg-Si alloys to corrosion attack depends on the Cu content, in that higher Cu content means lower corrosion resistance. The Fe-containing intermetallic/precipitate has higher cathodic activity than pure Al, leading to hydrogen evolution (see *Eq. 2-16*) occurring around Fe-rich particles [117]. Alkalization theory explains that the protective oxide layer would be dissolved during the localized alkalinity, and the matrix beneath the layer would be exposed and corroded. From the literature review, it can be concluded that the lower corrosion resistance of the ER4043 joint is attributable to the high content of Si, Fe and Cu in the joint.

2.4.3 Selection of the filling materials

One of the key interests in this thesis work is to provide useful information for selecting appropriate filling material when joining Al-Mg-Si alloys by hybrid laser welding. Choosing appropriate materials for particular structures is essential for design and innovation [118]. Conventionally, designers are mainly interested in the chemical and physical properties of the material. Thus, it is necessary to know the basic performance of the material. A summary of the main results from manufacturing to properties of the hybrid laser-welded joint with different filling materials is shown in *Table 2-9*. As indicated from the heat input, welding these two kinds of joints consumes the same amount of energy. In other words, there is no difference in manufacturing these two kinds of joints from the point of view of energy-saving and environmental issues. The ER4043 joint has higher tensile strength than the ER5356 joint, but the former has lower fatigue resistance due to pores within the joint. Although the ER4043 joint shows relatively poorer fatigue resistance, its fatigue strength is still higher than the design value recommended by the International Institute of Welding [119]. However, from the perspective of longer in-service life, the ER5356 joint is superior. The ER4043 joint may be suitable for structures designed for one-time usage, such as the rocket fuel tank [120].

The corrosion test demonstrates that the ER5356 joint is more corrosion resistant, suggesting that the ER4043 joint is not suitable for structures subjected to a corrosive environment (coastal cities).

Table 2-9 Summary of the main results from manufacturing to properties in this paper.

	The ER5356 joint	The ER4043 joint
Heat input (J/m)	20442	20289
Tensile strength (MPa)	258	307
Fatigue strength (MPa)	105	95
I_{corr} (A/cm ²)	3.88×10^{-6}	4.09×10^{-6}

2.5 Conclusions

In this chapter, comparisons were drawn between the ER5356 joint and the ER4043 joint from the aspects of microstructure, mechanical properties, fatigue and corrosion resistance.

The conclusions drawn are as follows:

- (a) A coarse microstructure with large dendritic precipitates and large grain size was found in both joints. But the ER4043 joint had more micropores, smaller grain size, and higher dislocation density.
- (b) The tensile strength of the ER5356 joint and ER4043 joint was 258 MPa and 307 MPa, respectively, indicating that the properties of the hybrid laser-welded AA6061 joint could be enhanced by altering the filling material. The tensile strength of the ER4043 joint reached up to 80% of the BM strength, which was stronger than that of the hybrid laser-welded joint.

- (c) A strength model was built from the strengthening mechanism to predict the yield strength of the welded joint. The model obtained accurately predicted the strength of both welds. From quantitative analysis, the higher strength of the ER4043 joint benefited from grain size and solid solution strengthening.
- (d) Despite the ER4043 joint showing higher tensile strength, its fatigue strength (95 MPa) was lower than that of the ER5356 joint (105 MPa). The dense pores were responsible for the marked loss of fatigue strength.
- (e) The ER4043 joint was prone to corrosion attack because of the higher content of Si, Fe and Cu in the FZ.

Chapter 3 Crystal plasticity of fusion zone in ER5 joint at microscale

3.1 Introduction

In this chapter, the microplasticity of the FZ in a hybrid laser-welded AA6061-T6 alloy joint was examined via micro-compression test of pillars with different orientations machined by FIB. Independent of orientation, the yield strength of the pillar is found to increase with the decrease of diameter when the diameter is less than 3.3 μm . Compared to size dependence of a pure Al, the size dependence is weaker due to the solute strengthening measured by the Dou-Derby power law. The crystalline orientation affects the yield strength, but the effect is reduced with a larger diameter. When the diameter of the pillar is greater than 3.3 μm , the dependence of yield strength on the pillar's diameter disappears. In this study, a transmission electron microscope, molecular dynamic simulation and theoretical modelling are used to investigate the dislocation behaviour, size and orientation effect on the microplasticity of the FZ at micro/submicro scales.

3.2. Experimental and simulation methods

3.2.1 Sample preparation

4mm-thick AA6061 aluminium alloys were joined using a hybrid laser-MIG welding system with ER5356 as the filling material (more details of the welding process can be found in Ref. [22]). The welding parameters were: $P_{\text{laser}}=2.2$ kW, $I_{\text{arc}}=173$ A, $v_{\text{welding}}=1.2$ m/min. After leaving the sample for some months to minimize the natural ageing effect on the mechanical properties, a rectangular block of about 1 mm³ in size was cut from the centre of the FZ and mounted using resin. The sample was then metallurgically ground and polished with the last step being finished with 0.02 μm colloidal silica to remove the deformed layer on the sample surface. The well-polished sample was thus ready for the EBSD test and micropillar compression tests.

Cylindrical pillars were made by FIB using FEI Helios 600 Nanolab. All pillars were machined at 30 kV with currents ranging from 9 nA to 0.21 nA for coarse milling and 45 pA for fine polishing to minimize the Ga⁺ damage on the surface of the pillar. The pillar diameter ranged from 0.4 μm to 6.8 μm. The pillars' aspect ratios of height-to-diameter were kept between 3:1 and 4:1. To study the effect of orientation on the pillar strength, orientations of [101], [111] and [-301], were selected. Since the phases in the FZ could be etched away during the FIB milling, all pillars were machined in the area without phases, so only solid solution strengthening was considered in the microstructure of the pillar.

A TEM sample of the bulk FZ was prepared by ion polishing method in a PIPS system. A different method was used to make TEM samples from the pillars after deformation. The procedure for the FIB-based method to make the TEM samples is shown in *Figure 3-1*. Basically, a thin protective layer of Pt was first deposited on the surface of the pillar. Then FIB was applied to cut the pillar along the cross section until the thickness was below 100 nm. An ex-situ method was used to transfer the sample to a TEM grid for later TEM observation.

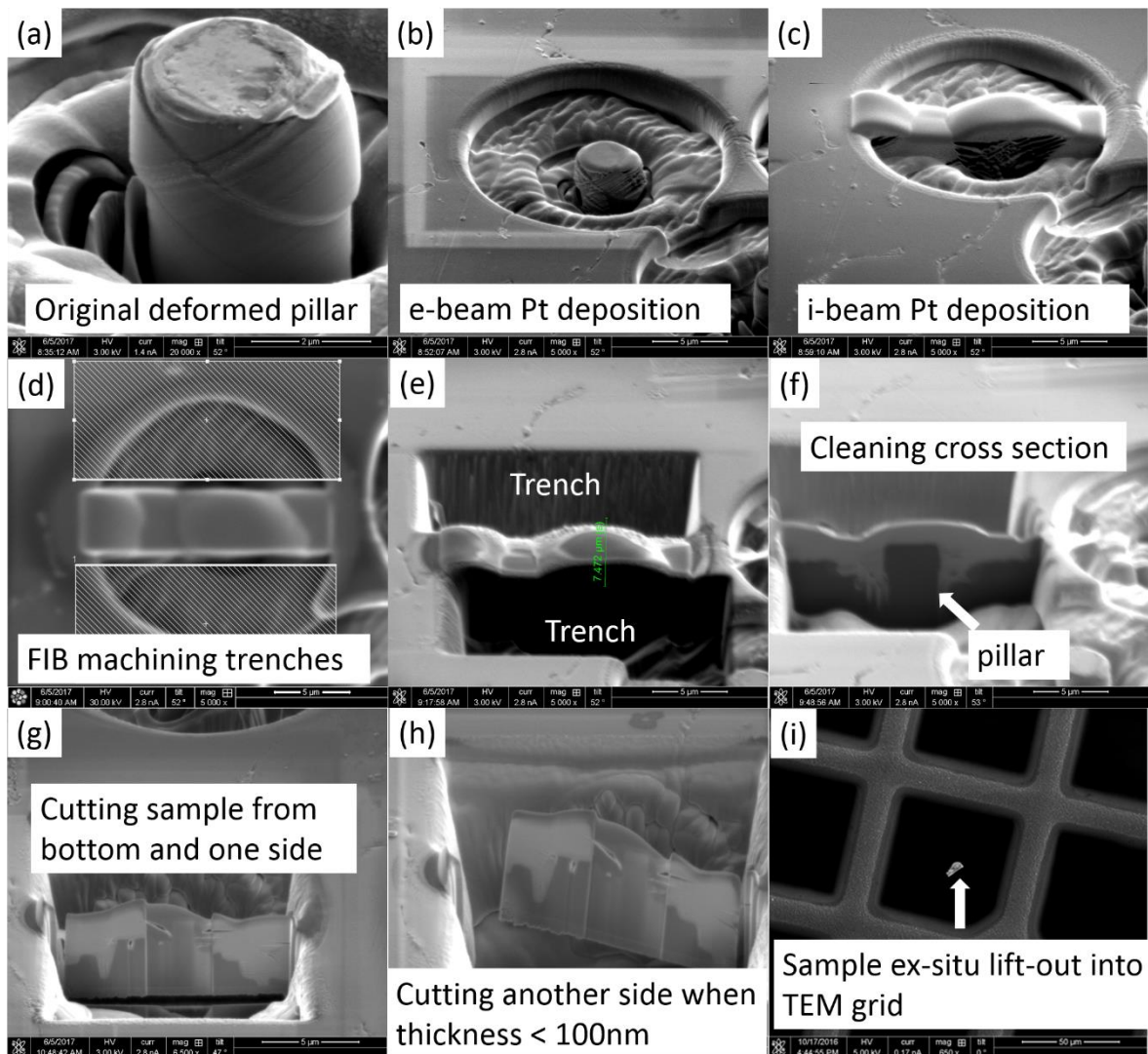


Figure 3-1 Procedure for TEM sample preparation using FIB.

3.2.2 Microstructure characterization

The microstructure of the sample was observed using a FESEM. The chemical composition of the matrix was measured using EDS. The EBSD test was performed utilizing the parameters as in Ref. [22]. The TEM experiment was performed using a JEOL 2100F microscope at the acceleration voltage of 200 KV to observe the microstructure of the bulk material and the deformed pillars.

3.2.3 Compression test

Compression tests were conducted by a nanoindenter (TriboIndenter TI900, Hysitron) with a 9 μm -diameter flat punch. All tests were carried out under displacement-control mode with the strain rate being $1 \times 10^{-3} \text{ s}^{-1}$. The most difficult part of the nano/microscale compression test was finding the position of the sample accurately. As shown in *Figure 3-2a*, the pillar was first located using the optical microscope in the nanoindenter, and then the tip (*Figure 3-2b*) was moved to the top of the pillar and the pillar was compressed. However, this process could not guarantee that the pillar was fully compressed. Mostly, the pillar was bent instead of compressed, as shown in *Figure 3-3*. This was because of the misalignment between the optics and the punch, despite calibration between the optics and punch being performed before the test. To overcome this problem, an in-situ imaging method was devised, using the tip to locate the pillar precisely. The basic procedure was that: (a) find the pillar with the optic microscope, (b) move the tip to the top of the pillar, (c) use the in-situ imaging method to obtain the location of the pillar. After successfully locate the pillar, the tip was disengaged for ~ 40 mins to reduce the thermal drift below 0.05 nm/s. The stress value at the first strain burst was the yield strength of the pillar. At least three samples were made for each condition. SEM images of the pillars were taken before and after the testing to obtain the dimension and the deformed morphology.

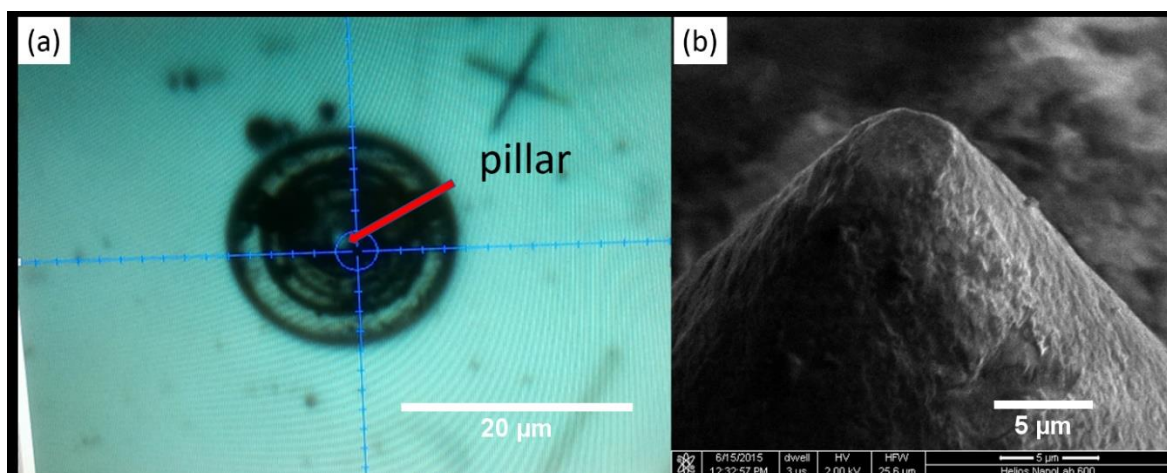


Figure 3-2 (a) Top view of a pillar under optical microscope in the nanoindenter, (b) flat-end punch for the compression test.

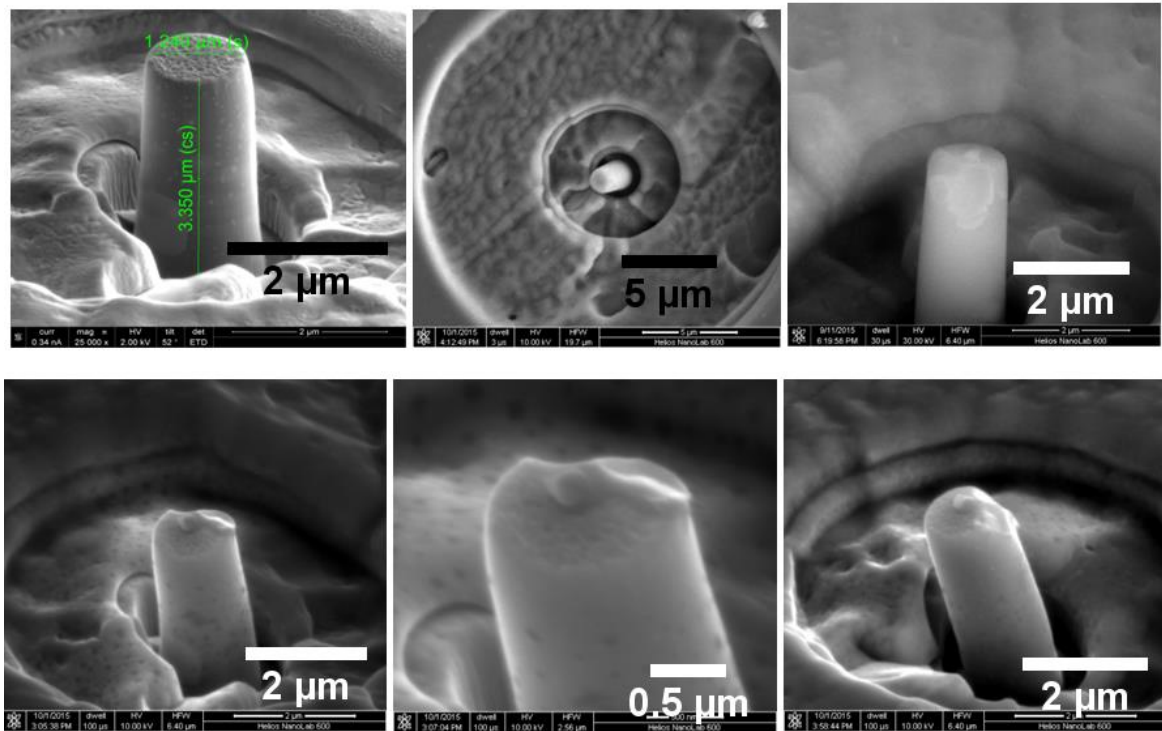


Figure 3-3 Figures showing the sample bent instead of compressed during nanoindentation.

3.2.4 Molecular dynamic simulation

To understand the influence of orientation on the deformation and dislocation behaviour at atomistic level, molecular dynamic (MD) simulation [121-127] was performed using a Large Scale Atomic/Molecular Massively parallel Simulator (LAMMPS) [128] with the potential presented in [129]. The model for the compression in MD simulation is shown in *Figure 3-4a*. The nanopillar was of 33 nm in height with the diameter of 11 nm, with a ratio of height-diameter of 3:1 that was close to the experimental condition. Mg atoms were randomly distributed in the pillar at the concentration of 1.27% (atomistic weight), which was the same as the results from EDS tests. Before compression, the nanopillar was first relaxed by energy minimization (conjugate gradient method), then equilibrated by MD in an isobaric-isothermal (NPT) ensemble at the pressure of 0 bar and temperature of 300 K for 100 ps. A constant strain rate of $1 \times 10^9 \text{ s}^{-1}$ was applied along the x axis at the temperature of 300 K under NPT conditions with periodic boundary conditions for all three directions. The

timestep for the simulation was 1 fs. The results were visualized with Ovito software [130]. Common neighbour analysis (CNA) [131] techniques were used to identify the defect structure and its evolution during the simulations. The dislocation extraction algorithm (DXA) [132] was used to analyse the dislocation behaviour during the compression.

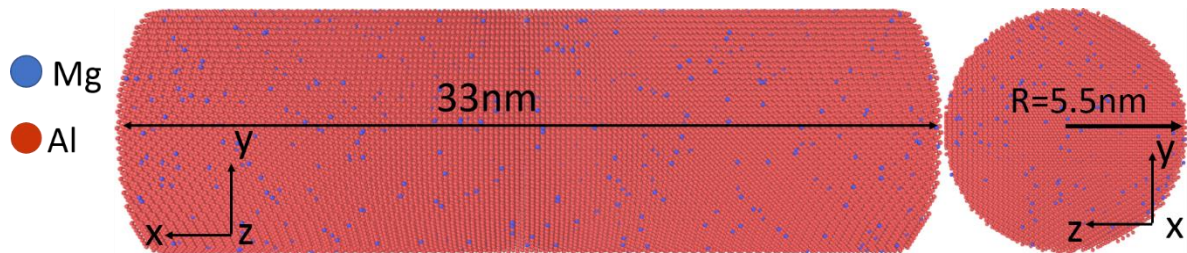


Figure 3-4 Nanopillar for MD simulation.

3.3. Results

3.3.1 Microstructure analysis of the FZ of bulk samples

The microstructure was discussed and displayed in chapter 2. For completion, the microstructure is shown below. The typical microstructure images of the FZ in the welded joint are shown in *Figure 3-5a*. From *Figure 3-5a*, coarsened dendritic-shaped phases can be seen in the matrix. To know the chemical compositions of the matrix, EDS test was conducted for the points shown in *Figure 3-5a*. The EDS results (*Figure 3-5b*) show the matrix has the elements of Al and Mg. *Figure 3-6* shows the representative TEM images of FZ. Similar to the SEM results, the big particles (*Figure 3-6a*) could be seen on the matrix, but fine particles (*Figure 3-6b*) could also be seen in the matrix in some places.

The EBSD results of the FZ are shown in *Figure 3-7*. *Figure 3-7a* shows equilibrated grains with the grain size of $71 \pm 53 \mu\text{m}$ in the FZ. Since the welded joint is not subjected to any post-welding treatment (such as rolling), there are no textures in the FZ, as demonstrated in the pole figures (*Figure 3-7c*). As the size effect in the micron/submicron scale is dependent on

the dislocation density, the EBSD results (*Figure 3-7b*) were also used to evaluate the dislocation density in the FZ to identify the initial dislocation density. The dislocation density (ρ) was calculated by [133]:

$$\rho = \frac{\theta_{KAM}}{|b| \mu n} \quad \text{Eq. 3-1}$$

where θ_{KAM} is the kernel average misorientation angle, b is the magnitude of the Burgers vector, μ is the step size of the EBSD test, and n is the number of nearest neighbours. Taking $b=0.3$ nm (magnitude of the Burgers vector), $\mu=3$ μm , $n=2$, and $\theta=0.897^\circ$, the calculated dislocation density of the welded joint is $9.19 \times 10^{12} \text{ m}^{-2}$.

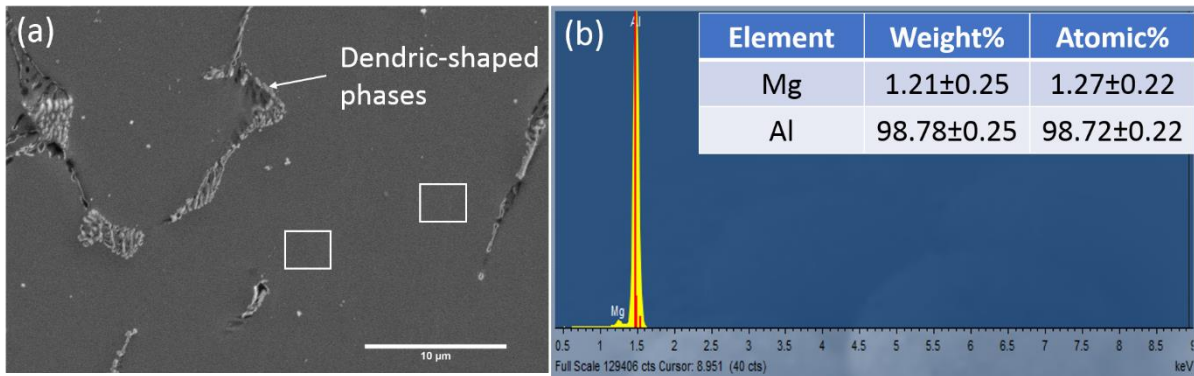


Figure 3-5 (a) SEM image of the microstructure of the FZ, (b) EDS results for the areas indicated in (b) with white boxes.

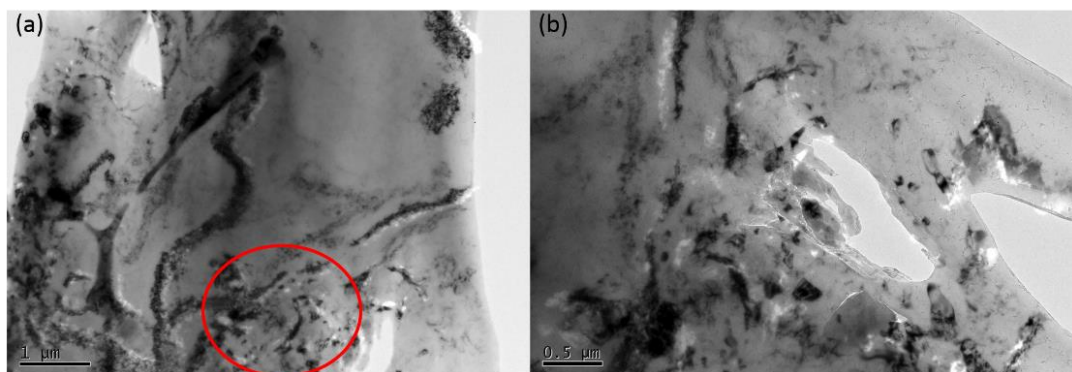


Figure 3-6 TEM images for the bulk in the FZ, (a) coarsened phases, (b) fine phases in the area indicated in (a) by a red circle.

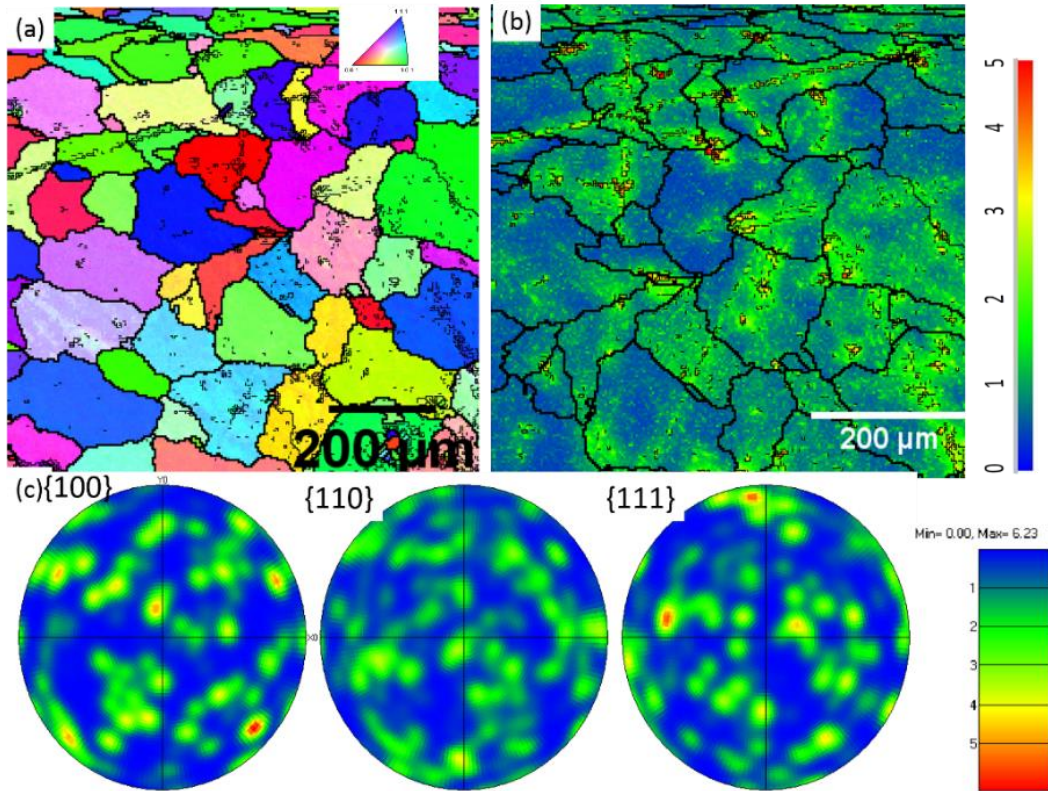


Figure 3-7 EBSD test results for the FZ, (a) IPF image, (b) KAM image, (c) PF image [22].

3.3.2 Micropillar compression

As shown in the SEM images (*Figure 3-8*), double slips can be observed for the [101]-oriented pillars with diameters from 400 nm to 6.8 μm . It can also be seen from *Figure 3-8a-b* that the slip in orientation [101] was not affected by the sample diameter in this study, a finding different from previous reports [81, 134]. The difference may be due to microstructure factor (alloying composition, orientation and dislocation density). In contrast to the [101]-oriented sample, the morphology of the compressed [111]-oriented sample was influenced by the sample's diameter. In the 400 nm-diameter sample (*Figure 3-8c*), only localized wavy slip lines can be seen on the surface. But in larger samples (*Figure 3-8d*), a single slip band could be seen on the surface.

Figure 3-9a-b shows representative stress-strain curves from the uniaxial compression of pillars with two orientations in the FZ. Discrete stochastic bursts can be seen after reaching

the yielding point in the stress-strain curves, which is much like the strain burst of the SC of pure FCC metal and is independent of orientation. As illustrated in *Figure 3-9c*, the strength increases as the diameter of the pillar ($\leq 3.2 \mu\text{m}$) decreases for both orientations, showing a “smaller is stronger” trend, with 400 nm-diameter pillars having the highest strength of ~ 310 MPa in the [101]-oriented pillar and ~ 440 MPa in the [111]-oriented pillar. The results illustrate that the orientation can influence the strength of the FZ at micron/submicron scale. For samples with diameter greater than $3.2 \mu\text{m}$, the size effect on the yield strength is ineffective for both orientations, indicating that the yield strength for diameter greater than $3.2 \mu\text{m}$ has the same value as that of the bulk, and the critical length for the size effect in this study is $3.2 \mu\text{m}$. It is also interesting thing that the orientation effect on the yield strength reduces along with the increase in the sample’s diameter (see *Figure 3-9c*).

The stress-strain curves for all tested pillars present discrete strain bursts, known as strain hardening. Here the hardening angle [135] is used to explain the strain hardening behaviour. In the present case, the hardening angle is measured from the stress-strain curves with the yielding strength point and 5% flow stress point as the starting point and ending point, respectively. The results are illustrated in *Figure 3-9d*. The hardening angle for the tested pillars falls within the range of $12.5\sim 26^\circ$, which is much higher than that of the single crystal in pure Al [135]. The large hardening angle indicates that there is dislocation action (i.e., dislocation storage). The hardening angle appears to be slightly size- and orientation-dependent, with the greatest [111]-oriented pillar showing the highest angle. This observed phenomenon can be explained as resulting from the dislocation storage in the pillar. In the larger pillar, the dislocation needs to travel a long distance to escape from the sample surface, increasing the likelihood of dislocation interaction, and the dislocation density. In the smaller pillar, however, the dislocation has greater likelihood escaping from the surface, resulting in lower dislocation density.

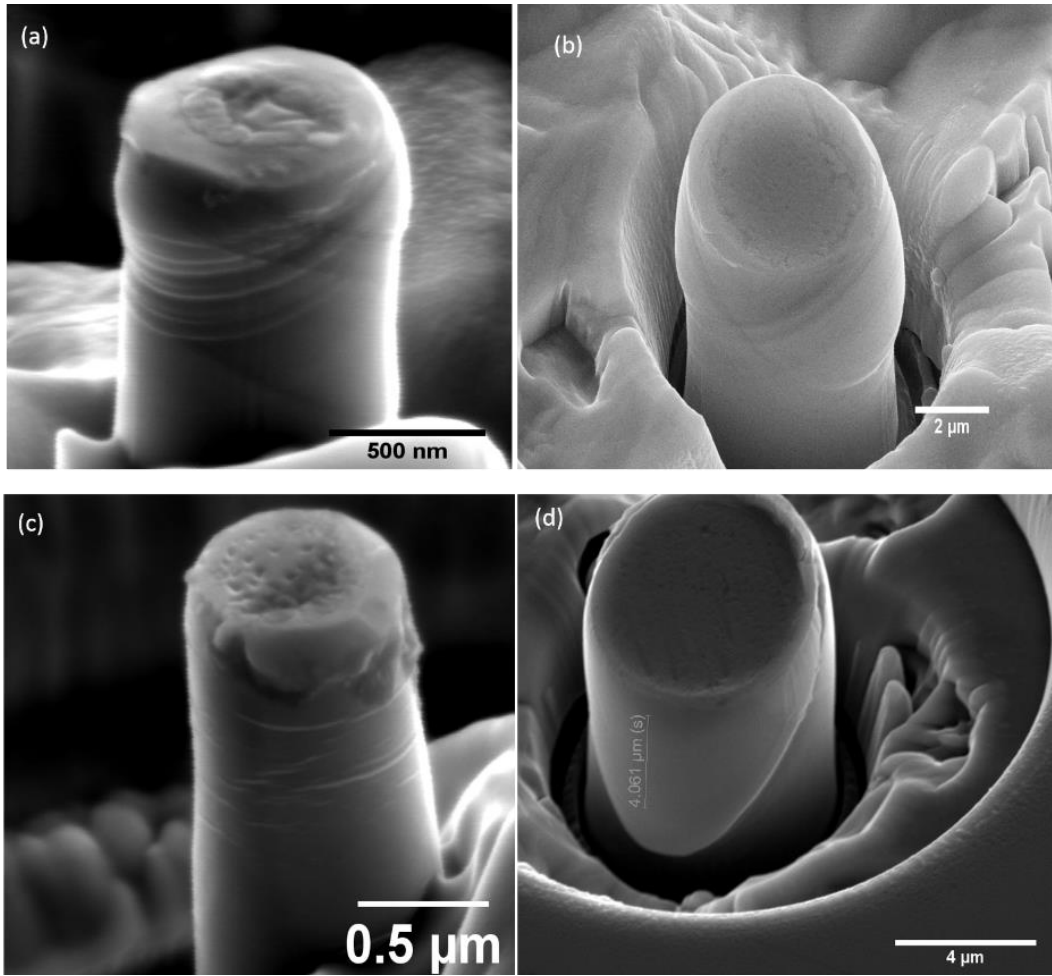


Figure 3-8 Representative images of the pillars after compression, (a) 800 nm-diameter pillar with orientation [101], (b) 6.8 μm-diameter pillar with orientation [101], (c) 800 nm-diameter pillar with orientation [111], (d) 6.8 μm-diameter pillar with orientation [111].

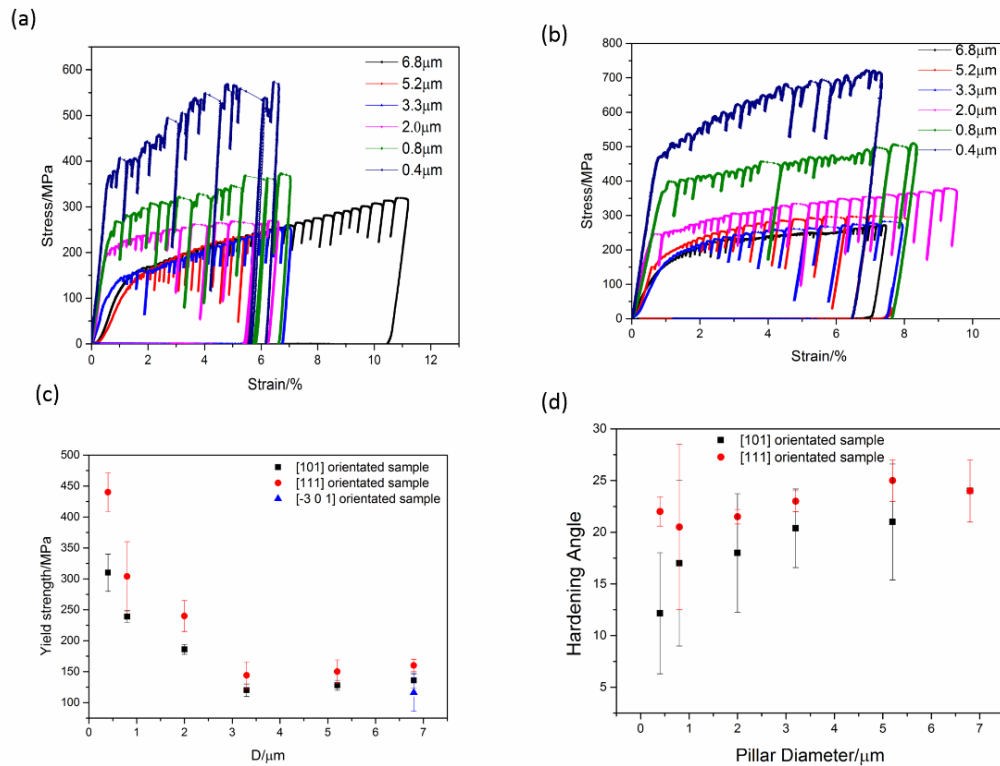


Figure 3-9 Representative stress-strain curves of (a) [101]-oriented pillars and (b) [111]-oriented pillars; (c) yield strength vs. diameter for the tested pillars with different orientations, (d) hardening angle vs. pillar diameter for the tested orientation.

3.3.3 Dislocation behaviour

Figure 3-10 shows TEM images for the deformed [101]-oriented 800 nm-diameter sample. As illustrated in Figure 3-10a, the TEM sample was taken along the cross section of the pillar. Figure 3-10b shows that most of the deformation occurs at the top of the pillar and the strained parts are parallel to each other along the slip direction. From the enlarged view (Figure 3-10d), most of the dislocations are distributed in the centre, with the area near the sample's surface being dislocation-free. But the inverse fast Fourier transform image (Figure 3-10f) shows that there are lattice distortions, meaning that the dislocation existed before deformation and escaped from the surface during deformation. The dislocation in Figure 3-10g can be seen on the slip plane, and close to the surface. This may be due to two reasons: (a) the cross slip locked the dislocation (Figure 3-10c), (b) the dislocation was annihilated

during compression. As reported previously [136, 137], the FIB milling could damage the surface of the sample, leading to an amorphous layer or dislocation strengthening on the surface. As shown in *Figure 3-10c*, the damaged layer is only ~9.6 nm with a fine current (48 pA) during the FIB milling.

Figure 3-11 shows dark-field TEM images for the [111]-oriented 800 nm-diameter sample. The bright areas in *Figure 3-11b* are the main deformed parts of the pillar. The enlarged view of the area (*Figure 3-11c-d*), shows the dislocation lines in the deformed sample. Comparing the TEM results for both orientations, it seems that the [111]-oriented sample has greater dislocation density than the [101]-orientation sample. The method described in Ref. [138] was used to measure the dislocation density in the deformed pillar. The calculated dislocation density for the [101]- and [111]-oriented 800 nm-diameter samples was 3×10^{14} and 5.32×10^{14} m^{-2} , respectively. The lower dislocation density in the [101]-orientated pillar was possibly due to more slip events occurring during compression. More details are discussed in Section 3.3.4.

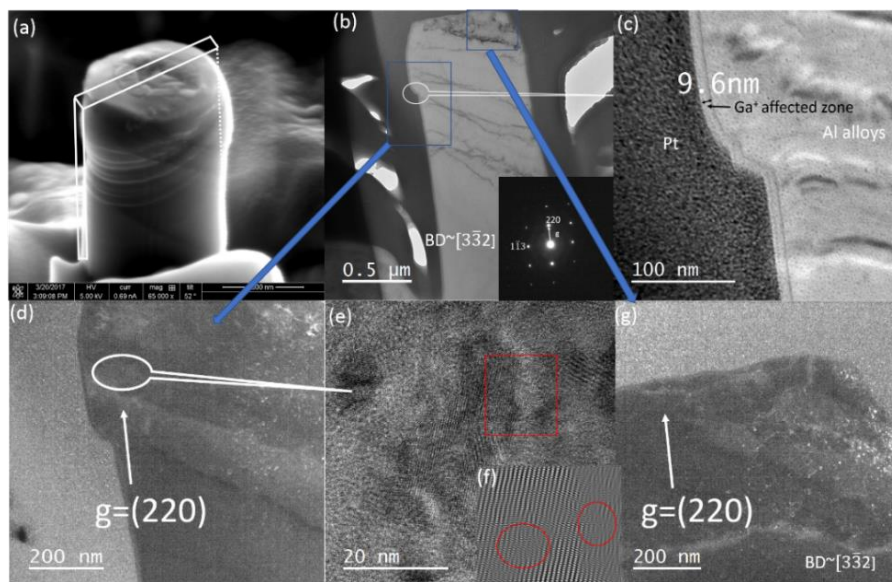


Figure 3-10 (a) Indication of TEM sample machined by FIB, (b) overview of the strained area (dark line), (c) Ga+ damaged zone, (d)-(g) dislocation and lattice distortion in the deformed pillar.

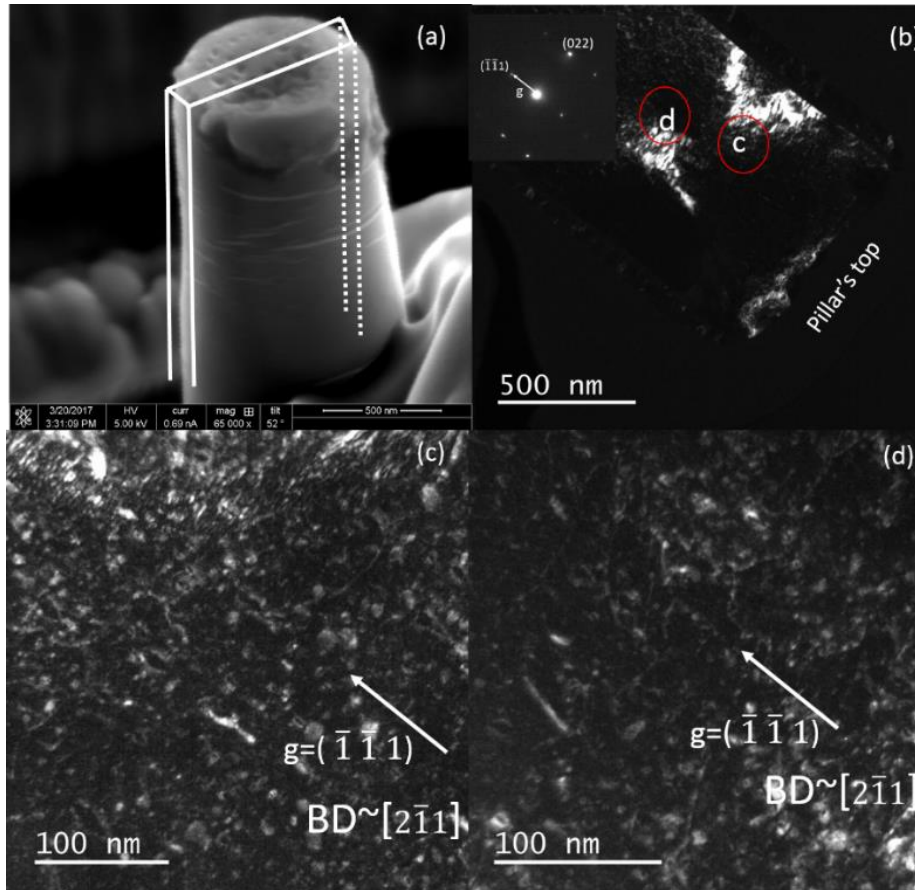


Figure 3-11 (a) Indication of the TEM sample machined by FIB, (b) overview of the strained area (bright areas), (c)-(d) dislocations in the deformed area as indicated in (b) by red circles.

3.3.4 Molecular dynamic simulation

The stress-strain curves for the orientations [111] and [101] are shown in *Figure 3-12a*. As in the experimental results, the [111]-oriented nanopillar shows greater yield strength than that of the [101]-oriented pillar. However, after yielding, the flow stress of the [101]-oriented nanopillar fluctuates over a wide range (0.12 GPa to 2 GPa), whereas the flow stress of the [111]-oriented nanopillar is much less variable. The fluctuation of the flow stress after yielding is due to the dislocation behaviour [139]. The dislocation density for both orientations during compression is shown in *Figure 3-12b*. In the plastic strain, the dislocation density in the [111]-oriented pillar is higher than that of the [101]-oriented pillar, a finding which is consistent with the experimental results (*Figure 3-10* and *Figure 3-11*).

The detailed microstructure of the pillar under compression was studied from snapshots. *Figure 3-12c* presents the snapshots for the [101]-oriented sample. From those snapshots, most of dislocations move along the stacking fault and then annihilate from the surface. With the formation of cross slip (*Figure 3-12c*), some dislocations are locked in the crossed area while no dislocations exist on the slip plane, indicating that dislocations escape from the surface during the slip. For the [111]-oriented sample (*Figure 3-12d*), the stacking faults are distributed on the {111} planes bounded with perfect and partial dislocations. As shown in *Figure 3-12d*, dislocations entangle with each other, making it difficult for them to escape from the surface. As a result, the dislocation density increases. Further, since there are too many slip directions and planes in the [111] sample (*Figure 3-12d*), the annihilation of the dislocation is multi-directional, resulting in a wavy surface.

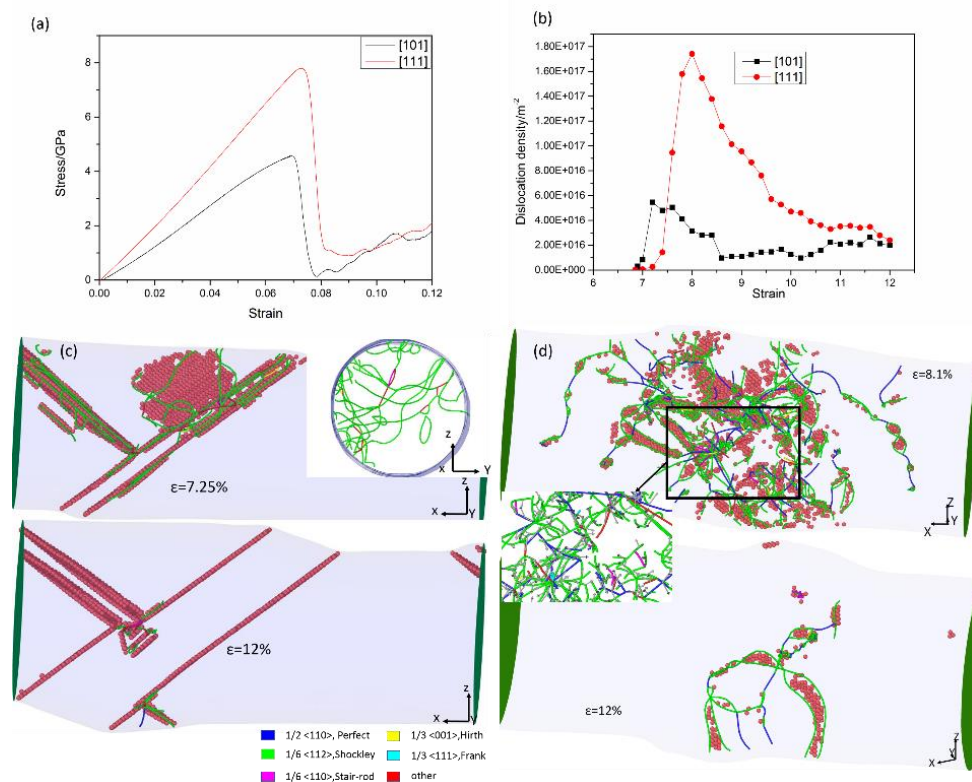


Figure 3-12 MD simulation results, (a) stress-strain curves for orientations [101] and [111], (b) dislocation density during compression, (c) snapshot of microstructure evolution in the [101]-oriented sample under compression, (d) snapshot of microstructure evolution in the [111]-oriented sample under compression.

3.4. Discussion

3.4.1 Orientation effect

As shown in *Figure 3-9c*, the yield stress of the micron/submicron pillar in the FZ is orientation-dependent, with the [111] orientation having the highest yielding stress. The TEM images from the bulk show that the size and space of the phase in the FZ are quite large, so it is unlikely to include the phase in the pillar, as demonstrated in *Figure 3-10b*. Thus, it is reasonable to consider the pillar made from the FZ as a kind of FCC solid-solution material, of which the slip system(s) would be the one(s) having the highest Schmid factor among the {111} <110> slip systems. From the EBSD test, the Schmid's factors of orientation [101], [111] and [-301] are 0.44, 0.32 and 0.5, respectively. Thus, the [111] pillar shows the highest stress when subjected to uniaxial loading.

The finding about the orientation effect on the strength at micro/submicro scales is consistent with that from Hagen et al. [140]. They reported that the strength of α -Fe with orientation [011] was greater than that of [010]. But the present finding differs from the report of Frick et al. [141], that a single crystalline Ni in orientation [111] with fewer slip systems had lower critical resolved shear stress (CRSS) than that with orientation of [269] with more slip systems. They attributed this interesting phenomenon to the possibility that there might have been more available slip planes for the [111] Ni at micro/submicro scales, which is contrary to Schmid's law. It has also been reported that the orientation has no effect on the CRSS at micro/ submicro scales, such as Nb [142]. These studies demonstrate that Schmid's law could break down at nanoscale [143]. At micro/ submicro scales, the yielding strength is determined by the activated dislocation source. In other words, the slip system with lower Schmid factors could be involved in the deformation.

Another interesting finding is that the orientation effect on the yield stress decreased with the increase of the pillar's diameter. As shown in *Figure 3-9c*, the yield stress due to the orientation effect could be as high as ~115 MPa (0.4 μ m-diameter sample) or as low as ~25 MPa (samples with diameter greater than 3.3 μ m). The change may be attributed to the size effect. As shown in *Figure 3-13a-b*, the contribution of dislocation-source strengthening decreases with the increase of the sample's diameter. The dislocation-source strengthening is only about 5 MPa when the diameter is greater than 3.3 μ m but could be as high as 110 MPa with the diameter of 0.4 μ m.

3.4.2 Flow strength

The flow shear stress of the sample in this study can be expressed as:

$$\tau_{total} = \tau_{fs} + \tau_{ss} + \tau_d + \tau_{source} \quad \text{Eq. 3-2}$$

where τ_{total} is the total shear stress, τ_{fs} is the friction stress that is taken as 0 [143], τ_{ss} is the solid solution strengthening, τ_d is the strengthening from dislocation-dislocation interactions, τ_{source} is the dislocation source-controlled strength that is related to the size effect. The solid solution strengthening can be given as [144]:

$$\tau_{ss} = \sum_j K_j C_j^{\frac{2}{3}} \quad \text{Eq. 3-3}$$

where C_j and K_j is the concentration and the scaling factor of the j^{th} alloying element, respectively. According to the EDS results, only Mg can be considered as the solute element for the joint. Taking $K=29 \text{ MPa wt\%}^{-2/3}$ [144], $C_{\text{Mg}}=1.21\%$, the resulting solid solution strengthening (τ_{ss}) is 33MPa.

The strengthening contribution from dislocation interaction (τ_d) can be quantitatively described as [145]:

$$\tau_d = \alpha \cdot b \cdot \mu \sqrt{\rho_{total}} \quad \text{Eq. 3-4}$$

where α is a constant, b is the magnitude of Burgers vector, μ is the shear modulus, and ρ is the total dislocation density. Since the mobile dislocation in the small-scale sample prefers to escape from the sample's surface, the increment of dislocation density during compression is taken to be 0 in this study. Taking $\alpha=0.5$ [77], $b=0.3$ nm [143], $\mu=26$ GPa [143], $\rho=9.19 \times 10^{12}$ m⁻², the increment obtained from the dislocation strength is 11 MPa.

As suggested by Parthasarathy et al. [77], the doubled-ended sources in the micron pillar would become single-ended due to interaction with the free surface. The stress to activate the single-ended source dislocation (τ_{source}) can be given as:

$$\tau_{source} = \frac{K\mu b}{\bar{\lambda}} \quad \text{Eq. 3-5}$$

where k is equal to 1 [77], μ is the shear modulus, b is the magnitude of the Burgers vector, $\bar{\lambda}$ is the effective source length, which can be obtained by:

$$\begin{aligned} \bar{\lambda} = & \int_0^R \left[1 - \frac{\pi(R-\lambda)(a-\lambda)}{\pi R a} \right]^{n-1} \\ & \times \left\{ \frac{\pi[(R-\lambda) + (a-\lambda)]}{\pi R a} \right\} n \lambda d\lambda \end{aligned} \quad \text{Eq. 3-6}$$

where R is the radius of the sample, a is given as $a = \frac{R}{\cos \beta}$ (β is the angle between the primary slip plane and the applied stress axis), for our case β is 35.3° and 90° for [101]- and [111]-oriented samples respectively; n is the pinning number determined by the sample dimension and initial dislocation density, as obtained by:

$$n = \text{Integer} \left[\frac{\pi D^2 \rho_{total}}{8} \right] \quad \text{Eq. 3-7}$$

where ρ_{total} is the total dislocation density, D is the diameter of the pillar.

Using *Eq. 3-2* to *Eq. 3-7*, the total flow stress can be expressed as:

$$\tau_{total} = 44 + \frac{\mu b}{\int_0^R \left[1 - \frac{\pi(R - \lambda)(a - \lambda)}{\pi R a}\right]^{n-1} \times \left\{ \frac{\pi[(R - \lambda) + (a - \lambda)]}{\pi R a} \right\} n \lambda d\lambda} \quad \text{Eq. 3-8}$$

The calculated τ_{total} is shown in *Figure 3-13a-b* together with the experimental results. The experimental results are about 20~30 MPa higher than the calculated ones, especially for the 0.8 μm -diameter and 2 μm -diameter samples. This finding is consistent with the previous report on small-scale research in alloys [81]. The discrepancy between the calculation and the experiment may be due to underestimation of the bulk strength:

- (1) Underestimation of the friction stress, because the solute atom Mg can significantly cause lattice distortion due to misfit volume and elastic mismatch between Al and Mg atoms.
- (2) Some other solute elements might not be detected using EDS, such as Fe (existing both in the base metal and filling material). It has been reported [146] that element Fe has an important influence on solute strengthening, even if its concentration is less than 3 ppm. But such low concentration is beyond the accuracy of the EDS used in our study.

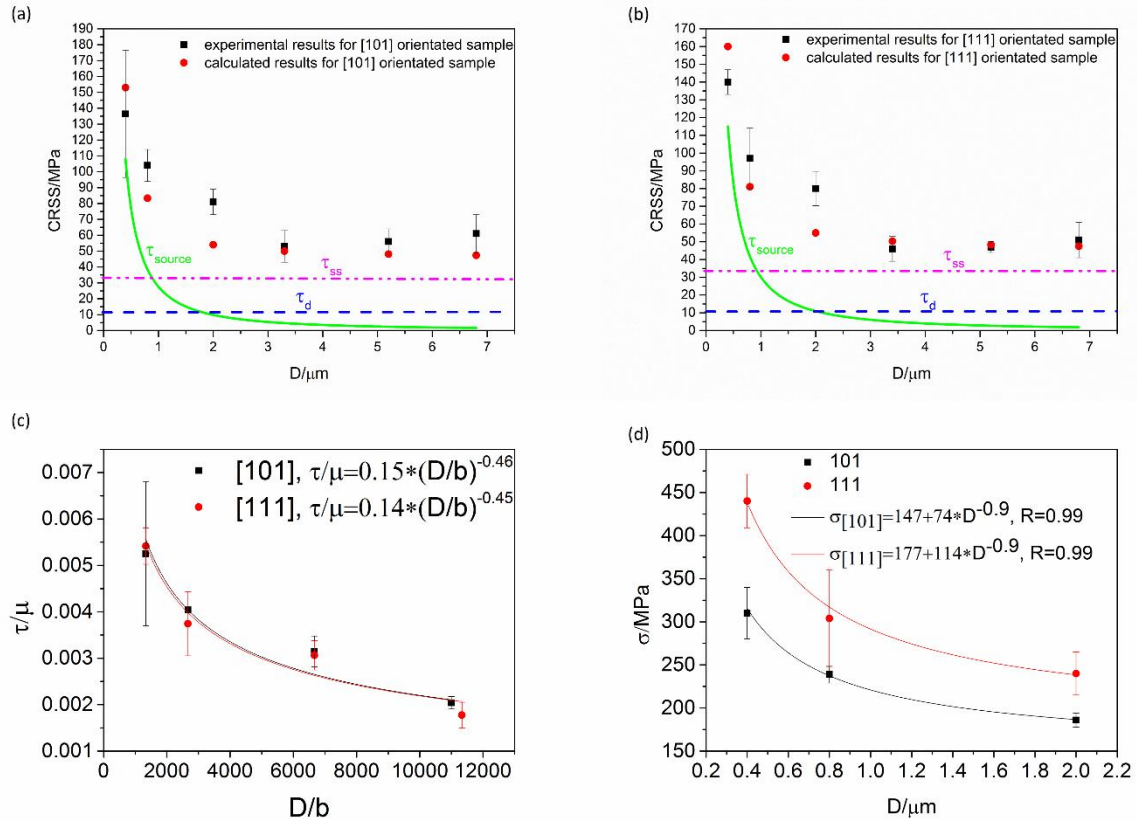


Figure 3-13 Calculated critical shear stress according to Eq. 3-15 for (a) orientation [101] and (b) orientation [111]. The red points are the calculated CRSS, while the black points are the experimental ones. The contribution to the strength from τ_{source} , τ_{ss} , and τ_d is illustrated by green, magenta and blue dashed lines, respectively. (c) The normalized strength vs. normalized diameter for the tested pillars in this study, (d) yield strength vs. diameter for orientations [101] and [111].

3.4.3 Strength from micropillar to bulk

One of the key foci in this study is extracting macroscopic mechanical properties from small-scale testing, such as the yield stress, which can be used in the design and assessment of the structure of Al alloys joined by hybrid laser welding. As can be seen from *Figure 3-9c*, all the samples from both tested orientations exhibit the trend of “smaller is stronger”. As suggested by Dou and Derby [71], the relationship between a sample’s diameter and strength can be expressed by:

$$\frac{\tau}{\mu} = A \left(\frac{D}{|b|} \right)^m \quad \text{Eq. 3-9}$$

where τ is the critical shear stress, μ is the shear modulus, D is the sample's diameter, $|b|$ is the magnitude of the Burgers vector, and m is the size exponent.

Here the power law, *Eq. 3-9*, is applied to the experimental results. As shown in *Figure 3-13c*, the values of A for [101] and [111] oriented sample are 0.092 and 0.076, respectively. And the size exponent m for [101]- and [111]-oriented samples is -0.46 and -0.45, respectively. The values of m for both tested orientations are very close, implying that the size effect in the present study is not affected by the orientation. The values of m in the present study is lower than that of pure SC Al, which is ~ -1 [143] and -0.63 [135]. The lower value is obtained because the power law only considers the external contribution from the sample's size and does not consider the contribution from internal changes [147] (e.g., solute strengthening). Moreover, the bulk yield strength obtained from this power law is too low.

Here a simple power law was used to evaluate the bulk strength [148]:

$$\sigma_{size} = \sigma_{bulk} + A \cdot D^{-n} \quad \text{Eq. 3-10}$$

where σ_{size} is the yield strength of the micro sample, σ_{bulk} is the yield strength for the macro sample, A is a constant. The fitted curves are shown in *Figure 3-13d*, where both curves are presented with a high confidence interval, 99% for both orientations. The bulk yield strength obtained for [101]- and [111]-oriented sample is 147 ± 3 MPa and 177 ± 8 MPa, respectively. These values are slightly higher than those obtained from the experiment, which is 133 ± 3 MPa and 164 ± 7 MPa for [101] and [111], respectively. Higher values from the micron test have also been reported for CP-Ti [149] and pure Zr [148]. The discrepancy can possibly be minimized by compressing the pillar with larger ranges of diameters. But there was still good agreement between the theoretical and experimental results. Moreover, the size exponent obtained from this equation was -0.9, higher than that calculated from the Dou-Derby power law, but close to that from the pure Al [143].

Another concern/dispute relevant to the micron test results was the FIB machining, as the Ga ion beam could induce damage on the surface of the sample in the form of defects [150], such as dislocation loops and amorphous layer. Some researchers [136, 137, 151, 152] have argued that the flow strength could be enhanced by such a damaged layer, due to the pile-up of dislocations in these damaged areas. But this effect is only significant when the damaged depth reaches 100 nm or more [136]. Using a fine FIB milling current could reduce this damaged layer (only a few tens nanometres), and the mechanical response would not be influenced, as demonstrated in Ref. [153]. For the present study, as shown in *Figure 3-10c*, the Ga⁺ damaged layer is only 9.6 nm, which is considerably smaller than the 6.8 μm-diameter pillar used to evaluate the bulk's yield strength. Therefore, it is reasonable to assume that the influence of the Ga⁺ damage can be ignored for the flow stress of the pillar in this study.

3.5. Conclusions

In this chapter, micro-compression testing was performed on the pillars of the FZ in a hybrid laser-welded AA6061-T6 joint, with the diameter ranging from 400 nm to 6.7 μm. Based on the data obtained, the following conclusions are drawn:

- (1) Crystalline orientation had no size effect on the pillar of SC in the FZ, but had an influence on the yield strength, which could be explained by Schmid's factor; the orientation-dependent strength decreases with the increase in the pillar diameter, which could be explained by the strengthening of dislocation source.
- (2) The trend of "smaller is stronger" was observed for both orientations with the exponent m being ~ -0.45 when the pillar's diameter was below 3.3 μm; the exponent m would be -0.9 if the strength of the bulk considered.

- (3) The observed critical pillar diameter was 3.3 μm ; the size-dependent strength disappeared beyond this value, and the yield strength could be used as the bulk's strength if pillar's diameter was greater than this value.
- (4) The bulk yield stress could be obtained by fitting law of $\sigma_{size} = \sigma_{bulk} + A \cdot D^{-n}$, with n being -0.9.

Chapter 4 Microstructure versus size: nano/microscale deformation of FZ via pillar compression tests

4.1 Introduction

Uniaxial pillar compression has been the most popular testing methodology for detecting the plasticity of single metallic crystal at nano/microscales since 2004 [154]. Unlike the flow strength of the bulk, which is controlled by the Taylor hardening, such nano/microscale plastic deformation features with intermittent strain bursts and sample-size-dependent strength [72, 134, 155]. Since dislocation is the only carrier of plastic deformation at such scales, several dislocation-based models have been proposed to explain the observed phenomenon [70, 77, 156-159], among which the two best known are the dislocation-starvation model and the single-ended dislocation source model. At nanoscale, dislocations in the pillar have the greater likelihood to escape from the sample's free surface than to interact with each other, thus resulting in a dislocation-starvation state with high flow stress [70]. At microscale, a double-ended dislocation source (the Frank-Read source) in the pillar would become single-ended dislocation source due to the operation with the free surface, and the strength of the pillar is inverse to the maximum dislocation source ($\leq R$, radius of the pillar) [77]. A smaller pillar has shorter dislocation source, and thus the flow stress is higher.

Although extensive research has been conducted at nano/microscales, most works focus on the single crystals of pure metal, such as Ni [134, 154], Au [160, 161], Cu [137], and Al [162, 163]. However, in-service engineering materials are complex-microstructure alloys with solid solution, precipitates, and grain boundaries. Such internal obstacles, which can impede the dislocation motion under external loading, coupled with the size of the external sample, could alter the deformation behaviour of nano/microscale samples [135, 164-166]. But a good

understanding of the influence of the interplay between the internal microstructure and the size of the external sample on the strength is still lacking.

In this chapter, the microstructure of the pillar is modified with solute strengthening, which is a broadly used material-strengthening method in engineering materials (e.g., 5xxx aluminium alloys, FZ of welded Al alloys), and the dislocation density is modified by pre-deformation of the pillar. Different from the emphasis in Chapter 3, which only studied the nano/microscale plasticity in ER5 joints, the main aim of this chapter is to quantitatively study the effects of solute elements, dislocation density and size on the strength of SCs in the FZ and provide the microplasticity information to the strength prediction of ER4 joints which will be used in Chapter 5.

4.2 Experimental and simulation methods

4.2.1 Experimental methods

The materials used in this study are the FZ of hybrid laser-welded AA6061 with two filling materials (ER5356 and ER4043). More detail of the welding conditions can be found in Chapter 2. The FZ was chosen as the studied material for two reasons: (1) the filling materials could produce different solute solutions and dislocation densities in the FZ, so that the effect of solutes and dislocation density on the mechanical properties of the nano/micropillar could be studied; (2) the plasticity of the nano/microscale pillar could be used to predict the macroscale properties. Two blocks were taken out from the FZ of hybrid laser-welded AA6061-T6 alloy joints with two fillings, ER5356 and ER4043. For simplicity, the welded joints with fillings ER5356 and ER4043 are denoted as the ER5 joint and ER4 joints, respectively. The two blocks were mounted by resins, then ground and polished by standard metallurgical procedure to obtain a mirror-like surface. The last step was finishing by a gentle polish with 0.02 μm colloidal silica solution to get rid of any strained layers that

had been produced in the previous polishing steps. The two well-polished samples were then subjected to electron back scatter diffraction (EBSD) tests to obtain the information about crystal orientations and grain sizes. According to the EBSD results, as shown in *Figure 4-1*, four orientations ($[10\bar{1}]$, $[111]$, $[31\bar{2}]$, and $[\bar{5}\bar{3}2]$) were selected for the FZ in the ER4 joint, and two orientations ($[101]$ and $[111]$) were selected for the FZ in the ER5 joint. The summary of crystallographic data for selected grains can be found in *Table 4-1*.

Pillars with diameter ranging from 400 nm to 6.8 μm were machined using FIB by FEI Helios 600 Nanolab. The coarsening milling was done with currents of 9 nA down to 0.21 nA at 30 kV, and finally finished with 45 pA at 30 kV to reduce FIB damage. The pillar's height-to-diameter ratio was kept between 3:1 to 4:1 to guarantee that the pillar was free of substrate constraints and not buckled during compression. For simplicity, the pillars from the FZ of the ER4 joint and ER5 joints are denoted as the ER4 and ER5 pillars, respectively.

The machined pillars were compressed by a nanoindenter (TriboIndenter TI900, Hysitron) with a flat-end tip (9 μm diameter). Since there are always random drifts between the optic microscope and the tip, it was difficult to accurately locate the pillar via the microscope only. If the pillar was not well allocated, it would be bent instead of being compressed. In the experiment, an in-situ imaging method was used with the tip to find the pillar, followed by disengaging the tip for about 40 mins to reduce the thermal drift below 0.05 nm/s. All tests were done under displacement-control mode with the applied strain rate being around $1 \times 10^{-3} \text{ s}^{-1}$. The strain was calculated with the displacement divided by the initial height of the pillar, and the stress was obtained with the load divided by the initial cross-section area of the pillar. The stress value at the first strain burst was considered the yield stress of the pillar. A scanning electron microscope was used to observe the pillar before and after the compression to obtain the dimensions and deformed morphology of the pillar.

After deformation, some pillars were FIB machined to thin sheets (with the thickness below 100 nm), and then lifted to a TEM grid for TEM observation. The TEM experiment was conducted using a JEOL 2100F microscope at the acceleration voltage of 200 kV.

Table 4-1 Summary of crystallographic data of the selected grains.

	Single crystal	Euler angle	Schmid factor	Dislocation density/ m ⁻²
ER4 pillars	[10 $\bar{1}$]-oriented	253.6, 40.7, 19.9	0.45	1.32×10 ¹³
	[111]-oriented	273.3, 343.3, 39.4	0.3	
	[31 $\bar{2}$]-oriented	268.5, 32.9, 73.1	0.45	
	[$\bar{5}$ 3 $\bar{2}$]-oriented	124.4, 24.8, 23.6	0.46	
ER5 pillars	[101]-oriented	268.1, 44.1, 89.9	0.44	9.19×10 ¹²
	[111]-oriented	123.2, 44.2, 2.7	0.32	

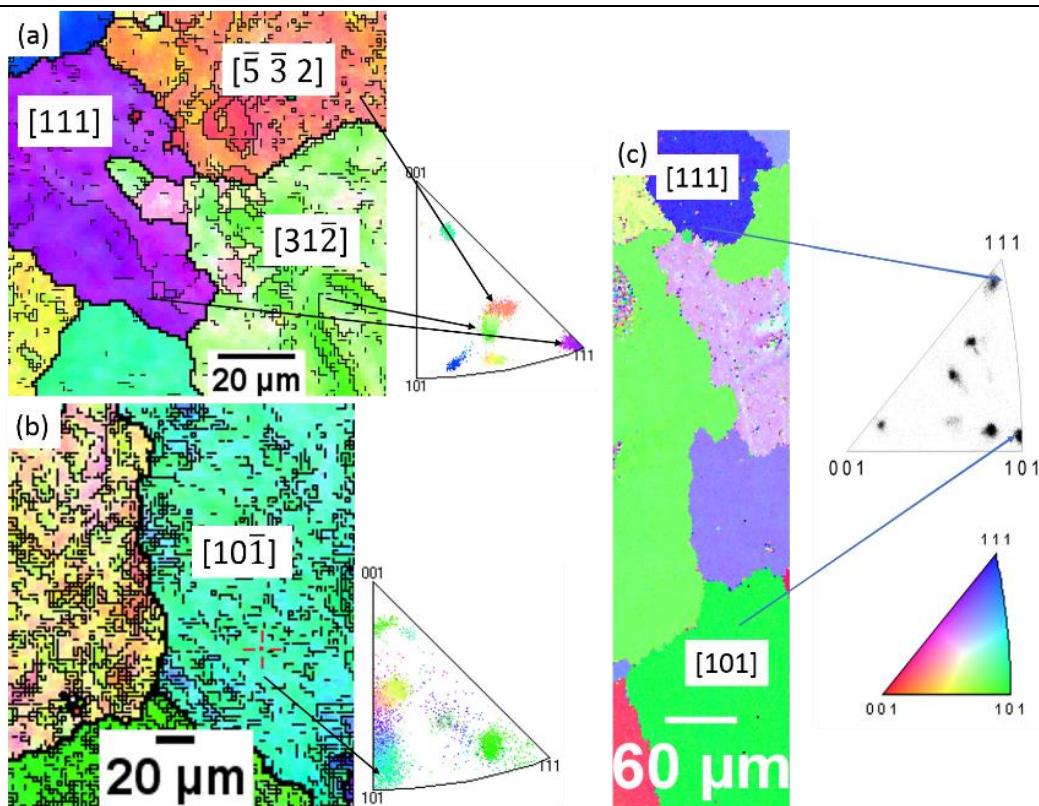


Figure 4-1 (a) (b) Selected orientations for pillar machining in the FZ of the ER4 joint, (c) selected orientations for the pillar machining in the FZ of the ER5 joint.

4.2.3 Simulation methods

To understand the influence of crystalline orientation and dislocation density on the mechanical behaviour of the pillar at atomistic level, MD simulation was done using LAMMPS [128] with the potential developed by Jelinek et al. [167]. The model for the compression in MD simulation is shown in *Figure 4-2*. The nanopillar was 28 nm height with a 10 nm diameter. Mg and Si atoms were randomly distributed in the pillar with the concentration of 0.34% and 0.46% (atomistic weight), respectively, which was the same as the results from EDS tests.

Before compression, the nanopillar was first relaxed by energy minimization (conjugate gradient method), then equilibrated by MD in an isobaric-isothermal (NPT) ensemble at a pressure of 0 bar and a temperature of 300 K for 100 ps. A constant strain rate of $1 \times 10^9 \text{ s}^{-1}$ was applied along the z axis to the total strain of 7.5% at the temperature of 300 K under NPT conditions. Then the system was unloaded and equilibrated for 100 ps at 300K. The goal of this step was to achieve an initial dislocation of about 10^{16} m^{-2} and 10^{17} m^{-2} for [110]- and [111]-oriented pillar, respectively.

Periodic boundary conditions were applied for all three directions. The timestep for the simulation was 1 fs. The results were visualized using Ovito software [130]. Common neighbour analysis (CNA) [131] techniques were used to identify the defective structure and its evolution during the simulations. The dislocation extraction algorithm (DXA) [132] was used to summarize and analyse dislocation behaviour during the compression.

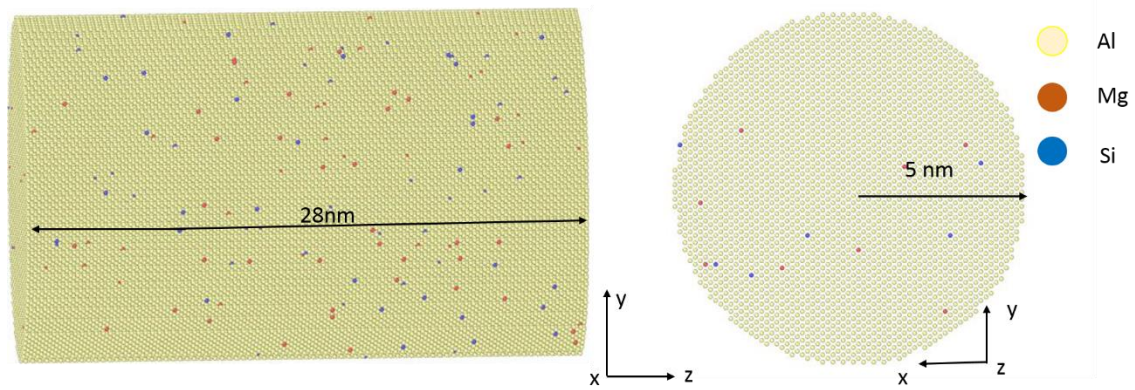


Figure 4-2 Model for molecular dynamic simulation for Al-Mg-Si alloys.

4.3 Results

4.3.1 Micropillar compression for the pillars without pre-deformation

The morphology of the deformed ER4 pillars is shown in *Figure 4-3*. Pillars with three orientations are shown with one slip offset, whereas there are two slip offsets for the $[10\bar{1}]$ -oriented pillars. The slip offset is not affected by the sample diameter. For the $[101]$ -oriented ER5 pillars (as seen in *Figure 3-8a-b*), there are also two slip offsets which are not influenced by the pillar's diameter. However, as seen in *Figure 3-8c-d*, the surface in the $[111]$ -oriented ER5 pillar changes from no obvious slip offset to one slip offset with the increase in the pillar diameter.

Representative stress-strain curves for the ER4 pillars is shown in *Figure 4-4a-b*. Similar to the single crystal of FCC pure metal, the stress-strain curves for the orientations of $[10-1]$ and $[111]$ are characterized by strain bursts. The stress-strain curves for pillars taken from the ER5 joint were illustrated in Chapter 3. The yield stress for the pillars from the FZ of the ER4 joint does not change much with an increase in the pillar diameter, as demonstrated in *Figure 4-4c*, which is different from the results from the FZ of ER5 joints presenting the trend of “smaller is stronger” (see *Figure 3-9c*), meaning that pillars with smaller diameter have stronger strength. In the bulk samples, the strength would be influenced by the orientation, an effect which is known as Schmid's law. As suggested in *Figure 4-4c*, the influence of crystal

orientation on the yield strength is much greater in the pillars taken from the FZ of the ER4 joint than that of the pillars taken from the FZ of the ER5 joint (see *Figure 3-9c*). In contrast, ER4 pillars with various orientations show almost the same strength at the same diameters, suggesting that Schmid's law does not work for ER4 pillars.

The size effect on strength is normally expressed by the power law [71]:

$$\frac{\tau}{\mu} = A \left(\frac{D}{|b|} \right)^m \quad \text{Eq. 4-1}$$

where τ is the critical shear stress, μ is the shear modulus, D is the sample diameter, $|b|$ is the magnitude of the Burgers vector, and m is the size exponent. The power law was applied here, and the curves obtained are shown in *Figure 4-4d*, which displays that the exponent for the size effect is very small (-0.016~-0.087), indicating that there is no size effect on the strength of the ER4 pillars at nano/microscales. It can also be seen from *Figure 4-4d* that the size effect is not affected by the crystal orientation.

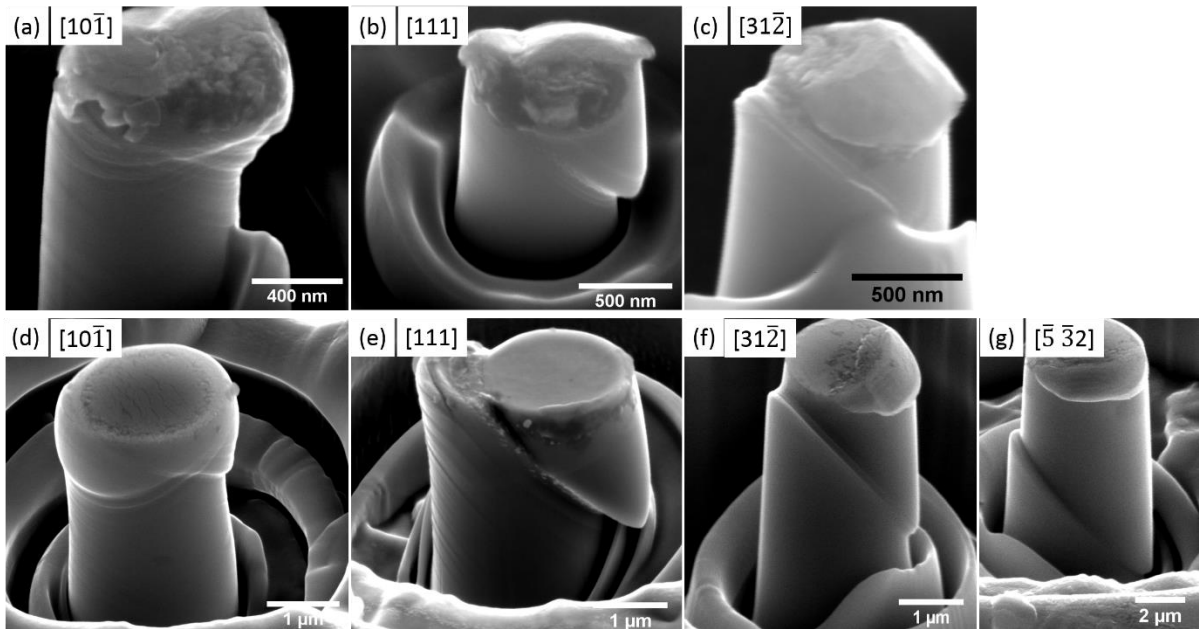


Figure 4-3. Morphology of deformed pillars taken from the FZ of ER4 joint, (a)-(c) are 800 nm-diameter pillars with orientations of $[10\bar{1}]$, $[111]$, and $[31\bar{2}]$; (d)-(g) are 2000 nm-diameter pillars with orientations of $[10\bar{1}]$, $[111]$, $[31\bar{2}]$, and $[\bar{5} \ 3\bar{2}]$.

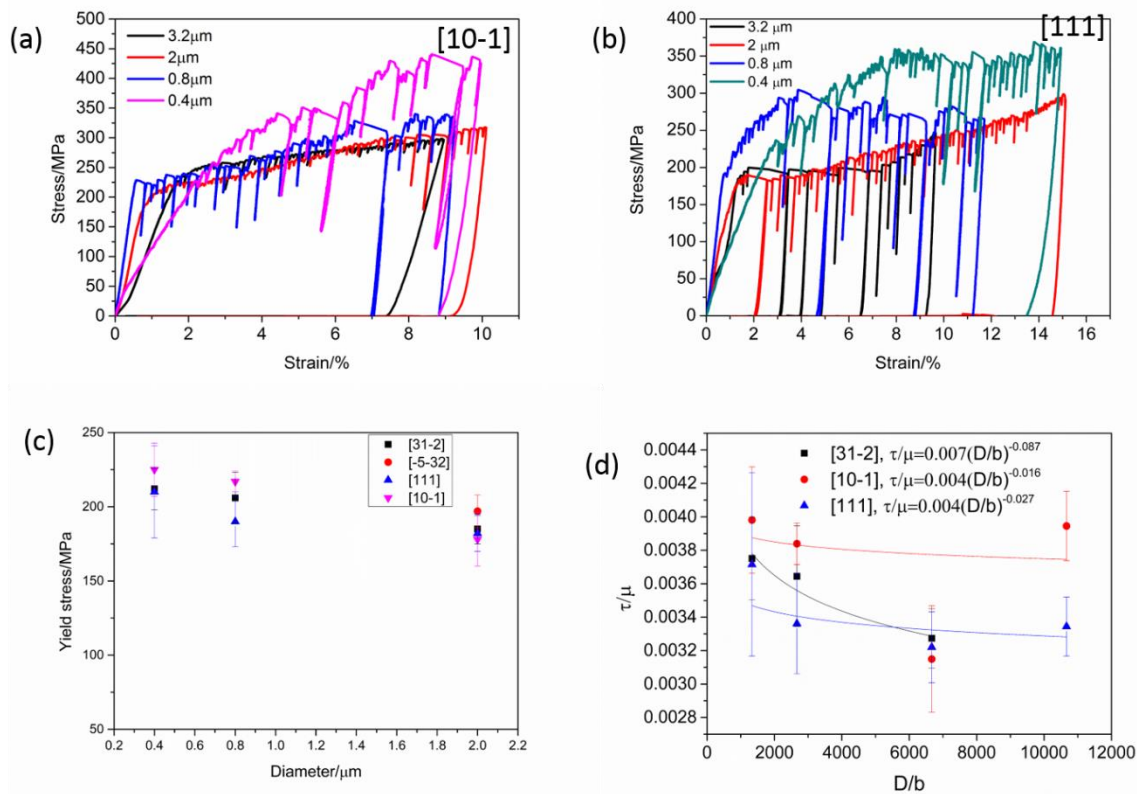


Figure 4-4 (a) Representative stress-strain curves for $[10\bar{1}]$ -oriented pillars taken from the FZ of ER4 joint, (b) Representative stress-strain curves for $[111]$ -oriented pillars taken from the FZ of ER4 joint; (c) Yield stress vs. diameter for pillars taken from the FZ of ER4 and ER5 joint, respectively; (d) Normalized strength vs. normalized diameter for pillars taken from FZ of ER4 joint, respectively.

4.3.2 Dislocation behaviour

Figure 4-5 shows the TEM results for the $[111]$ -oriented 800nm-diameter ER4 pillar. The slip offset can be seen in Figure 4-5a, and the dislocation density near the free surface seems not to change much compared to the inner area (Figure 4-5b). The enlarged view (Figure 4-5c) for the place indicated in Figure 4-5b shows dislocations entangling with each other. For the place near the top of the pillar (Figure 4-5d), high dislocation density can be seen in the form of dislocation circles and entanglement.

TEM results for the $[10\bar{1}]$ -oriented ER4 pillars are illustrated in Figure 4-6. Independent of the pillar's diameter, the dislocation density near the slip offset is lower than the internally, as

suggested by *Figure 4-6a* and *c*. This is possibly due to more slip events occurring during the compression and the dislocations escaping from the free surface. For the 2 μm -diameter sample (*Figure 4-6d*), the density and structure of the dislocation are higher and more complex than those of the 800nm-diameter sample (*Figure 4-6b*). Compared to the ER4 pillars, the ER5 pillars show a less complex dislocation structure, as demonstrated in *Figure 3-10* and *Figure 3-11*. The dislocation density for the tested pillars was calculated using the method described by Jennings et al. [138], and the results are shown in *Figure 4-7*. At the same diameter, the dislocation density in the ER4 pillars after deformation is about two orders higher than that of the ER5 pillars. For the orientation effect, pillars with [111] orientation have higher dislocation density than that of the $\langle 110 \rangle$ -oriented pillar. With the same microstructure, the density of dislocation is higher for the larger sample than that of the smaller sample, as demonstrated in *Figure 4-7a* for ER4 pillars.

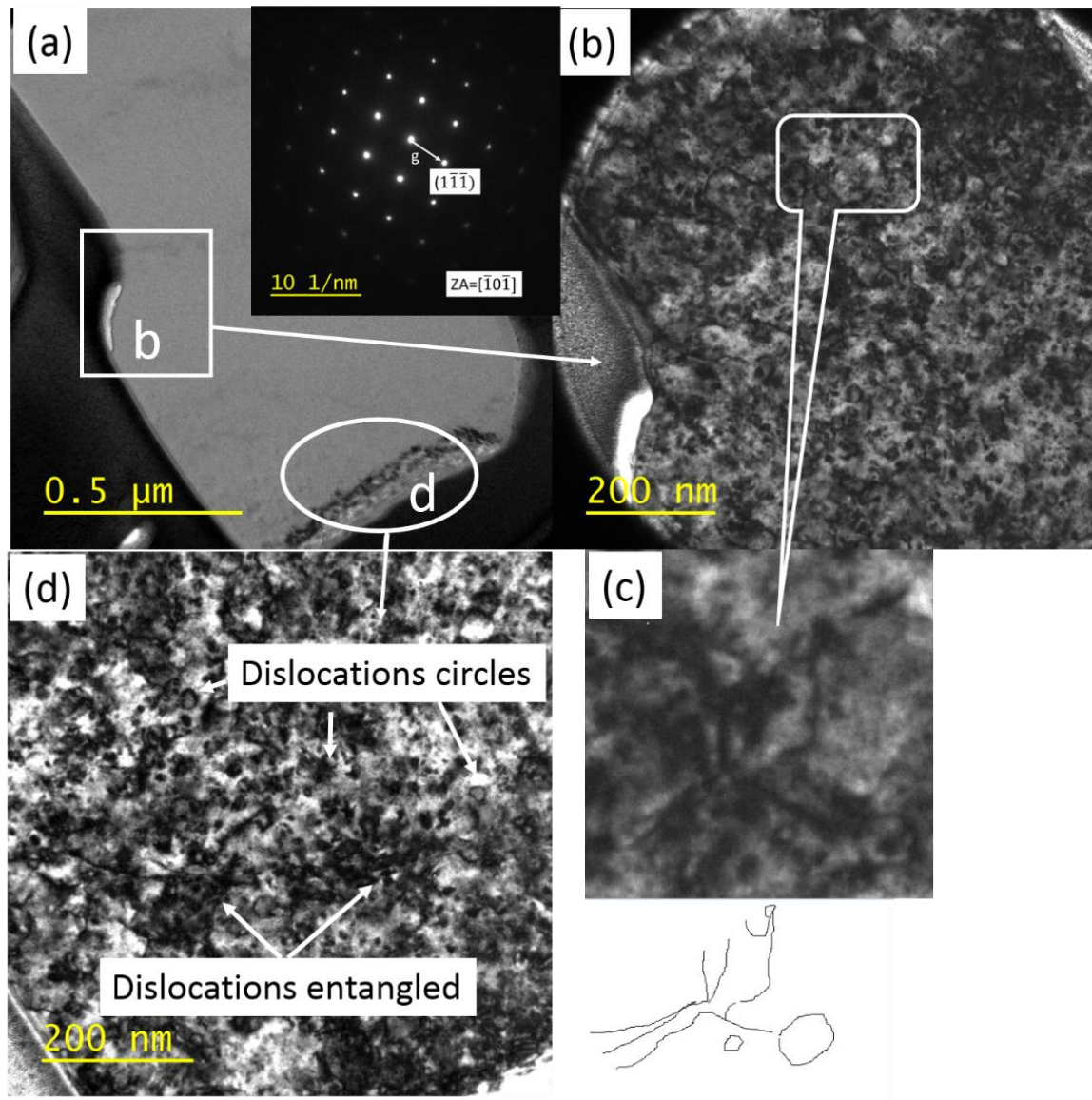


Figure 4-5. TEM results for the $[111]$ -orientated 800 nm-diameter pillars taken from the FZ of the ER4 joint, (a) overview of the deformed pillar, (b) dislocation structure near the slip offset as indicated in (a) with a square, (c) enlarged view of the site indicated in (b), (d) dislocation structure near the top of the pillar.

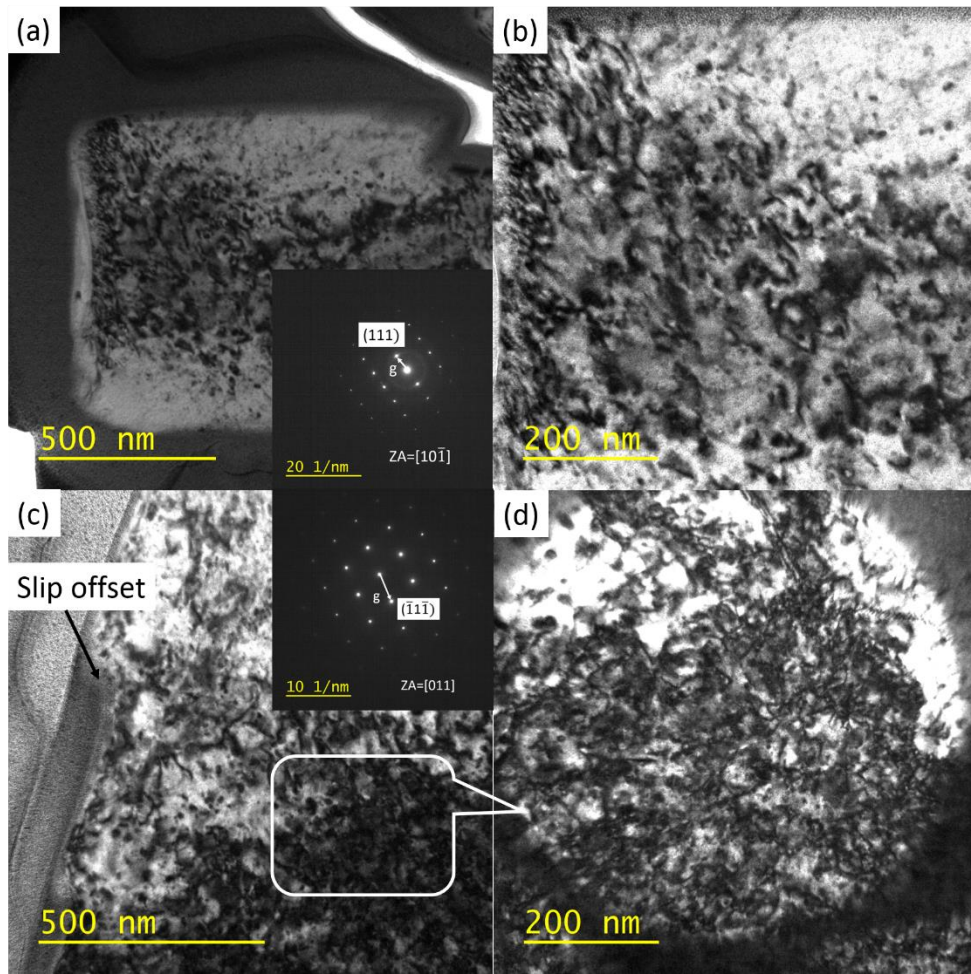


Figure 4-6. TEM results for $[10\bar{1}]$ -oriented pillars taken from the FZ of the ER4 joint, (a) overview for the 800 nm-diameter pillar, (b) dislocation structure near the top of the 800 nm-diameter pillar, (c) dislocation structure near the slip offset for the 2000 nm-diameter pillar, (d) enlarged view of the dislocation structure of the site indicated in (c).

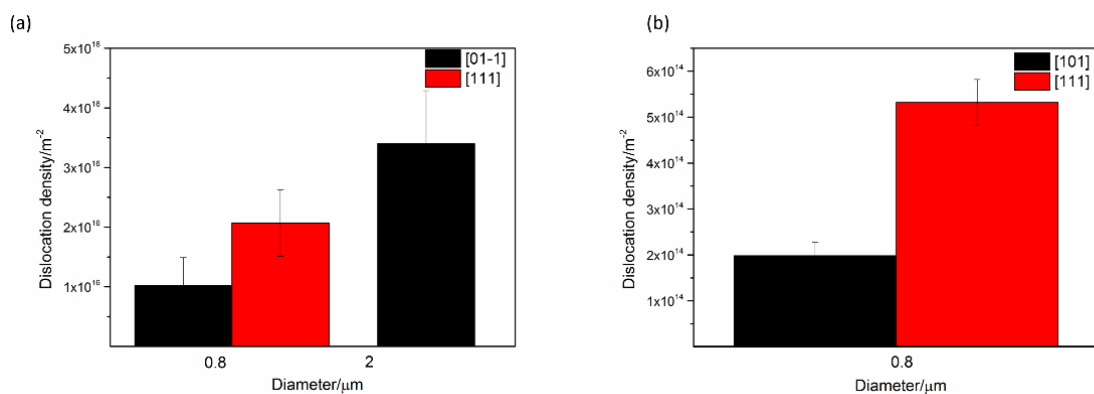


Figure 4-7. (a) Dislocation density for pillars of the FZ taken from the ER4 joint, (b) dislocation density for pillars of the FZ taken from the ER5 joint.

4.3.3 Micropillar compression for pillars with pre-deformation

To understand the effect of dislocation density on the deformation behaviour of the FZ at nano/microscales, some larger deformed pillars (*Figure 4-8a and d*) with orientation $\langle 110 \rangle$ were remade into smaller pillars using FIB. By the remade process by FIB, the surface slip steps were removed with smooth lateral surface, see *Figure 4-8*. The information about the original and pre-deformed pillars, such as the diameter, pre-stains and dislocation density, is shown in *Table 4-2*.

As seen in *Figure 4-8b and e*, the previously-deformed pillar has the same shape as the non-deformed ones. After compression (*Figure 4-8c*), the ER5 pillar still shows two slip offsets that are not influenced by the pillar's diameter, which is similar to that of the nondeformed pillars. The previously-deformed ER4 pillar (*Figure 4-8f*) shows only one slip offset.

The stress-strain curves for the previously deformed pillar are shown in *Figure 4-9*. Although the dislocation density is much higher, the stress-strain curves for the pillars still feature with strain burst, as illustrated in *Figure 4-9a and d*. However, there is almost no size effect on the strength of both pillar types. As demonstrated in *Figure 4-9b*, the exponent of size effect for the ER5 pillars is reduced to -0.057, which is much smaller than that of the non-deformed pillars (see *Figure 3-13c*). Also, the influence of crystal orientation on the strength of SCs is largely reduced for the ER5 pillars with previous-deformation (compare *Figure 4-9c and Figure 3-13d*). One common finding for the pillars of both joints is that the yield strength is greater in the previously-deformed pillars.

Table 4-2 Information of pre-deformed pillars machined from original larger pillars

	Diameter of original pillars/ μm	Deformed to strain/%	Diameter of remade pillars/ μm	Residual Dislocation density (m^{-2})
ER5 pillars	5.2	7	3	$> 1.98 \pm 0.8 \times 10^{14}$
	3.3	7.2	2	
	2	6.8	0.8	
ER4 pillars	3.2	9	2	$\geq 3.4 \pm 0.9 \times 10^{14}$
	2	9.4	0.8	

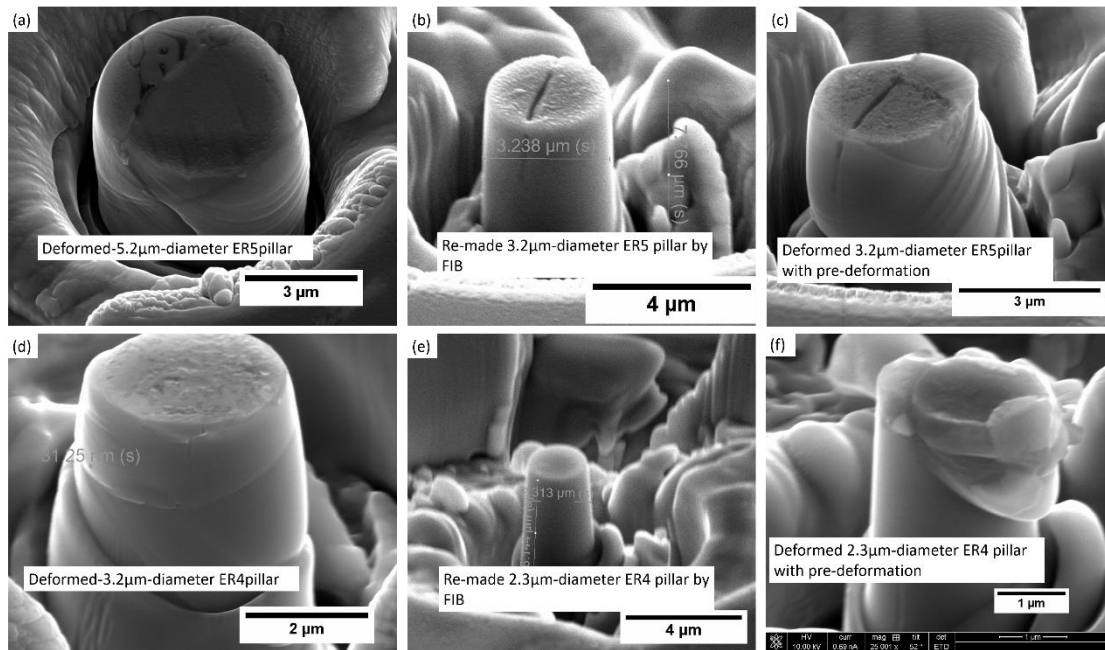


Figure 4-8. Procedure for making pillars from deformed larger pillars, (a) deformed 5.2 μm -diameter ER5 pillar, (b) 3.2 μm -diameter pillar made from deformed 5.2 μm -diameter ER5 pillar, (c) deformed morphology of the pre-deformed 3.2 μm -diameter pillar; (d) deformed 3.2 μm -diameter ER4 pillar, (e) 2.3 μm -diameter pillar made from deformed 3.2 μm -diameter ER4 pillar, (f) deformed morphology of the pre-deformed 2.3 μm -diameter pillar.

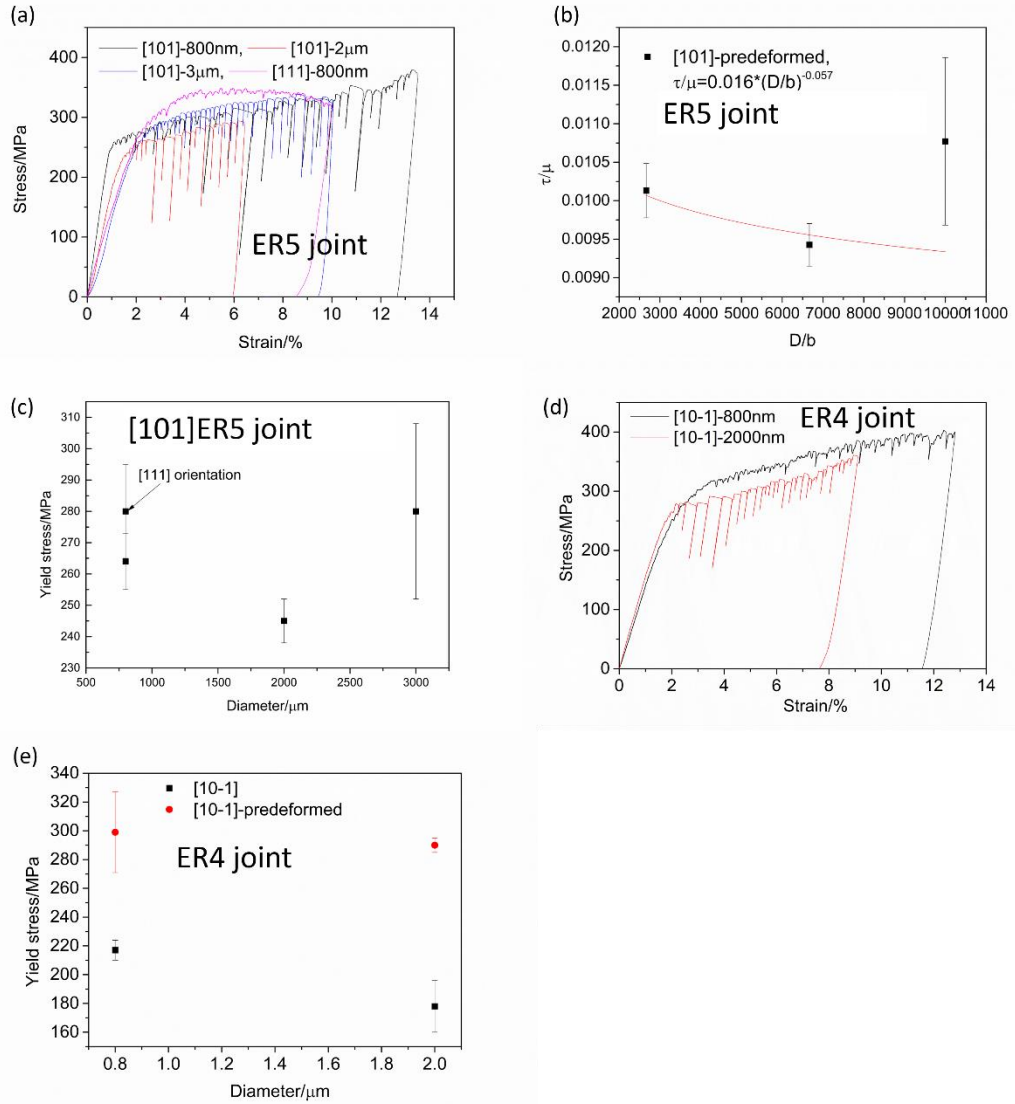


Figure 4-9. (a) Representative stress-strain curves for previously deformed pillars taken from the FZ of the ER5 joint, (b) Normalized strength vs. normalized diameter for pre-deformed pillars taken from the FZ of the ER5 joint, (c) yield stress vs. diameter for pre-deformed pillars taken from the FZ of the ER5 joint; (d) representative stress-strain curves for pre-deformed pillars taken from the FZ of the ER4 joint, (e) yield stress vs. diameter for pre-deformed pillars taken from the FZ of the ER4 joint.

4.3.4 MD simulation results

As seen in *Figure 4-4c* and *Figure 4-9c*, the strength of both the ER4 pillar and the pre-strained ER5 pillar is not influenced by the crystalline orientation, a finding which is contrary to Schmid's law. Since the ER4 pillar and pre-strained ER5 pillar had higher dislocation density, it was proposed that the dislocation density was responsible for the unusual results.

To support this view, MD simulation was conducted. As shown in *Figure 4-10a*, when there is no dislocation, the [111]-oriented Al-Mg-Si pillar has higher stress than that of the [110]-oriented pillar, which can be explained by Schmid's law, as the [111] orientation has lower Schmid's factor. However, there are almost no differences in the flow stress for both orientations if higher dislocation density is included in the sample, as demonstrated in *Figure 4-10b*. The dislocation density evolution, *Figure 4-10c*, shows that the dislocation density in [111]-oriented sample is higher than that of the [101]-oriented sample, a finding which is consistent with the TEM results (*Figure 4-7*). The microstructure development for both orientations is shown in *Figure 4-11* and *Figure 4-12*. For both orientations, most of the dislocations are partial ones.

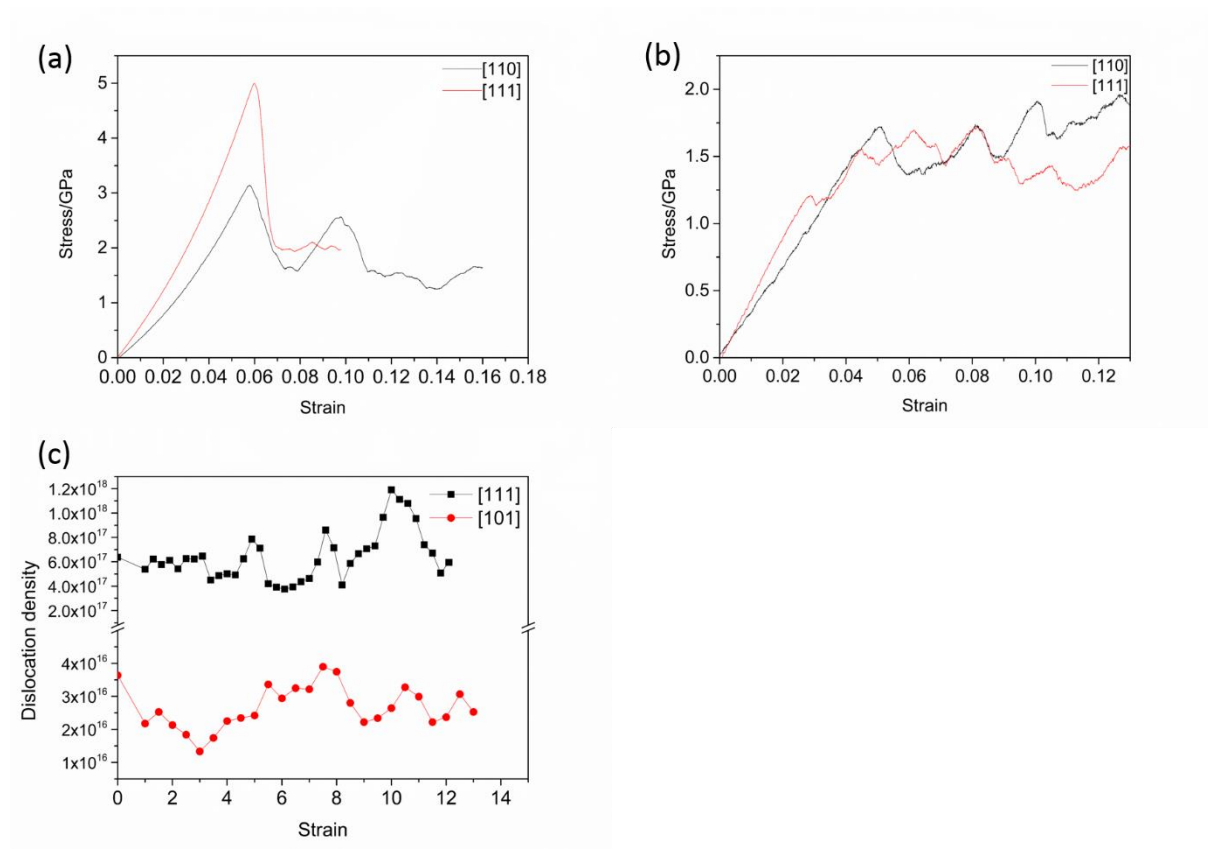


Figure 4-10. (a) Stress-strain curves from MD simulation for samples without initial dislocation density, (b) stress-strain curves from MD simulation for samples with initial dislocation density, (c) dislocation density evolution during compression.

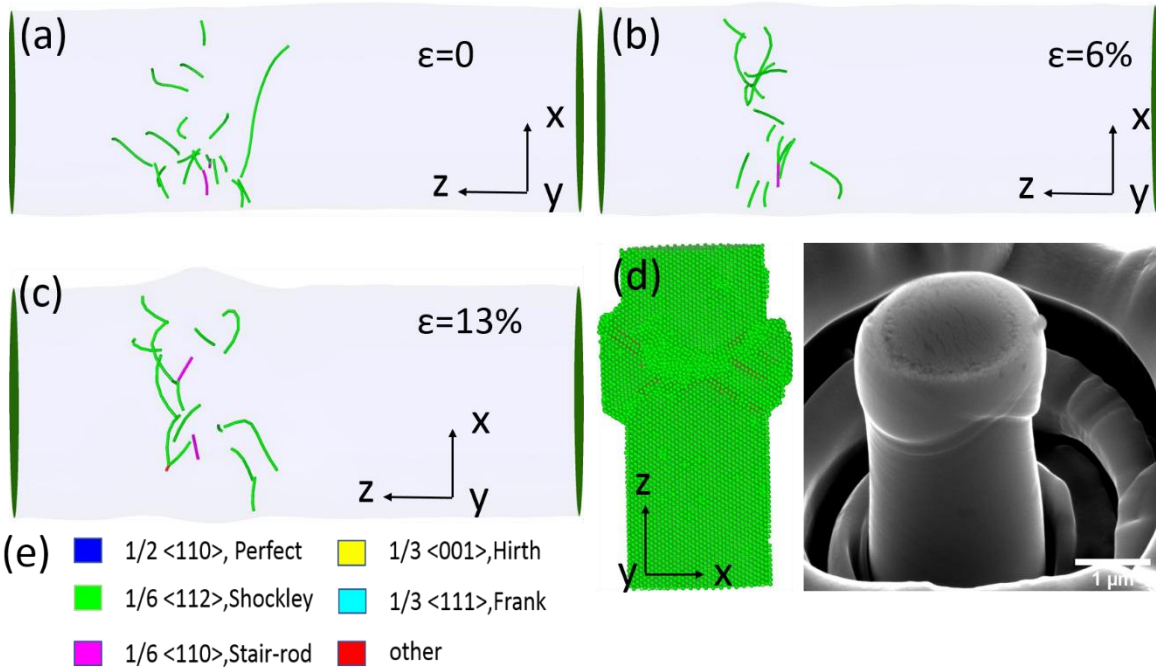


Figure 4-11. (a)-(c) Dislocation density evolution for $[110]$ -oriented sample under different strains, (d) deformed morphology from experiment and simulation, (e) indication for dislocation types.

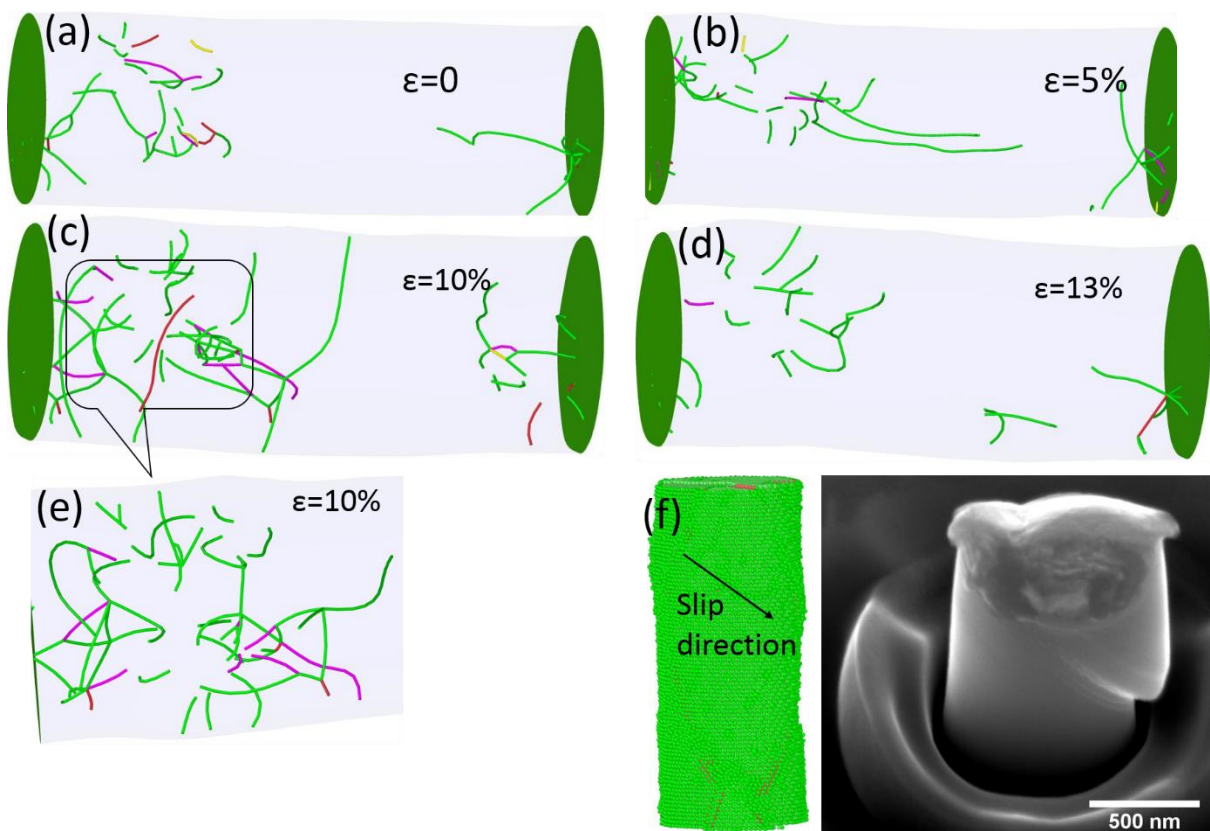


Figure 4-12. (a)-(e) Dislocation density evolution for $[111]$ -oriented sample under different strains, (f) deformed morphology from experiment and simulation.

4.4 Discussion

4.4.1 Effect of alloying on the size effect and strength

At nano/microscales, the effect of sample size on the strength is influenced by the sample's microstructure, as suggested by Girault et al., [73] who reported that the size-dependence of strength disappeared for the Ni-based superalloy MA6000 in which the particle size was about 20-30 nm. They concluded that the size-dependence mechanisms did not work for alloying metallic system since internal microstructural features dominated the deformation rather than the size of the external sample. For Al-based alloys (such as AA2025 [42], Al-Sc alloys [168]), as shown in *Figure 4-13a*, the space and size of the internal particle/cluster is much smaller than the pillar's size, nevertheless, the strength of the pillar is still size-dependent. It seems that the size-dependent strength is still effective if the particle is not strong enough [164]. For the Al-based alloys, the exponent m is between -0.34 and -0.51, as suggested in *Figure 4-13a*. Our results for the pillar taken from the ER5356 joint are consistent with the findings of the research. The lower size effect is due to lower dislocation mobility caused by the lattice friction or the dragging effect from these solutes or precipitates. Basically, the material with higher crystal resistance against the dislocation motion exhibits a lower size effect [75].

One of the points of interest in studying the mechanical properties at nano/microscales is to finding a way to make the material tougher, or to stabilize the plastic deformation without or reduced strain burst [165, 169]. *Figure 4-13b* summarizes up-to-date results of the yield stress for Al alloys with different diameters at nano/microscales. It can be seen from *Figure 4-13b* that the yield strength of a single crystal of Al alloys is typically in the range of 88 MPa to 400 MPa, regardless of the type of strengthening method (solute, precipitates or both) used. However, if the pillar includes a nanoscale strong particle [170] or grain boundary [171], the yield strength can increase to 1.5 GPa, as seen in the case of Al7075 and Al-Fe

alloys in *Figure 4-13b*. Moreover, the stress-strain curves for the samples with nano-size grains are much smoother than that of the single crystal of Al alloys [168-171]. This comparison suggests a new clue to obtaining higher-strength materials with stable plasticity.

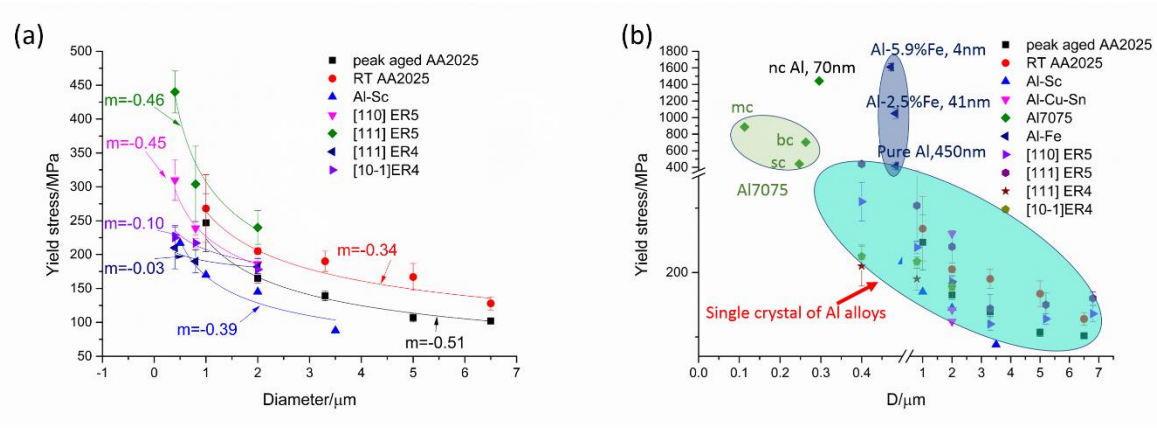


Figure 4-13. (a) Yield stress vs. diameter for the present study and Refs. [42, 168, 172], (b) effect of alloying and sample size on the yield stress of Al-based alloys (data from present study and Refs. [42, 168, 170-172]).

4.4.2 Effect of dislocation density

Surprisingly, the pillars of the FZ taken from the ER4 joint shows size-independent strength at nano/microscales, as demonstrated in *Figure 4-4c and d*. The size-independent strength may be caused by two factors: an internal alloying effect and dislocation density. An internal alloying effect such as nanosized strong particles can cause the domination of strength over the external pillar's size, as demonstrated in Refs. [73, 74]. However, the strength of ER4 pillars is lower than the counterpart of pillar of AA2025, as demonstrated by the strength of the 2 μm-diameter pillars in *Figure 4-13b*. This means that the microstructure in AA2025 is stronger than that in the ER4 joint in terms of impeding dislocation motion. But the size-dependent strength still functions for the single-crystal pillars in AA2025, so the internal alloying effect is thus not responsible, or not the main factor for the size-independent strength of the ER4 pillar.

The influence of dislocation density on the size effect has been reported previously for pure metallic single crystals. There are two main methods to increase the dislocation density, one by deforming the bulk to certain strains [161, 173, 174], the other by deforming the micro-sized pillar [175, 176]. These two methods lead to different results. Schneider et al. [173] examined the influence of pre-straining bulk Ni on the size effect at nano/microscales. They reported that previous deformation could inhibit the size effect and increase the yield stress of the pillar. They attributed the change in the size effect to the dislocation structure (e.g., dislocation cell wall, dislocation entanglements, high dislocation density) generated by the bulk pre-deformation, such that the dislocation movement could be effectively impeded by the already formed dislocation structure. Consequently, the size effect would be reduced. However, for smaller pillars with the diameter of a few hundred nanometres, the bulk pre-deformation could soften the yield stress of the pillar, as suggested in Ref. [161], because of the change of the deformation mechanism from dislocation starvation (for lower dislocation density) to Taylor hardening (for higher dislocation density). El-Awady et al. [174, 177] reported that the size exponent had a relation with initial dislocation density, $m \propto \rho^n$, with the higher-dislocation samples showing a lower size effect.

Contrary to the first method, the second method, in which the larger pillar is first compressed and then machined to a smaller one using FIB, has been reported to have no influence on the size effect. Schneider et al. [175] reported that the previous compression on a Mo pillar had a negligible effect on the stress-strain behaviour and the size effect. They proposed that the dislocation nucleation mechanism controlled the deformation behaviour of the Mo pillar. Gu et al [176] studied the effect of pre-straining and coating on the plastic deformation behaviour of Al micropillars. They found that pre-straining had almost no influence on the size effect but could change the yield stress of the pillar.

For the present case, the dislocation density of the fusion zone in the ER4 joint was 10^{13} m^{-2} , which was lower than that of the deformed pillars of pure metallic single crystal [176]. But because the dragging effect due to the solute strengthening was greater than that of the pure metal, more dislocations could remain in the pillar to sustain the plastic deformation. Consequently, the size effect was minimized. The results from the pre-strained pillars in the present study, as shown in *Figure 4-9*, are different from those in previous studies [175, 176]. For the pillar of ER5 joint, the previous straining causes the size effect to become negligible, as demonstrated in *Figure 4-9b*. After the deformation, the dislocation density of the 800 nm-diameter pillar reaches 10^{14} m^{-2} (*Figure 4-7b*), which is in the same order as that of the previously deformed Al pillar [176]. But the dragging effect of the solute disturbs the dislocation motion, leading to the storage of dislocations in the pillar. As a result, the size effect is reduced.

The other influence of the dislocation density is an increase in the strength of the pillar. As shown in *Figure 4-14* the yield strength of the pillar for both joints is increased. Since the contribution from the dislocation source strengthening is largely reduced, this effect is possibly due to the mutual dislocation interaction known as Taylor strengthening. Moreover, the increment due to the previous straining is larger in the bigger samples, as demonstrated by the 3.3 μm -diameter ER5 pillars (*Figure 4-14*). In the bigger pillars, the dislocation tends to be trapped in the pillar as it must travel a longer distance to escape from the free surface. Thus, the dislocation density is higher for larger pillars and the strength is greater.

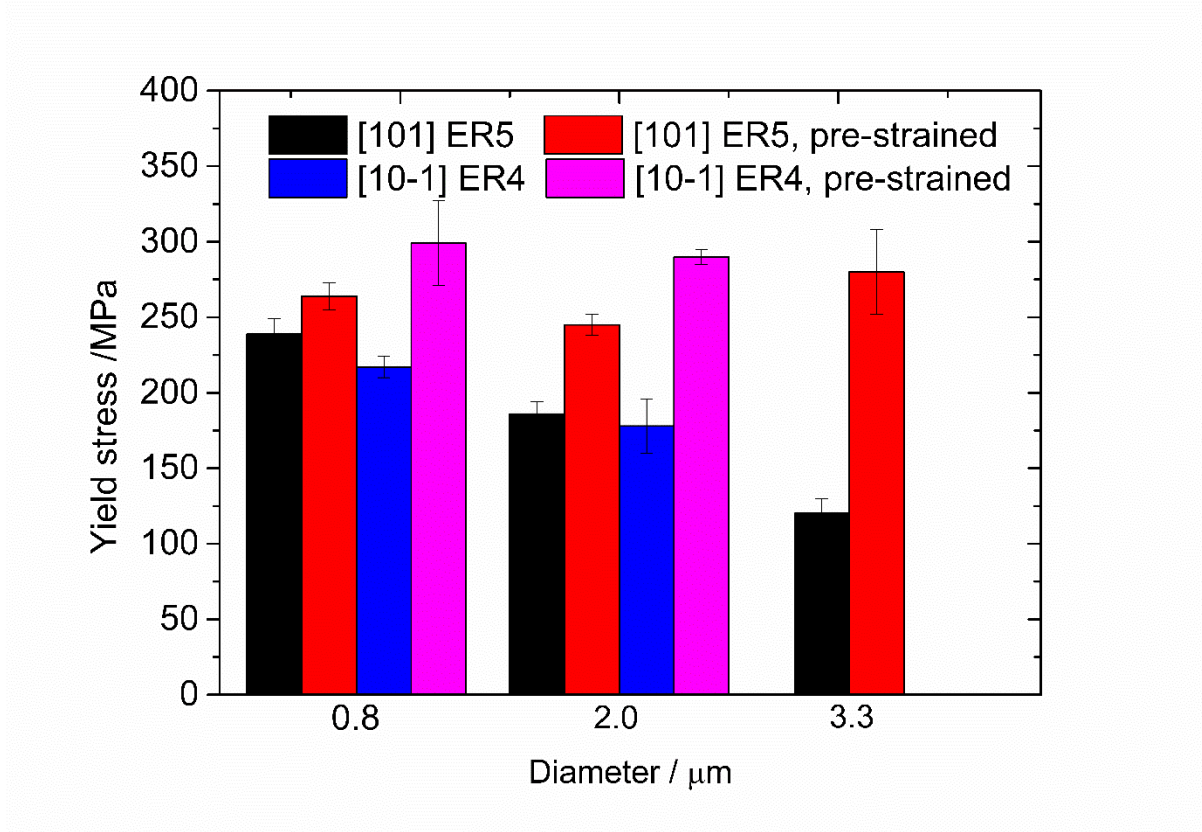


Figure 4-14 Yield stress for ER4 pillars and ER5 pillars with and without pre-deformation.

4.4.3 Possible mechanisms controlling the deformation

To quantify the effect of the alloying and dislocation density on the strength of Al alloys at microscale, a theoretical model is built, and the possible controlling mechanisms is discussed in this section.

The critical resolved shear stress (τ_{CRSS}) of Al alloys can be expressed by [178]:

$$\tau_{CRSS} = \tau_{athermal} + \tau_0 + \tau_{ss} \quad \text{Eq. 4-2}$$

where $\tau_{athermal}$ is the stress from athermal mechanisms associated with the long-range elastic dislocation interactions, τ_0 is the friction stress which is taken as 10 MPa [22], τ_{ss} is the stress from the strengthening mechanisms such as solid solution, which has been calculated in section 2.4.1. τ_{ss} for ER5 pillars and ER4 pillars is about 34 MPa and 54 MPa, respectively.

$\tau_{athermal}$ can be given as [179]:

$$\tau_{athermal} = \mu \frac{\beta}{D\sqrt{\rho}} + \alpha\mu b\sqrt{\rho} \quad \text{Eq. 4-3}$$

Where μ is the shear modulus, D is the diameter of the pillar, b is the magnitude of the Burger's vector, ρ is the dislocation density, β and α are constants which are determined by materials [179]. By fitting the experimental data, the constant β for ER5 and ER4 pillars is 0.003 and 0.004, respectively. the constant α for ER5 and ER4 pillars is 0.51 and 0.09, respectively. The first term on the right hand of *Eq. 4-3* presents dislocation source strengthening whereas the second term means dislocation forest interactions.

Using *Eq. 4-2*, the τ_{CRSS} for the pillars with different D and ρ is shown in *Figure 4-15*. Clearly, there is good agreement between the experimental and calculated results for the tested pillars. For the tested pillars, the dislocation-source strengthening decreases with increasing the size and dislocation density of pillars, as demonstrated in *Figure 4-15*. It seems that the dislocation density has more influence on decreasing the dislocation-source strengthening (see the curves of dislocation-source strengthening in pre-deformed pillars in *Figure 4-15*). For 0.8 μm -diameter ER5 pillars (see *Figure 4-15a*), the strengthening contribution from dislocation source and solid solution is nearly at the same level, and the strengthening from dislocation interaction is small (12 MPa). However, the contribution from dislocation interaction in pre-deformed ER5 pillars reaches up to 69 MPa, while the dislocation-source strengthening is lower than 10 MPa. This change suggests that the deformation mechanism for the pre-deformed ER5 pillars is dominantly dislocation interaction.

For ER4 pillars, the highest dislocation-source strengthening is 1.8 times smaller than the solid solution strengthening, suggesting that the pillar's strength may be dominantly

controlled by the solid solution strengthening. For the pre-deformed ER4 pillars, the dislocation-source strengthening is almost reduced to 0 MPa due to the high dislocation density. Nevertheless, the strengthening from dislocation interactions is increased up to 77 MPa in 2 μ m-diameter pillars. Considering that the solid-solution strengthening is 54 MPa, it is reasonable to deduct that both Taylor hardening and solid-solution strengthening are the controlling mechanism.

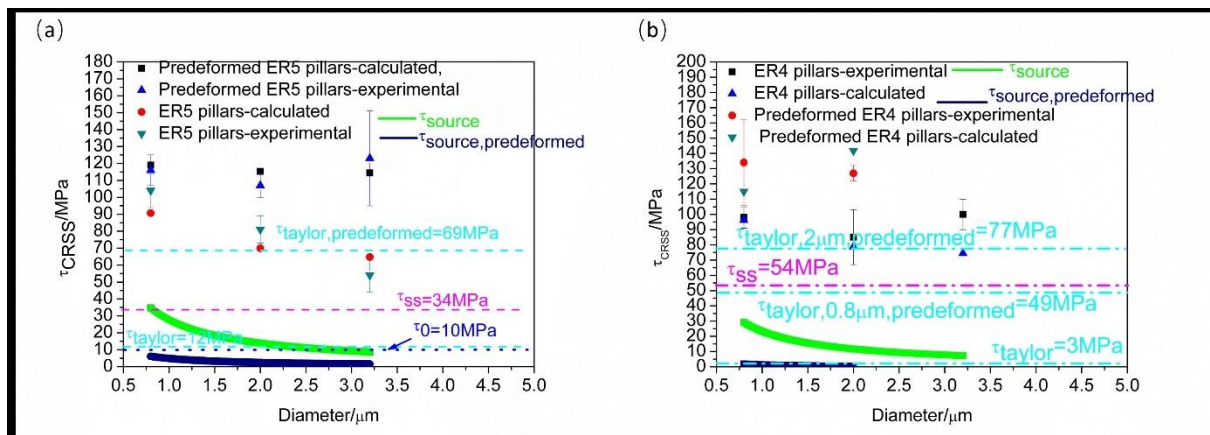


Figure 4-15. (a) Diameter vs. τ_{CRSS} from experimental results and theoretical model for ER5 and pre-deformed ER5 pillars, (b) Diameter vs. τ_{CRSS} from experimental results and theoretical model for ER4 and pre-deformed ER4 pillars. The contribution to the strength from τ_{source} , τ_{ss} , and τ_{taylor} is illustrated by green, magenta and cyan dashed lines, respectively. For the pre-deformed pillars, the contribution to the strength from τ_{source} is illustrated by navy lines.

4.5 Conclusions

Based on the foregoing results, the following summaries can be given:

- (a) Different from ER5 pillars, the yield strength of ER4 pillars is size- and orientation-independent.

- (b) With the orientation unchanged, the dislocation density in the deformed ER4 pillar is higher than that of the ER5 pillar. The pillar with greater diameter has the higher density of dislocation.
- (c) With the increase in the dislocation density, the size and orientation effect on the strength disappears for both ER4 and ER5 pillars.
- (d) A theoretical model is successfully constructed and used to qualify the effect of solute elements, size, and orientation on the strength of SCs in the FZ; the mechanism behind the deformation is also presented via this model.

Chapter 5 Bridging the gap between microscale and macroscale deformation of the hybrid laser-welded Al alloy joints: experiment and simulation

5.1 Introduction

In Chapters 3 and 4, the microplasticity of the FZ at microscale was studied, with the ER5 pillars presenting as size-dependent while the ER4 pillar showed as size-independent. In this chapter, size-independent microplasticity is used to predict the stress-strain behaviour of the welded joint at macroscale via CPFEE simulation. For the first time, how to link the microplasticity with macro plasticity in welded joints is shown in this chapter.

5.2 Methodology

The base metal used in this study was AA6061-T6, which is utilized in high-speed train bodies (see *Figure 5-1a*). The chemical composition of the base metal can be found in Ref. [22]. Hybrid laser welding was used to join AA6061-T6 (see *Figure 5-1b*) with two filling materials, ER5356 and ER4043. The cross-section of the FZ was characterized by EBSD testing (*Figure 5-1c*), for which the testing parameters can be found in Ref. [22]. A single crystal with orientations of $\langle 110 \rangle$ and $\langle 111 \rangle$ was selected to make a cylindrical pillar at microscales machined by FIB, see *Figure 5-1d*. The well-prepared pillar had a height-to-diameter ratio of $\sim 3:1$. The pillar was then compressed by a flat-end tip in a nanoindentation machine. The pillar compression test was in displacement-control mode with the constant strain rate of $\sim 1 \times 10^{-3} \text{ s}^{-1}$. The stress was obtained by dividing the force by the original area of the sample, and the strain was obtained by dividing the displacement with the original height. The deformed pillar was observed with SEM and TEM to obtain the deformation mechanism (dislocation), *Figure 5-1e*. The macroscale deformation was performed with tensile and compressive testing (*Figure 5-1f*). Based on the data of micropillar deformation,

CPFE was first used to predict the SC mechanical properties, and then to predict the polycrystal samples (*Figure 5-1*).

The theory for phenomenological constitutive models is introduced here. The deformation gradient \mathbf{F} is given as:

$$\mathbf{F} = \mathbf{F}_e \mathbf{F}_p \quad \text{Eq. 5-1}$$

where \mathbf{F}_e represents the crystal lattice rotation and elastic stretching and \mathbf{F}_p denotes the plastic part of the deformation gradient. Given that the slip is the only deformation process, the plastic deformation ($\dot{\mathbf{F}}$) can be expressed by:

$$\dot{\mathbf{F}} = \mathbf{L}_p \mathbf{F}_p \quad \text{Eq. 5-2}$$

\mathbf{L}_p is given as:

$$\mathbf{L}_p = \sum_{\alpha=1}^n \dot{\gamma}^\alpha \mathbf{m}^\alpha \otimes \mathbf{n}^\alpha \quad \text{Eq. 5-3}$$

where $\dot{\gamma}^\alpha$ is the slip rate on the slip system α , \mathbf{m}^α and \mathbf{n}^α are unit vectors of the slip direction and normal to the slip plane of the slip system α , respectively; n is the number of slip systems, which is 12 for FCC metal. The slip rate $\dot{\gamma}^\alpha$ can be described as:

$$\dot{\gamma}^\alpha = \dot{\gamma}_0 \left| \frac{\tau^\alpha}{g_c^\alpha} \right|^{\frac{1}{m}} \text{sgn}(\tau^\alpha) \quad \text{Eq. 5-4}$$

where $\dot{\gamma}^\alpha$ is the slip rate of slip system α , τ^α is the applied resolved shear stress on the slip system α , g_c^α is the slip resistance of slip system α , $\dot{\gamma}_0$ and m are material parameters. The hardening rate can be expressed by:

$$\dot{g}_c^\alpha = \sum_{\beta=1}^n h_{\alpha\beta} |\dot{\gamma}^\beta| \quad \text{Eq. 5-5}$$

where $h_{\alpha\beta}$, which presents the micromechanical interaction between any two systems, can be given as:

$$h_{\alpha\beta} = h_0 [q + (1 - q) \delta^{\alpha\beta}] \left| 1 - \frac{g^\beta}{g_\infty} \right|^a \text{sgn} \left(1 - \frac{g^\beta}{g_\infty} \right) \quad \text{Eq. 5-6}$$

where h_0 , a , g_∞ are slip hardening parameters that are determined by experiment, $q_{\alpha\beta}$ is the lateral hardening parameter which is given as:

$$q_{\alpha\beta} = \begin{cases} 1; & \alpha, \beta \text{ coplanar} \\ 1.4; & \text{otherwise} \end{cases} \quad \text{Eq. 5-7}$$

The CPFE simulation was performed using the model of phenomenological crystal plasticity, which was implemented in DAMASK software [180], as a user subroutine of ABAQUS. The micropillar used in the CPFE simulation is shown in *Figure 5-2*, and the diameter and height of the ER5 pillar are 6.8 μm and 20.4 μm , respectively. The diameter of the ER4 pillars is 2 μm and the height is 6 μm . The pillars were connected to the substrate with the same orientation. The top surface of each pillar was compressed by an indenter with a flat rigid surface. The friction coefficient between the indenter and the top surface of the pillar was set to 0.14 to prevent the slip between the indenter and the top of the pillar [181]. The compression rate was $1 \times 10^{-3} \text{ s}^{-1}$ which matched the experimental condition.

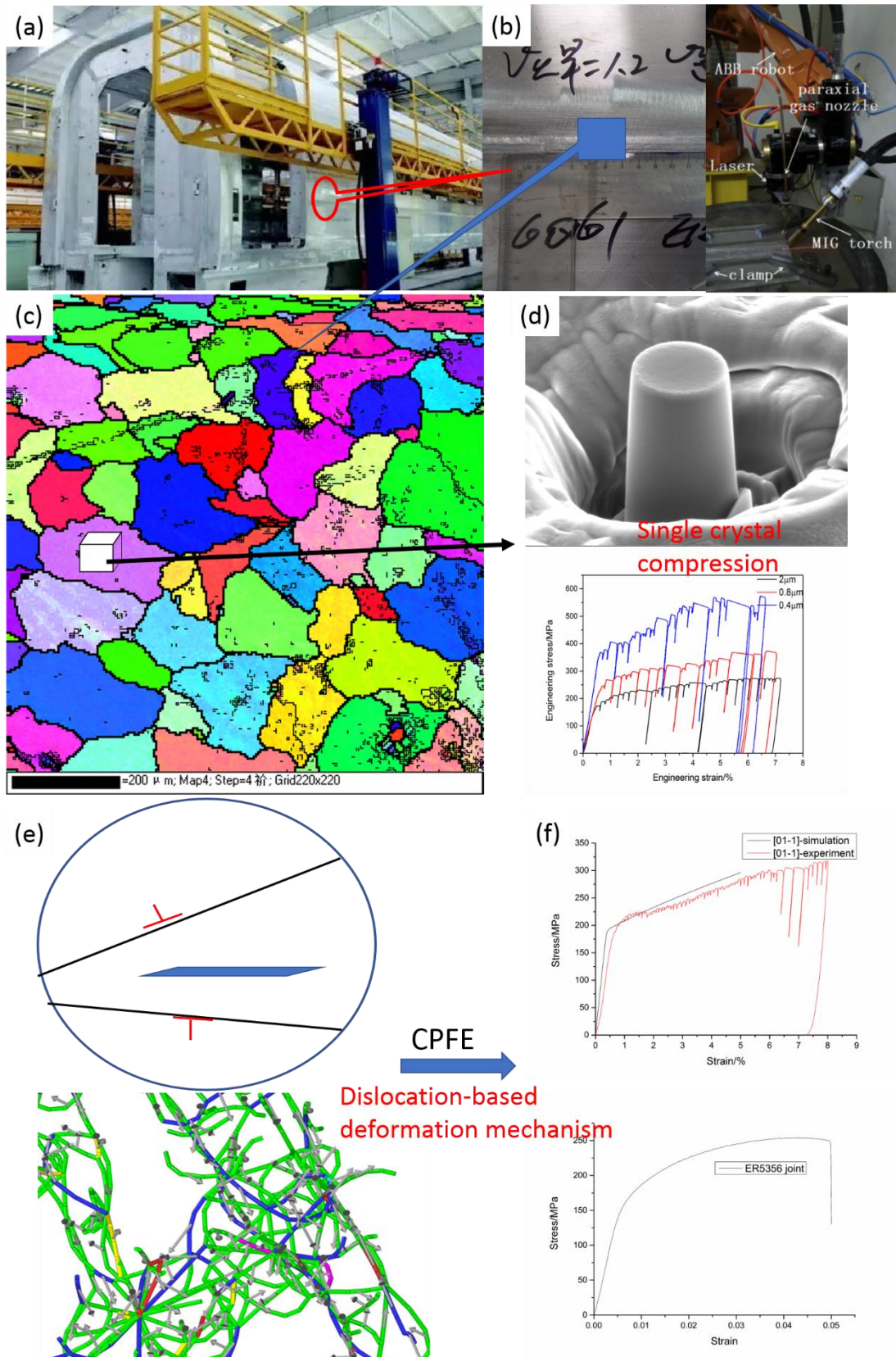


Figure 5-1 (a) High-speed train body made of aluminium alloys, (b) AA6061 welded by hybrid laser welding, (c) EBSD characterization of the cross-section of the FZ, (d) SC compression testing for the selected grain in (c), (e) dislocation-based mechanism, (f) CPFE employed to simulate the stress-strain curves for SC and polycrystal of the weld.

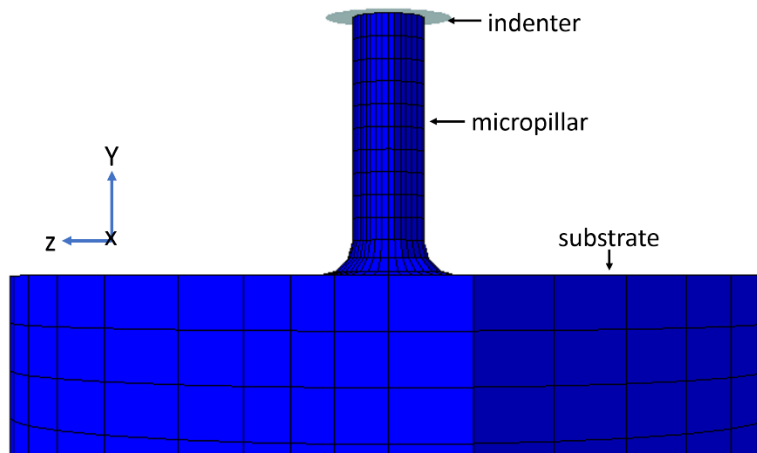


Figure 5-2 CPFE simulation model of single crystal.

5.3 Results

5.3.1 CPFE simulation on the single crystal of the ER5 pillar

Theoretical and numerical approaches [182-192] are powerful for analysing engineering problems such as identification of material parameters and analysis of plasticity and dislocation behaviour. In this section, a CPFE model is constructed and the material parameters used in the CPFE model are determined by fitting the stress-strain curve from simulation to the one from micropillar experiments. As shown in *Figure 3-9c*, the strength of the pillar increases when the sample's diameter decreases. To accurately predict the strength of the welded joint at macroscale, the choice of the sample with an appropriate diameter is crucial. As shown in *Figure 3-9c*, the size effect on the strength of the pillar disappears when the sample's diameter is greater than $3.2\ \mu\text{m}$. That means the mechanical response of the pillar with a diameter larger than $3.2\ \mu\text{m}$ can represent the bulk's behaviour when the pillar is subject to external loading. Hereafter, the experimental data of the [101]-oriented sample with diameter of $\sim 6.8\ \mu\text{m}$ is used to obtain the material parameters for the CPFE simulation. The procedure for determining material parameters is shown in *Figure 5-3*. After many optimizations, the material parameters for the ER5 single crystal are shown in *Table 5-1*.

The stress-strain curves from the CPFÉ simulation and experiment for three crystalline orientations, [101], [111], and [-301], are shown in *Figure 5-4*. For the three orientations, the elastic strain stage from simulation did not match perfectly with that from experiment. This discrepancy is due to the misalignment between the top of the pillar and the flat-end tip [193, 194]. This misalignment appears to decrease in the smaller samples, as demonstrated by the slope of the elastic period in the 400 nm-diameter sample in *Figure 3-9 a-b*. The experimental stress-strain curves for the 400 nm-diameter sample were also fitted. The results, *Figure 5-4d*, show fairly good agreement between the simulation and experiment even in the elastic strain period, suggesting that the deformation of a single crystal of the FZ can be accurately predicted by CPFÉ simulation. The yield strengths from simulation and experiment are very close each other, as demonstrated in

Table 5-2. It is worth mentioning that the yield strength from the simulation was the strength at the strain of 0.2%, whereas the yield strength from the experiment was the strength from the first strain burst. The stress distribution of the Von Mises stress is shown in *Figure 5-5*. For comparison, the SEM images of the deformed pillar are also shown. It can be seen from *Figure 5-5* that the slip can be accurately predicted by the simulation. The [101]-oriented sample shows double slips, whereas the other two orientations show single slips.

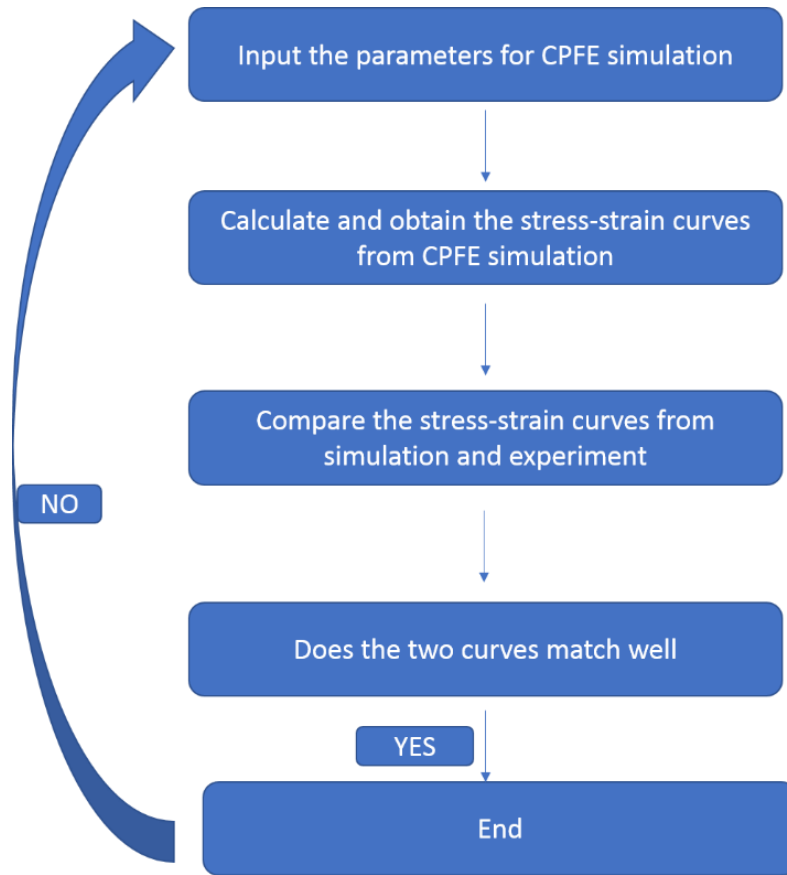


Figure 5-3 Procedure for determining the material parameters used in CPF simulation.

Table 5-1 Material parameters used in ER5 pillar for crystal plasticity finite element simulation. The unit of C_{11} , C_{12} , C_{44} is GPa, of g_0 , g_∞ , and h_0 is MPa, and of $\dot{\gamma}_0$ is s^{-1} .

C_{11}	C_{12}	C_{44}	g_0	g_∞	h_0	$\dot{\gamma}_0$	m	a	Coplanar $q_{\alpha\beta}$	Non- coplanar $q_{\alpha\beta}$
106	60	28	65	500	780	0.001	20	2.25	1.0	1.4

Table 5-2 Yield strength obtained from simulation and experiment for ER5 joints, the unit is MPa.

	[101]	[111]	[-301]	Bulk polycrystal
From simulation	132	182	128	173
From experiment	135	170	125	170

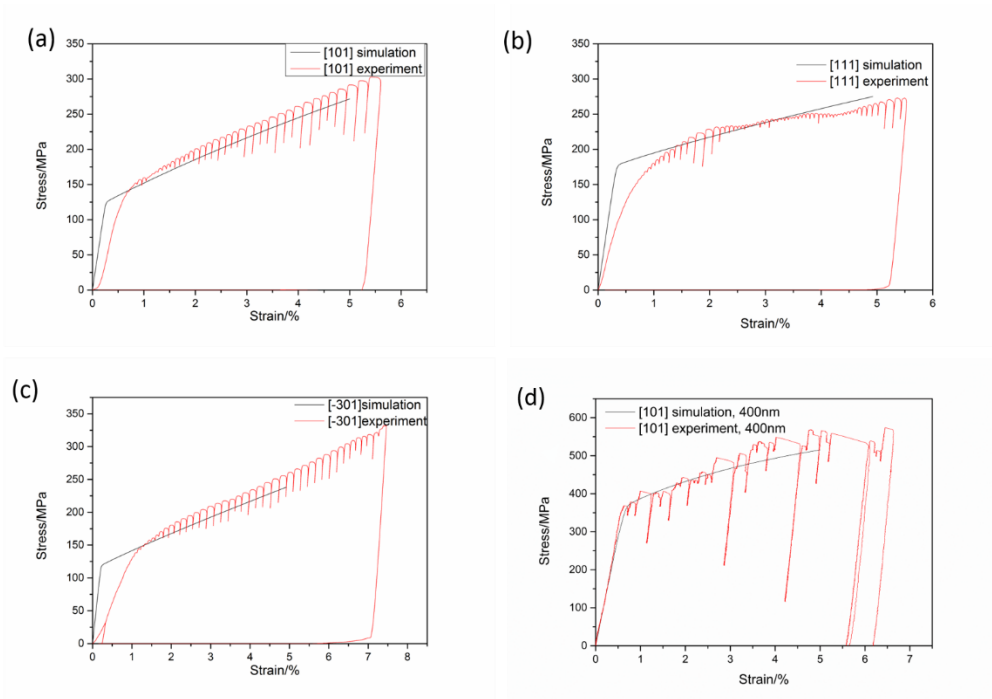


Figure 5-4 Stress-strain curves from both simulation and experiment for the orientation of (a) [101], (b) [111], (c) [-301], and (d) [101]-oriented 400nm-diameter sample.

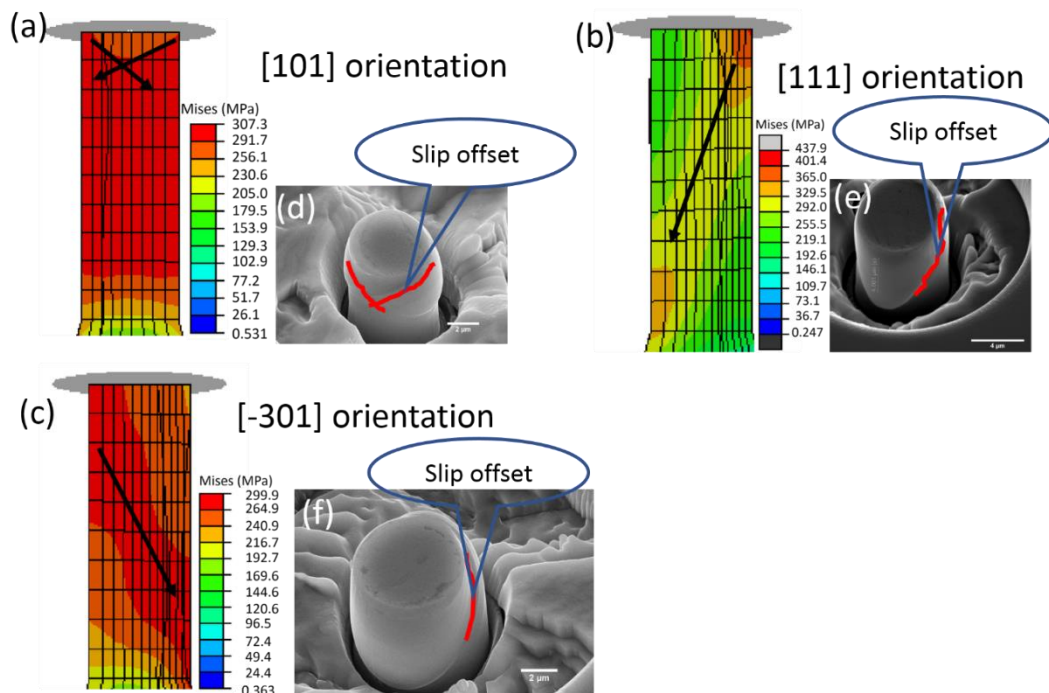


Figure 5-5 Von Mises stress of orientation (a) [101], (b) [111], (c) [-301]; SEM images for the deformed pillar of orientation (d) [101], (e) [111], and (f) [-301].

5.3.2 CPFE simulation on the single crystal of ER4 pillar

Since there is no size effect on the strength of ER4 pillars at microscale (see *Figure 4-4c*), the microplasticity of 2 μ m-diameter pillar was used to determine the material parameters. Similar procedure as described in *Figure 5-3* was applied to simulate the deformation behaviour of ER4 pillars, the optimized material parameters are listed in *Table 5-3*. The according stress-strain curves from CPFE simulation for the tested three orientations are shown in *Figure 5-6*. It can be seen from *Figure 5-6* that there are good agreements between the simulation and experiment. The stress distribution of the Von Mises stress is shown in *Figure 5-7*. For comparison, the SEM images of the deformed pillar are also shown. It can be seen from *Figure 5-7* that the slip can be accurately predicted by the simulation. The [10-1]-oriented sample shows double slips, while the other two orientations show single slip.

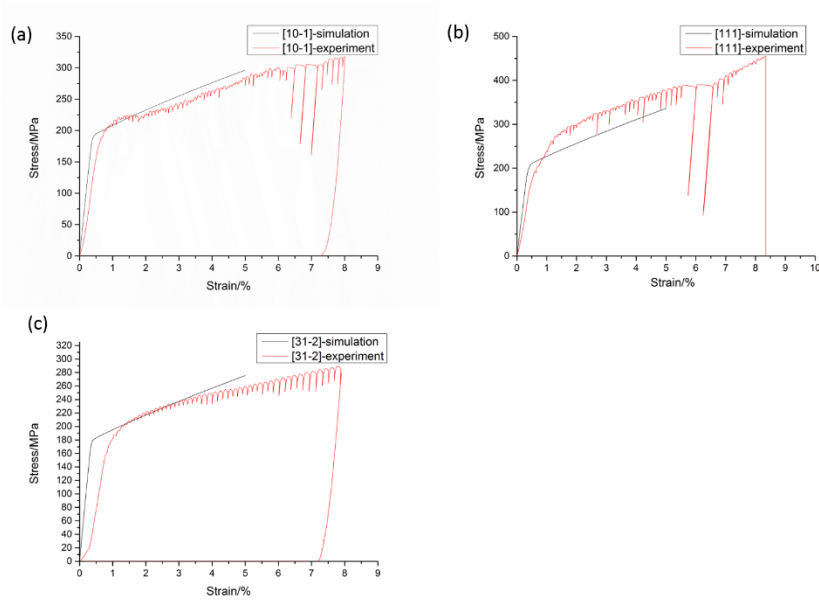


Figure 5-6 Stress-strain curves from both simulation and experiment for the orientation of (a) [10-1], (b) [111], (c) [31-2].

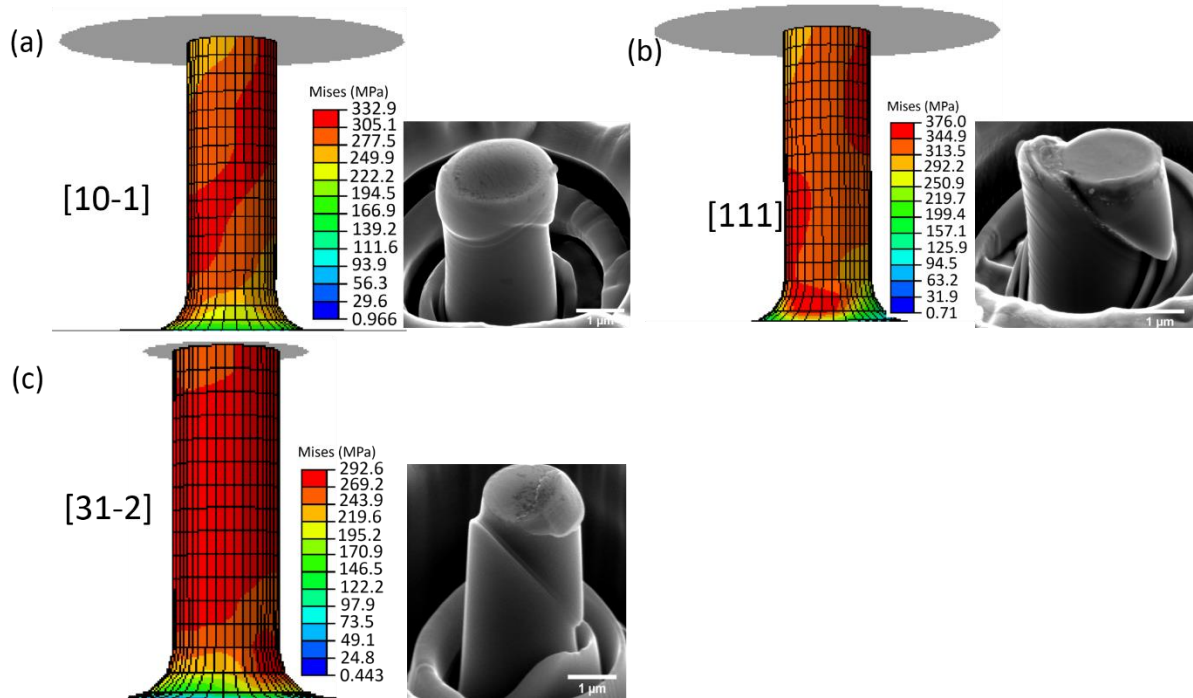


Figure 5-7. Von Mises stress and SEM images of the deformed morphology of orientation (a) [10-1], (b) [111], (c) [31-2].

Table 5-3 Material parameters used in ER4 pillar for crystal plasticity finite element simulation. The unit of C_{11} , C_{12} , C_{44} is GPa, g_0 , g_∞ , and h_0 is MPa, and $\dot{\gamma}_0$ is s^{-1} .

C_{11}	C_{12}	C_{44}	g_0	g_∞	h_0	$\dot{\gamma}_0$	m	a	Coplanar $q_{\alpha\beta}$	Non-coplanar $q_{\alpha\beta}$
106	60	28	90	650	650	0.001	20	2.25	1.0	1.4

5.3.3 CPFE on the compressive deformation behaviour of polycrystals

As demonstrated in section 5.3.1 and 5.3.2, the CPFE simulation successfully repeats the performance of single crystals under compressive loading at microscale. In this section, a macro-mechanical CPFE model based on microscale crystal plasticity is constructed to mimic the deformation of polycrystal samples of ER4 joints under compressive loading. With the Euler angles obtained from EBSD tests and software Neper [195], the obtained model is shown in *Figure 5-8a*, which had 157 grains with averaged grain size of 71 μm . The colours

were assigned according to the Euler angles obtained from EBSD testing. The dimensions of the model were $0.17 \times 0.17 \times 0.52 \text{ mm}^3$.

After finishing the model, simulation was conducted to reproduce the mechanical behaviour of the FZ under compressive loading with the same material parameters in *Table 5-3*. The results from the simulation and experiments are illustrated in *Figure 5-8b*. Similar to the results of single crystals, results from the simulation and experiment in the elastic stage did not match perfectly. However, the yield strength could be well predicted, with the simulation and experimental results being 245 MPa and 250 MPa, respectively. In the hardening period, fair good agreement was achieved between the simulation and experiments, as illustrated in *Figure 5-8b*. The morphology (*Figure 5-8c*) of the sample at final stage of strains shows that the stress in some places are higher than others.

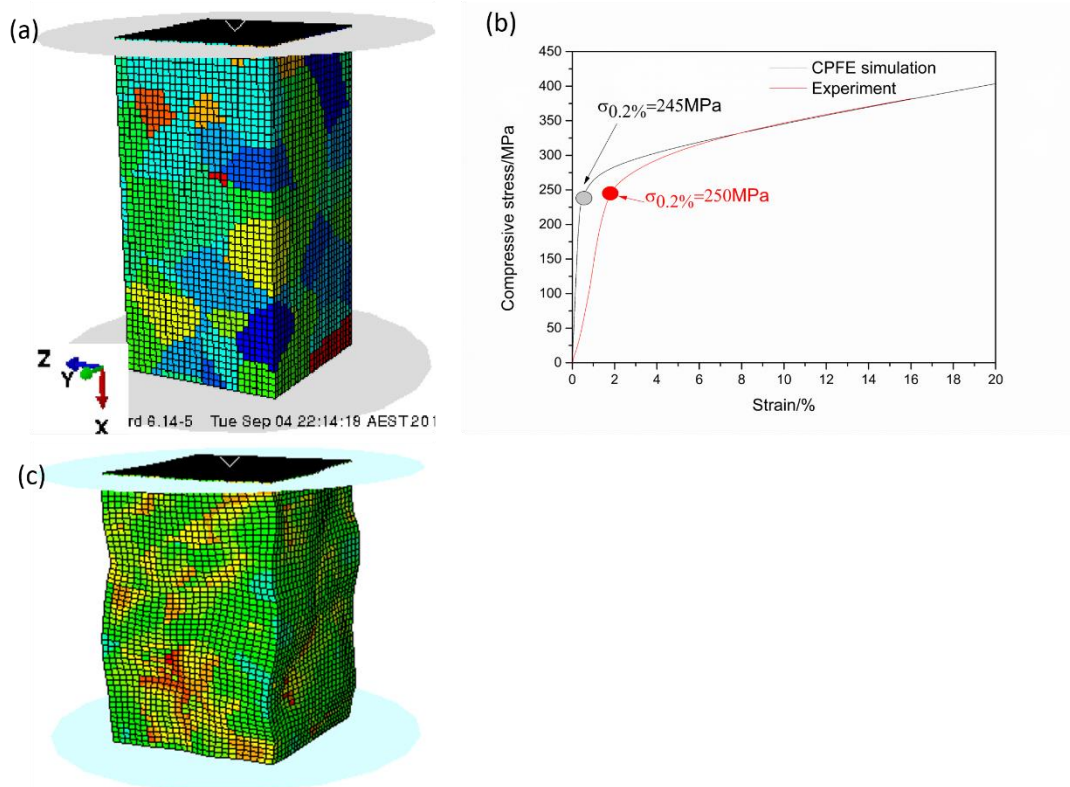


Figure 5-8. (a) Polycrystal model for CPF simulation, (b) results from the macro-mechanical model and experiments, (c) stress distribution in the model at the final tested strains.

5.3.4 CPFE on the tensile deformation behaviour of polycrystals

After demonstrating that the crystal plasticity obtained at microscales could be used to predict the bulk's compressive mechanical behaviour utilizing CPFE simulation (see *Figure 5-8*), a further step was taken to see if the current CPFE model could be used to mimic the deformation behaviour under tensile testing, given that most of the engineering components fail under tensile stress. A macro-mechanical CPFE model was constructed and used to simulate the tensile deformation behaviour of the ER5 and ER4 joints.

As shown in *Figure 5-9a*, the built model with dimensions of $1.75 \times 0.4375 \times 0.07 \text{ mm}^3$ is made of 157 grains with the grain size of $71 \text{ }\mu\text{m}$, as determined by the EBSD test. The different colours present different crystalline orientations abstracted from the EBSD test. The predicted stress-strain curves and the experimental curves are shown in *Figure 5-9b*. The good agreement between them is achieved, especially for the yield strength. The Von Mises stress distribution at 5% strain is shown in *Figure 5-9c*. The stress is not evenly distributed in the sample with some grains showing higher stress. The results of CPFE simulation of the ER4 joint are shown in *Figure 5-10*. Similarly, there is a good agreement between the simulation and the experiment, especially for the yield strength.

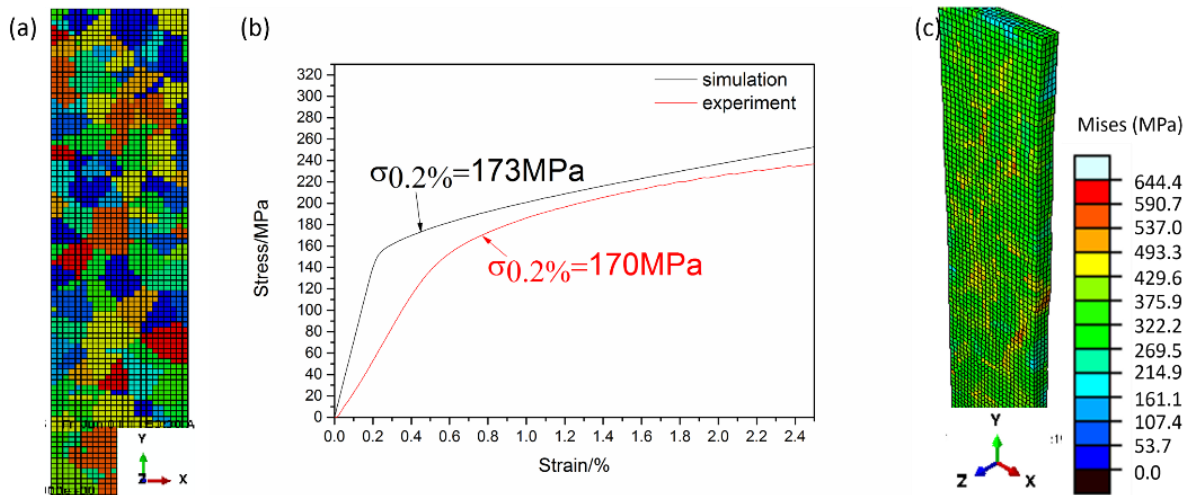


Figure 5-9. (a) CPFE polycrystal model for tensile test of the ER5 joint, (b) tensile stress-strain curves from experiment and simulation with the yield stress showing in the image, (c) Von Mises stress distribution after 5% strain in CPFE simulation

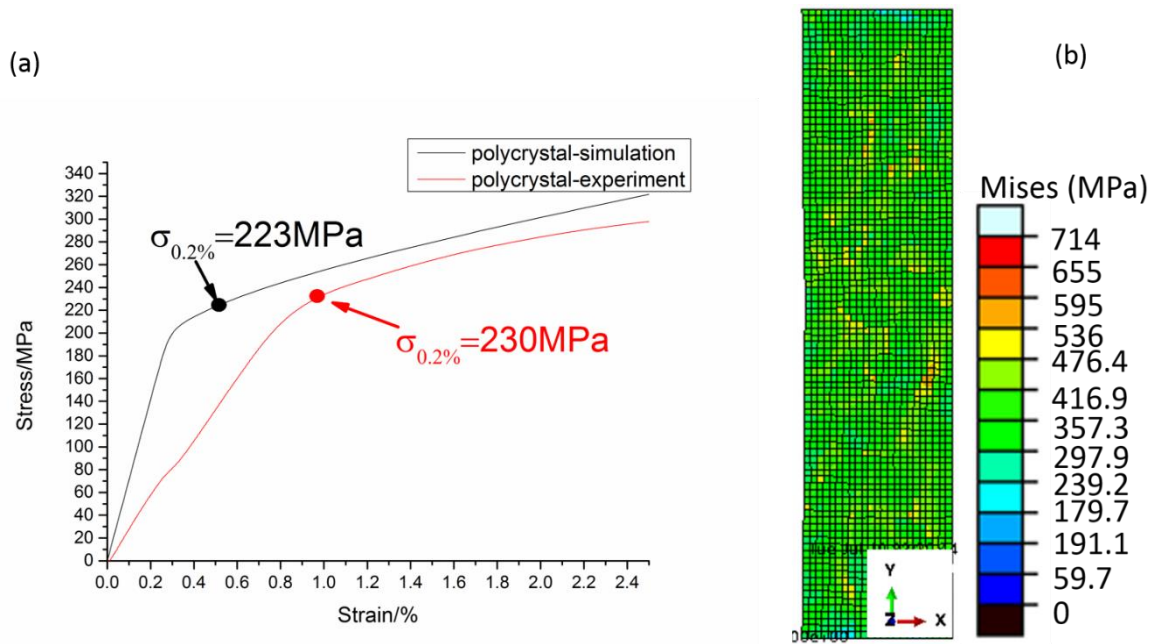


Figure 5-10. (a) Tensile stress-strain curves from experiment and simulation with the yield stress shown in the image, (c) Von Mises stress distribution after 5% strain in CPFE simulation.

5.4 Discussion

As demonstrated in *Figure 5-4* and *Figure 5-6*, the mechanical response at microscale of a SC in the FZ was reasonably well predicted by CPFE simulation, a finding which is similar to the published results [59, 196, 197]. However, the common problem for simulation is the

discrepancy of the elastic period. The slope of the elastic period in the stress-strain curves from simulation results is greater than that of the experimental results (*Figure 5-4a-c*). In the simulation, Hooke's law determined the slope. But in the experiment, the main factor influencing the slope was the misalignment between the tip and the pillar. The misalignment caused some areas to deform plastically before others, resulting in a smaller slope as demonstrated at the early stage of the deformation (see *Figure 5-4a*). Thus, the elastic period of the pillar is not reflective of pure elastic deformation, with some local plastic deformation is involved. Nevertheless, the plastic deformation is the focus during the simulation, and the results show that good agreement could be obtained through CPFÉ simulation.

The material parameters obtained by fitting the single crystal, as shown in *Table 5-1* and *Table 5-3*, could be successfully used to predict the mechanical behaviour of polycrystals of the welded joint under compressive loading, as demonstrated by the results in *Figure 5-8*. The yield stress for both joints is accurately predicted by CPFÉ simulation. The strain hardening behaviour also shows a good agreement between the simulation and experiment. The results suggest that the microplasticity obtained by the micropillar compression test can be employed to predict the onset of plasticity of the welded joint precisely.

However, one aspect that needs to be taken into consideration is the size effect on the strength at microscale, as mentioned in Chapters 3 and 4. Generally, sample with smaller size had stronger strength. If the plasticity of smaller sized sample (e.g., 400nm-diameter pillar in this research) is used to predict the macroscale mechanical properties, much higher strength would be obtained. Thus, the choice of the size of the sample requires special care.

One of the drawbacks in this study is that porosity is not taken into consideration when simulating the mechanical properties of the welded joint. It is well known that porosity can reduce the elastic modulus of material [198, 199]. Since porosity is not included in the CPFÉ

model, a direct outcome is mismatch of the elastic period in the stress-strain curves, as seen *Figure 5-9b* and *Figure 5-10a*. As this research focused on the mechanical properties under statistic loading, the residual stress, which is known to affect the fatigue strength of welded joints [200, 201], is not considered.

5.5 Conclusions

- (1) A micromechanical CPFGE model was successfully constructed and applied to simulate the compressive behaviour of single crystals of the FZ at microscale, and the material parameters used in the micromechanical model could be obtained from micropillar compression testing.
- (2) A marco-mechanical CPFGE model was proposed from the microplasticity and used to precisely mimic the deformation of ER4 joints under compressive loading, especially in the yield strength and hardening period; the onset of plasticity under tensile testing of the ER4 joint was also precisely predicted by CPFGE simulation based on the microplasticity of the 2 μm -diameter pillar, with the predicted yield strength (223 MPa) very close to that found experimentally (230 MPa).
- (3) Base on the microplasticity of pillars with the diameter of 6.8 μm , A marco-mechanical CPFGE model could accurately predict the onset of plasticity of the ER5 joint, with the predicted yield strength (173 MPa) very close to that found experimentally (170 MPa).

Chapter 6 Summary and outlook of this research

The scope of this research covered:

1. Exploring a way to toughen the welds by utilizing different filling materials, identifying the strengthening mechanisms governing the mechanical properties of the welds, and providing a guideline for selecting appropriate filling materials when hybrid laser welding of Al-Mg-Si alloys;
2. Investigating the nano/microplasticity of the FZ via pillar compression at nano/microscale. The effects of solutes, dislocation density, and crystal orientations on the nano/microplasticity of the FZ were examined;
3. Providing a novel method that could bridge the gap between nano-plasticity and macro-plasticity, using experiments and crystal plasticity finite elements simulation.

6.1 Summary of this thesis

6.1.1 Macroscale study of the microstructure and properties

To find a way to strengthen hybrid laser welds, two filling materials, ER5356 and ER4043, were used to join AA60661. For simplicity, the joints with ER5356 and ER4043 were denoted as the ER5 and ER4 joints, respectively. The microstructure and macroscale properties of the welds were characterized and compared. It was found that:

1. Although the heat input was similar for the two joint types, the microstructures of these two joints differed, with the ER4 joint featuring smaller grain size, higher dislocation density, greater porosity, and higher contents of Si, Fe, and Cu.
2. The ER4 joint showed superior mechanical properties at macroscale. When a strength model was built and utilized, it was found that the greater strength in the ER4 joint was due to grain boundary strengthening and solid solution strengthening. Coarsened

and wide-spaced precipitates made little contribution to the onset strength of the welded joint.

3. The fatigue and corrosion resistance of the ER4 joint were inferior to those of the ER5 joint because of higher density of micropores and contents of Si, Fe, and Cu.
4. A comparison was made from the manufacturing processes to the properties of both joints, which provided new clues for selecting appropriate filling materials for hybrid laser welding AA60661.

6.1.2 Nano/microscale study of the plasticity of the fusion zone

After a sound joint had been obtained, attempts were made to predict the strength of the joint using crystal plasticity finite element simulation. Keeping in mind the fact that both joints were broken in the FZ which withstood almost all strains as well, the onset plasticity of the welded joint was predicted based on the plasticity of the FZ. Unlike the macroscale mechanical test on the FZ which did not take anisotropic behaviour into consideration, for the first time, the plasticity of the single crystal in the fusion zone at microscale was investigated. Since the grain size was large in the FZ (at least 57 μm), the pillar was made in a single crystal with various crystal orientations and diameters. A summary of the microscale study is as follows:

For the pillars taken from the FZ of ER5 joint (referred as ER5 pillars)

1. The sample's diameter could affect the yield stress of the ER5 pillar, presenting a trend of "smaller is stronger", when the diameter was less than 3.3 μm . The size-dependent stress of the ER5 pillar could be expressed by a power law, $\sigma \propto D^m$. The value of m was about -0.45, which is less than that of pure FCC Al, but would become -0.9 if the strength of the bulk considered.

2. Size-dependent stress was not affected by the crystal orientations. However, the crystal orientation played a key role in the yield stress, a finding which can be explained by Schmid's law. The orientation-dependent strength decreased with the increase in the pillar's diameter.
3. A theoretical model was successfully built and used to explain the observed size-dependent strength in the FZ.
4. The bulk's yield stress was obtained by utilizing the laws of $\sigma_{size} = \sigma_{bulk} + A \cdot D^{-n}$, with n being -0.9.
5. With increasing dislocation density, size- and orientation-dependent strength disappeared in ER5 pillars, and the deformation mechanism changed into dislocation interaction.

For the pillars taken from the FZ of the ER4 joint (referred as ER4 pillars)

1. Size-dependent stress was not observed for the ER4 pillars in the studied orientations and diameters (400 nm to 3.2 μm), a result which was possibly due to a stronger dragging effect from solutes.
2. Surprisingly, the crystal orientation had no influence on the yield stress of the ER4 pillars, a finding which could not be explained by the Schmid's law.
3. Given the same orientation, the dislocation density of the ER4 pillar was higher than that of the ER5 pillar. Moreover, the larger pillar had a higher dislocation density than the smaller ones.
4. When the dislocation density was increased by pre-deformation on the pillar, the size-dependent and orientation-dependent stress disappeared in ER4 pillars.
5. Dislocation interaction and solid-solution strengthening were found to be the deformation mechanism for the previously-deformed pillars.

6.1.3 Predicting plasticity from microscale to macroscale

After the examination of macroscale and microscale plasticity was completed, CPFE simulation was used to link the plasticity at multiscale. It was found that:

1. The compressive mechanical behaviour of single crystals at microscale in the FZ was predicted well by CPFE simulation, especially the yield stress.
2. By fitting the stress-strain curves of single crystals from simulations and experiments, the material parameters for CPFE simulation were obtained.
3. With the same material parameters, CPFE simulation was successfully applied to predict the deformation of the welds at macroscale.

6.2 Highlights

The research highlights of this thesis are as follows:

1. An in-depth comparison was conducted on hybrid laser-welded AA6061-T6 joints with different filling materials by characterizing microstructures and properties at macroscale.
2. A strength model was built and used to predict and explain the enhanced static strength of the welds at macroscale.
3. A recommendation for selecting appropriate filling materials was developed by comparisons from processing to in-service properties.
4. Comparative study was conducted of the nano/microplasticity of single crystals in FZ of the ER5 joint via pillar compression at small scales. The nano/microplasticity in the FZ depended significantly on the sample's size and crystal orientation, the influence of which decreased in larger samples. Numerical models were constructed and used to assess the size and orientation effects.

5. No size or orientation effects on the strength were observed for the single-crystal pillar from the FZ in the ER4 joint due to the dragging effect from solutes.
6. With an increase in the dislocation density in the pillar of the FZ from both joints, the size-dependent and orientation-dependent strength disappeared at microscale. However, the yield strength of the pillar increased due to the higher dislocation density.
7. Macro-plasticity was successfully predicted by CPFЕ simulation based on the microplasticity obtained by micropillar compression tests.

6.3 Future works

1. Quantitative prediction of the yield strength of hybrid laser-welded AA6061-T6 joints yields new clues as to how to strengthen welded joints, such as changing the grain size and increasing the dislocation density. Due to the limitation of available industrial filling materials, only two filling materials were used in this research. In future, if possible, some other alloying elements which can increase the solidification speed or increase the dislocation density could be used in the filling material to alter the microstructure of the FZ.
2. Success in predicting the static mechanical properties of the welded joint using microplasticity as shed new lights on simulating more problematic issues, such as fatigue crack initiation and crack-dislocation interaction. Moreover, with the microplasticity of single crystals, a model could be built to simulate the influence of porosity on fatigue strength.

3. Furthermore, the micropillar study could be used to investigate the mechanical properties of single grain boundary, or to study stress corrosion cracking which is an issue of concern in high-strength Al alloys (such as AA7xxx), where understanding of the mechanism is still inconclusive.

4. In this research, the multiscale investigation conducted only the crystal plasticity of single crystals, which might be enough for static mechanical properties. However, the dynamic properties of welds could be influenced by the residual stress and grain boundary segregations, which were not included in this research. Thus, in the near future, these factors should be taken into consideration when investigating the properties (such as fatigue resistance and SCC) of welds.

Bibliography

- [1] W.M. Steen, Arc augmented laser processing of materials, *Journal of Applied Physics*, 51(11) (1980) 5636-5641.
- [2] L. Huang, D. Wu, X. Hua, S. Liu, Z. Jiang, F. Li, H. Wang, S. Shi, Effect of the welding direction on the microstructural characterization in fiber laser-GMAW hybrid welding of 5083 aluminum alloy, *Journal of Manufacturing Processes*, 31 (2018) 514-522.
- [3] H.W. Wang, Y.L. Kang, Z.F. Zhang, Q.H. Qin, Size effect on the fracture toughness of metallic foil, *Int J Fract*, 123(3) (2003) 177-185.
- [4] Y.L. Kang, Z.F. Zhang, H.W. Wang, Q.H. Qin, Experimental investigations of the effect of thickness on fracture toughness of metallic foils, *Mat Sci Eng A-Struct*, 394(1) (2005) 312-319.
- [5] X. Wang, K.J. Si, J. Yang, X. Wu, Q.H. Qin, W. Cheng, Y. Lu, Ultra-sensitive photon sensor based on self-assembled nanoparticle plasmonic membrane resonator, in: 2016 IEEE 29th International Conference on Micro Electro Mechanical Systems (MEMS), IEEE, 2016, pp. 1058-1061.
- [6] S. Yan, H. Chen, Z. Zhu, G. Gou, Hybrid laser-Metal Inert Gas welding of Al–Mg–Si alloy joints: Microstructure and mechanical properties, *Materials & Design*, 61 (2014) 160-167.
- [7] B. Ribic, T.A. Palmer, T. DebRoy, Problems and issues in laser-arc hybrid welding, *International Materials Reviews*, 54(4) (2013) 223-244.
- [8] U. Dilthey, A. Wiesschemann, Perspectives offered by combining a laser beam with arc welding procedures, *Welding International*, 16(9) (2002) 711-719.
- [9] G. Ming, Z. Xiaoyan, H. Qianwu, Effects of gas shielding parameters on weld penetration of CO₂ laser-TIG hybrid welding, *Journal of Materials Processing Technology*, 184(1-3) (2007) 177-183.

- [10] B. Acherjee, Hybrid laser arc welding: State-of-art review, *Optics & Laser Technology*, 99 (2018) 60-71.
- [11] B. Hu, I.M. Richardson, Mechanism and possible solution for transverse solidification cracking in laser welding of high strength aluminium alloys, *Materials Science and Engineering: A*, 429(1-2) (2006) 287-294.
- [12] C. Zhang, M. Gao, D. Wang, J. Yin, X. Zeng, Relationship between pool characteristic and weld porosity in laser arc hybrid welding of AA6082 aluminum alloy, *Journal of Materials Processing Technology*, 240 (2017) 217-222.
- [13] I. Bunaziv, O.M. Akselsen, A. Salminen, A. Unt, Fiber laser-MIG hybrid welding of 5 mm 5083 aluminum alloy, *Journal of Materials Processing Technology*, 233 (2016) 107-114.
- [14] S. Katayama, Naito Yasuaki, Uchiumi Satoru, Mizutani Masami, Physical Phenomena and Porosity Prevention Mechanism in Laser-Arc Hybrid Welding, *Transactions of JWRI*, 35 (2006) 13-18.
- [15] S. Wu, X. Yu, R. Zuo, W. Zhang, H. Xie, J. Jiang, Porosity, element loss, and strength model on softening behavior of hybrid laser arc welded Al-Zn-Mg-Cu alloy with synchrotron radiation analysis, *Welding Journal*, 92(3) (2013) 64-71.
- [16] S. Yan, Y. Nie, Z. Zhu, H. Chen, G. Gou, J. Yu, G. Wang, Characteristics of microstructure and fatigue resistance of hybrid fiber laser-MIG welded Al-Mg alloy joints, *Applied Surface Science*, 298 (2014) 12-18.
- [17] L. Wang, M. Gao, C. Zhang, X. Zeng, Effect of beam oscillating pattern on weld characterization of laser welding of AA6061-T6 aluminum alloy, *Materials & Design*, 108 (2016) 707-717.

- [18] X. Wang, S. Mao, P. Chen, Y. Liu, J. Ning, H. Li, K. Zang, Z. Zhang, X. Han, Evolution of microstructure and mechanical properties of a dissimilar aluminium alloy weldment, *Materials & Design*, 90 (2016) 230-237.
- [19] X. Zhan, J. Chen, J. Liu, Y. Wei, J. Zhou, Y. Meng, Microstructure and magnesium burning loss behavior of AA6061 electron beam welding joints, *Materials & Design*, 99 (2016) 449-458.
- [20] C. Zhang, M. Gao, G. Li, C. Chen, X.Y. Zeng, Strength improving mechanism of laser arc hybrid welding of wrought AA 2219 aluminium alloy using AlMg5wire, *Science and Technology of Welding and Joining*, 18(8) (2013) 703-710.
- [21] P. Leo, S. D'Ostuni, G. Casalino, Hybrid welding of AA5754 annealed alloy: Role of post weld heat treatment on microstructure and mechanical properties, *Materials & Design*, 90 (2016) 777-786.
- [22] S. Yan, B. Xing, H. Zhou, Y. Xiao, Q.-H. Qin, H. Chen, Effect of filling materials on the microstructure and properties of hybrid laser welded Al-Mg-Si alloys joints, *Materials Characterization*, 144 (2018) 205-218.
- [23] S. Yan, H. Chen, C. Ma, Y. Nie, X. Wang, Q.H. Qin, Local corrosion behaviour of hybrid laser-MIG welded Al-Zn-Mg alloy joints, *Materials & Design*, 88 (2015) 1353-1365.
- [24] A. Fritzsche, K. Hilgenberg, F. Teichmann, H. Pries, K. Dilger, M. Rethmeier, Improved degassing in laser beam welding of aluminum die casting by an electromagnetic field, *Journal of Materials Processing Technology*, 253 (2018) 51-56.
- [25] A. Ascari, A. Fortunato, L. Orazi, G. Campana, The influence of process parameters on porosity formation in hybrid LASER-GMA welding of AA6082 aluminum alloy, *Optics & Laser Technology*, 44(5) (2012) 1485-1490.

- [26] W. Tao, Z. Yang, C. Shi, D. Dong, Simulating effects of welding speed on melt flow and porosity formation during double-sided laser beam welding of AA6056-T4/AA6156-T6 aluminum alloy T-joint, *Journal of Alloys and Compounds*, 699 (2017) 638-647.
- [27] G. Gou, M. Zhang, H. Chen, J. Chen, P. Li, Y.P. Yang, Effect of humidity on porosity, microstructure, and fatigue strength of A7N01S-T5 aluminum alloy welded joints in high-speed trains, *Materials & Design*, 85 (2015) 309-317.
- [28] C. Sharma, D.K. Dwivedi, P. Kumar, Effect of post weld heat treatments on microstructure and mechanical properties of friction stir welded joints of Al-Zn-Mg alloy AA7039, *Materials & Design*, 43 (2013) 134-143.
- [29] Z.Y. Zhu, C.Y. Deng, Y. Wang, Z.W. Yang, J.K. Ding, D.P. Wang, Effect of post weld heat treatment on the microstructure and corrosion behavior of AA2219 aluminum alloy joints welded by variable polarity tungsten inert gas welding, *Materials & Design* 65 (2015) 1075-1082.
- [30] M. Cabibbo, A. Forcellese, M. Simoncini, M. Peralisi, D. Ciccarelli, Effect of welding motion and pre-/post-annealing of friction stir welded AA5754 joints, *Materials & Design*, 93 (2016) 146-159.
- [31] B. Wang, S.-b. Xue, C.-l. Ma, Y.-l. Han, Z.-q. Lin, Effect of combinative addition of Ti and Sr on modification of AA4043 welding wire and mechanical properties of AA6082 welded by TIG welding, *Transactions of Nonferrous Metals Society of China*, 27(2) (2017) 272-281.
- [32] R.R. Ambriz, G. Barrera, R. García, V.H. López, The microstructure and mechanical strength of Al-6061-T6 GMA welds obtained with the modified indirect electric arc joint, *Materials & Design*, 31(6) (2010) 2978-2986.

- [33] D.-Q. Zhang, J. Li, H.G. Joo, K.Y. Lee, Corrosion properties of Nd:YAG laser–GMA hybrid welded AA6061 Al alloy and its microstructure, *Corrosion Science*, 51(6) (2009) 1399-1404.
- [34] K.S. Rahman Mujibur ABM, Gerson AR, Galvanic corrosion of laser weldments of AA6061 aluminium alloy, *Corrosion Science*, 49(12) (2007) 4339-4351.
- [35] Q. Chu, R. Bai, H. Jian, Z. Lei, N. Hu, C. Yan, Microstructure, texture and mechanical properties of 6061 aluminum laser beam welded joints, *Materials Characterization*, 137 (2018) 269-276.
- [36] H. Li, P. Zhao, Z. Wang, Q. Mao, B. Fang, R. Song, Z. Zheng, The intergranular corrosion susceptibility of a heavily overaged Al-Mg-Si-Cu alloy, *Corrosion Science*, 107 (2016) 113-122.
- [37] W.J. Liang, P.A. Rometsch, L.F. Cao, N. Birbilis, General aspects related to the corrosion of 6xxx series aluminium alloys: Exploring the influence of Mg/Si ratio and Cu, *Corrosion Science*, 76 (2013) 119-128.
- [38] X. Wang, B. Li, M. Li, C. Huang, H. Chen, Study of local-zone microstructure, strength and fracture toughness of hybrid laser-metal-inert-gas-welded A7N01 aluminum alloy joint, *Materials Science and Engineering: A*, 688 (2017) 114-122.
- [39] A.H. Faraji, M. Moradi, M. Goodarzi, P. Colucci, C. Maletta, An investigation on capability of hybrid Nd:YAG laser-TIG welding technology for AA2198 Al-Li alloy, *Optics and Lasers in Engineering*, 96 (2017) 1-6.
- [40] G. Casalino, M. Mortello, P. Leo, K.Y. Benyounis, A.G. Olabi, Study on arc and laser powers in the hybrid welding of AA5754 Al-alloy, *Mater. Des.*, 61 (2014) 191-198.
- [41] Q. Puydt, S. Flouriot, S. Ringeval, F. De Geuser, R. Estevez, G. Parry, A. Deschamps, Relationship Between Microstructure, Strength, and Fracture in an Al-Zn-Mg

- Electron Beam Weld: Part II: Mechanical Characterization and Modeling, Metallurgical and Materials Transactions A, 45(13) (2014) 6141-6152.
- [42] R. Gu, A.H.W. Ngan, Size effect on the deformation behavior of duralumin micropillars, Scripta Materialia, 68(11) (2013) 861-864.
- [43] Q.H. Qin, The Trefftz finite and boundary element method, WIT Press, Southampton, 2000.
- [44] Q.H. Qin, H. Wang, Matlab and C programming for Trefftz finite element methods, CRC Press, New York, 2009.
- [45] Q.H. Qin, Trefftz finite element method and its applications, Appl Mech Rev, 58(5) (2005) 316-337.
- [46] H. Wang, Q.H. Qin, FE approach with Green's function as internal trial function for simulating bioheat transfer in the human eye, Arch Mech, 62(6) (2010) 493-510.
- [47] J. Jirousek, Q.H. Qin, Application of hybrid-Trefftz element approach to transient heat conduction analysis, Comput Struct, 58(1) (1996) 195-201.
- [48] J. Jirousek, A. Wroblewski, Q.H. Qin, X.Q. He, A family of quadrilateral hybrid-Trefftz p-elements for thick plate analysis, Comput Meth Appl Mech Eng, 127(1) (1995) 315-344.
- [49] D. Bardel, M. Fontaine, T. Chaise, M. Perez, D. Nelias, F. Bourlier, J. Garnier, Integrated modelling of a 6061-T6 weld joint: From microstructure to mechanical properties, Acta Materialia, 117 (2016) 81-90.
- [50] D. Bardel, M. Perez, D. Nelias, S. Dancette, P. Chaudet, V. Massardier, Cyclic behaviour of a 6061 aluminium alloy: Coupling precipitation and elastoplastic modelling, Acta Materialia, 83 (2015) 256-268.

- [51] A. Simar, Y. Bréchet, B. de Meester, A. Denquin, C. Gallais, T. Pardoen, Integrated modeling of friction stir welding of 6xxx series Al alloys: Process, microstructure and properties, *Progress in Materials Science*, 57(1) (2012) 95-183.
- [52] Z.H. Rao, S.M. Liao, H.L. Tsai, Modelling of hybrid laser–GMA welding: review and challenges, *Science and Technology of Welding and Joining*, 16(4) (2013) 300-305.
- [53] Q.H. Qin, Hybrid Trefftz finite-element approach for plate bending on an elastic foundation, *Appl Math Model*, 18(6) (1994) 334-339.
- [54] Q.H. Qin, Variational formulations for TFEM of piezoelectricity, *Int J Solid Struct*, 40(23) (2003) 6335-6346.
- [55] C. Cao, Q.H. Qin, Hybrid fundamental solution based finite element method: theory and applications, *Advances in Mathematical Physics*, 2015 (2015) Article ID: 916029, 916038 pages.
- [56] Q.H. Qin, Fracture Analysis of Piezoelectric Materials by Boundary and Trefftz Finite Element Methods, WCCM VI in conjunction with APCOM'04, Sept. 5-10, 2004, Beijing, China, (2004).
- [57] Q.H. Qin, Trefftz Plane Element of Piezoelectric Plate with p-Extension Capabilities, pp 144-153, in: IUTAM Symposium on Mechanics and Reliability of Actuating Materials, Springer Netherlands, 2006.
- [58] H. Wang, Y. Xiao, Q.H. Qin, 2D hierarchical heat transfer computational model of natural ber bundle reinforced composite, *Scientia Iranica, Transactions B: Mechanical Engineering*, 23(1) (2016) 268-276.
- [59] A. Cruzado, B. Gan, M. Jiménez, D. Barba, K. Ostolaza, A. Linaza, J.M. Molina-Aldareguia, J. Llorca, J. Segurado, Multiscale modeling of the mechanical behavior of IN718 superalloy based on micropillar compression and computational homogenization, *Acta Materialia*, 98 (2015) 242-253.

- [60] F. Roters, P. Eisenlohr, L. Hantcherli, D.D. Tjahjanto, T.R. Bieler, D. Raabe, Overview of constitutive laws, kinematics, homogenization and multiscale methods in crystal plasticity finite-element modeling: Theory, experiments, applications, *Acta Materialia*, 58(4) (2010) 1152-1211.
- [61] H. Zhang, M. Diehl, F. Roters, D. Raabe, A virtual laboratory using high resolution crystal plasticity simulations to determine the initial yield surface for sheet metal forming operations, *International Journal of Plasticity*, 80 (2016) 111-138.
- [62] C. Pinna, Y. Lan, M.F. Kiu, P. Efthymiadis, M. Lopez-Pedrosa, D. Farrugia, Assessment of crystal plasticity finite element simulations of the hot deformation of metals from local strain and orientation measurements, *International Journal of Plasticity*, 73 (2015) 24-38.
- [63] S. Chandra, M.K. Samal, V.M. Chavan, S. Raghunathan, Hierarchical multiscale modeling of plasticity in copper: From single crystals to polycrystalline aggregates, *International Journal of Plasticity*, 101 (2018) 188-212.
- [64] L. Patriarca, A. Ojha, H. Sehitoglu, Y.I. Chumlyakov, Slip nucleation in single crystal FeNiCoCrMn high entropy alloy, *Scripta Materialia*, 112 (2016) 54-57.
- [65] H. Abdolvand, J. Wright, A.J. Wilkinson, Strong grain neighbour effects in polycrystals, *Nature Communications*, 9(1) (2018) 171.
- [66] S.I.R. J. Krebs, S. Verheyden, C. Miko, R. Goodall, W. A. Curtin, A. Mortensen, Cast aluminium single crystals cross the threshold, *Nature materials*, 16 (2017) 730-737.
- [67] J.H. Wu, W.Y. Tsai, J.C. Huang, C.H. Hsieh, G.-R. Huang, Sample size and orientation effects of single crystal aluminum, *Materials Science and Engineering: A*, 662 (2016) 296-302.
- [68] D.M.D. Michael D. Uchic, Jeffrey N. Florando, William D. Nix, Sample Dimensions Influence strength and crystal plasticity, *Science*, 305 (2004) 986-989.

- [69] P.A.S. Michael D. Uchic, Dennis M. Dimiduk, Micro-Compression Testing of fcc Metals: A Selected Overview of Experiments and Simulations, *JOM*, 61 (2009) 36-41.
- [70] J.R. Greer, W.C. Oliver, W.D. Nix, Size dependence of mechanical properties of gold at the micron scale in the absence of strain gradients, *Acta Materialia*, 53(6) (2005) 1821-1830.
- [71] R. Dou, B. Derby, A universal scaling law for the strength of metal micropillars and nanowires, *Scripta Materialia*, 61(5) (2009) 524-527.
- [72] J.R. Greer, J.T.M. De Hosson, Plasticity in small-sized metallic systems: Intrinsic versus extrinsic size effect, *Progress in Materials Science*, 56(6) (2011) 654-724.
- [73] B. Girault, A.S. Schneider, C.P. Frick, E. Arzt, Strength Effects in Micropillars of a Dispersion Strengthened Superalloy, *Advanced Engineering Materials*, 12(5) (2010) 385-388.
- [74] H. Ghassemi-Armaki, R. Maaß, S.P. Bhat, S. Sriram, J.R. Greer, K.S. Kumar, Deformation response of ferrite and martensite in a dual-phase steel, *Acta Materialia*, 62 (2014) 197-211.
- [75] R. Raghavan, C. Kirchlechner, B.N. Jaya, M. Feuerbacher, G. Dehm, Mechanical size effects in a single crystalline equiatomic FeCrCoMnNi high entropy alloy, *Scripta Materialia*, 129 (2017) 52-55.
- [76] J. Greer, W. Nix, Nanoscale gold pillars strengthened through dislocation starvation, *Physical Review B*, 73(24) (2006).
- [77] T.A. Parthasarathy, S.I. Rao, D.M. Dimiduk, M.D. Uchic, D.R. Trinkle, Contribution to size effect of yield strength from the stochastics of dislocation source lengths in finite samples, *Scripta Materialia*, 56(4) (2007) 313-316.

- [78] Z.W. Shan, R.K. Mishra, S.A. Syed Asif, O.L. Warren, A.M. Minor, Mechanical annealing and source-limited deformation in submicrometre-diameter Ni crystals, *Nature materials*, 7(2) (2008) 115-119.
- [79] Q.-J.L. Zhang-Jie Wanga, Yi-Nan Cui, Zhan-Li Liu, Evan Maa, Ju Li, Jun Sun, Zhuo Zhuang, Ming Daoe, Zhi-Wei Shana, Subra Suresh, Cyclic deformation leads to defect healing and strengthening of small-volume metal crystals, *PNAS*, 112 (2015) 13502-13507.
- [80] S.-W. Lee, W.D. Nix, Size dependence of the yield strength of fcc and bcc metallic micropillars with diameters of a few micrometers, *Philosophical Magazine*, 92(10) (2012) 1238-1260.
- [81] Y. Zou, S. Maiti, W. Steurer, R. Spolenak, Size-dependent plasticity in an Nb₂₅Mo₂₅Ta₂₅W₂₅ refractory high-entropy alloy, *Acta Materialia*, 65 (2014) 85-97.
- [82] R.N. Prasad Rao K, Viswanathan N., Partially melted zone cracking in AA6061 welds, *Materials & Design*, 29(1) (2008) 179-186.
- [83] H. Jamshidi Aval, S. Serajzadeh, A study on natural aging behavior and mechanical properties of friction stir-welded AA6061-T6 plates, *The International Journal of Advanced Manufacturing Technology*, 71(5-8) (2013) 933-941.
- [84] GBT 15970.7-2000. National standard of China. Corrosion of metals and alloys stress corrosion testing – slow strain rate testing.
- [85] S. Kou, *Welding Metallurgy*, second ed., John Willy & Sons, New York, 2003
- [86] L.D. Miao WF, Effects of Cu Content and Preaging on Precipitation Characteristics in Aluminum Alloy 6022, *Metallurgical and Materials Transactions A*, 31A (2000) 361-371.

- [87] P. Eftekhari Milani, E.M. van der Aa, M.J.M. Hermans, I.M. Richardson, Microstructural characterisation of double pulse resistance spot welded advanced high strength steel, *Science and Technology of Welding and Joining*, 22(7) (2017) 545-554.
- [88] M.A. Kubin LP, Geometrically necessary dislocations and strain-gradient plasticity: a few critical issues, *Scripta Materialia*, 48 (2003) 119-125.
- [89] M. Calcagnotto, D. Ponge, E. Demir, D. Raabe, Orientation gradients and geometrically necessary dislocations in ultrafine grained dual-phase steels studied by 2D and 3D EBSD, *Materials Science and Engineering: A*, 527(10-11) (2010) 2738-2746.
- [90] K.D. Srivatsan TS, Magnusen P, The cyclic fatigue and final fracture behavior of aluminum alloy 2524, *Materials & Design*, 23 (2002) 129-139.
- [91] R.R. Jr, Effect of hard anodize thickness on the fatigue of AA6061 and C355 aluminium *Journal of Materials Science Letters*, 15 (1996) 1321-1323.
- [92] Y. Deng, Z. Yin, K. Zhao, J. Duan, J. Hu, Z. He, Effects of Sc and Zr microalloying additions and aging time at 120°C on the corrosion behaviour of an Al–Zn–Mg alloy, *Corrosion Science*, 65 (2012) 288-298.
- [93] X. Cao, P. Wanjara, J. Huang, C. Munro, A. Nolting, Hybrid fiber laser – Arc welding of thick section high strength low alloy steel, *Materials & Design*, 32(6) (2011) 3399-3413.
- [94] B. Gao, K. Kakimoto, Three-dimensional analysis of dislocation multiplication in single-crystal silicon under accurate control of cooling history of temperature. *Journal of Crystal Growth* 396 (2014) 7–13.
- [95] F.Z. Bu, X.M. Wang, L. Chen, S.W. Yang, C.J. Shang, R.D.K. Misra. Influence of cooling rate on the precipitation behavior in Ti–Nb–Mo microalloyed steels during continuous cooling and relationship to strength. *Materials Characterization* 102 (2015) 146–155

- [96] R.S. Ruwen Zheng, Wuyan Fan, Effects of annealing cooling rates on mechanical properties, microstructure and texture in continuous annealed IF steel, *Journal of Alloys and Compounds*, 692 (2017) 503-514.
- [97] X.M.W. F.Z. Bu, L. Chen, S.W. Yang, C.J. Shang, R.D.K. Misra, Influence of cooling rate on the precipitation behavior in Ti–Nb–Mo microalloyed steels during continuous cooling and relationship to strength, *Materials Characterization*, 102 (2015) 146-155.
- [98] I.A. Bataev, D.V. Lazurenko, S. Tanaka, K. Hokamoto, A.A. Bataev, Y. Guo, A.M. Jorge Jr. High cooling rates and metastable phases at the interfaces of explosively welded materials. *Acta Materialia* 135 (2017) 277-289.
- [99] Z.Z. Wang SC, Starink MJ, Estimation of dislocation densities in cold rolled Al-Mg-Cu-Mn alloys by combination of yield strength data, EBSD and strength models, *Journal of microscopy*, 217 (2005) 174-178.
- [100] M.J. Starink, S.C. Wang, A model for the yield strength of overaged Al–Zn–Mg–Cu alloys, *Acta Materialia*, 51(17) (2003) 5131-5150.
- [101] G.Ø. Myhr OR , Andersen SJ, Modelling of the age hardening behaviour of Al–Mg–Si alloys, *Acta Materialia*, 49 (2001) 65-75.
- [102] J. Friedel, *Dislocations*, first ed., Pergamon, Oxford, 1964
- [103] M. Vivas, P. Lours, C. Levaillant, A. Couret, M.-J. Casanove, A. Coujou, Determination of precipitate strength in aluminium alloy 6056-T6 from transmission electron microscopy in situ straining data, *Philosophical Magazine A*, 76(5) (1997) 921-931.
- [104] R.D. Roters F, Gottstein G, Work hardening in heterogeneous alloys—a microstructural approach based on three internal state variables, *Acta Materialia*, 48 (2000) 4181-4189.

- [105] R. Gu and A.H.W. Ngan, Size effect on the deformation behavior of duralumin micropillars. *Scripta Materialia* 68 (2013) 861–864
- [106] N. Hansen, Hall–Petch relation and boundary strengthening, *Scripta Materialia*, 51(8) (2004) 801-806.
- [107] <http://asm.matweb.com/search/SpecificMaterial.asp?bassnum=ma6061t6>
- [108] L.F. Deschamps A, Bréchet Y, Influence of predeformation on ageing in an Al–Zn–Mg alloy—I. Microstructure evolution and mechanical properties, *Acta Materialia*, 47 (1999) 281-292.
- [109] S.S. Buffière JY, Jouneau PH, Maire E, Fougères R, Experimental study of porosity and its relation to fatigue mechanisms of model Al–Si7–Mg0.3 cast Al alloys, *Materials Science and Engineering A*, 316 (2001) 115-126.
- [110] H. Mayer, M. Papakyriacou, B. Zettl, S.E. Stanzl-Tschegg, Influence of porosity on the fatigue limit of die cast magnesium and aluminium alloys, *International Journal of Fatigue*, 25(3) (2003) 245-256.
- [111] F. Shen, B. Zhao, L. Li, C.K. Chua, K. Zhou, Fatigue damage evolution and lifetime prediction of welded joints with the consideration of residual stresses and porosity, *International Journal of Fatigue*, 103 (2017) 272-279.
- [112] V. Gaur, M. Enoki, T. Okada, S. Yomogida, A study on fatigue behavior of MIG-welded Al-Mg alloy with different filler-wire materials under mean stress, *International Journal of Fatigue*, 107 (2018) 119-129.
- [113] S.C. Wu, C. Yu, P.S. Yu, J.Y. Buffière, L. Helfen, Y.N. Fu, Corner fatigue cracking behavior of hybrid laser AA7020 welds by synchrotron X-ray computed microtomography, *Materials Science and Engineering: A*, 651 (2016) 604-614.
- [114] B.R. Paglia CS, A look in the corrosion of aluminum alloy friction stir welds, *Scripta Materialia*, 58(5) (2008) 383-387.

- [115] F. Eckermann, T. Suter, P.J. Uggowitzer, A. Afseth, P. Schmutz, Investigation of the exfoliation-like attack mechanism in relation to Al–Mg–Si alloy microstructure, *Corrosion Science*, 50(7) (2008) 2085-2093.
- [116] K.S. Mujibur Rahman ABM, Gerson AR, The role of silicon in the corrosion of AA6061 aluminium alloy laser weldments, *Corrosion Science*, 52(6) (2010) 1969-1975.
- [117] L. Guan, B. Zhang, J.Q. Wang, E.H. Han, W. Ke, The reliability of electrochemical noise and current transients characterizing metastable pitting of Al–Mg–Si microelectrodes, *Corrosion Science*, 80 (2014) 1-6.
- [118] P. Hosemann, D. Frazer, M. Fratoni, A. Bolind, M.F. Ashby, Materials selection for nuclear applications: Challenges and opportunities, *Scripta Materialia*, 143 (2018) 181-187.
- [119] S.C. Wu, Y.N. Hu, H. Duan, C. Yu, H.S. Jiao, On the fatigue performance of laser hybrid welded high Zn 7000 alloys for next generation railway components, *International Journal of Fatigue*, 91 (2016) 1-10.
- [120] Y.T. Lin, M.C. Wang, Y. Zhang, Y.Z. He, D.P. Wang, Investigation of microstructure evolution after post-weld heat treatment and cryogenic fracture toughness of the weld metal of AA2219 VPTIG joints, *Materials & Design*, 113 (2017) 54-59.
- [121] Z. Qin, Q.H. Qin, X.-Q. Feng, Mechanical property of carbon nanotubes with intramolecular junctions: Molecular dynamics simulations, *Phys Lett A*, 372(44) (2008) 6661-6666.
- [122] K. Cai, H. Yin, Q.H. Qin, Y. Li, Self-excited oscillation of rotating double-walled carbon nanotubes, *Nano Lett*, 14(5) (2014) 2558-2562.
- [123] K. Cai, Y. Li, Q.H. Qin, H. Yin, Gradientless temperature-driven rotating motor from a double-walled carbon nanotube, *Nanotechnology*, 25(50) (2014) 505701.

- [124] J. Shi, H. Cai, K. Cai, Q.H. Qin, Dynamic behavior of a black phosphorus and carbon nanotube composite system, *J. Phys. D: Appl. Phys.*, 50 (2017) 025304.
- [125] K. Cai, H. Cai, H. Yin, Q.H. Qin, Dynamic behavior of curved double-wall carbon nanotubes with rotating inner tube, *RSC Advances*, 5(38) (2015) 29908-29913.
- [126] L. Yang, K. Cai, J. Shi, Q.H. Qin, Significance tests on the output power of a thermally driven rotary nanomotor, *Nanotechnology*, 28(21) (2017) 215705.
- [127] B. Xing, S. Yan, W. Jiang, Q.H. Qin, Deformation mechanism of kink-step distorted coherent twin boundaries in copper nanowire, *AIMS Materials Science*, 4(1) (2017) 102-117.
- [128] S. Plimpton, Fast parallel algorithms for short-range molecular dynamics, *Journal of Computational Physics*, 117 (1995) 1-19.
- [129] M.I. Mendeleev, M. Asta, M.J. Rahman, J.J. Hoyt, Development of interatomic potentials appropriate for simulation of solid-liquid interface properties in Al-Mg alloys, *Philosophical Magazine*, 89(34-36) (2009) 3269-3285.
- [130] A. Stukowski, Visualization and analysis of atomistic simulation data with OVITO—the Open Visualization Tool, *Modelling and Simulation in Materials Science and Engineering*, 18(1) (2010) 015012.
- [131] F.D.D.T. Jakob Schiøtz, Karsten W. Jacobsen, Softening of nanocrystalline metals at very small grain sizes, *Nature*, 391 (1998) 561-563.
- [132] A. Stukowski, K. Albe, Extracting dislocations and non-dislocation crystal defects from atomistic simulation data, *Modelling and Simulation in Materials Science and Engineering*, 18(8) (2010) 085001.
- [133] A.M. L.P. Kubin, Geometrically necessary dislocations and strain-gradient plasticity a few critical issues., *Scripta Materialia*, 48 (2003) 119-125.

- [134] D.M. Dimiduk, M.D. Uchic, T.A. Parthasarathy, Size-affected single-slip behavior of pure nickel microcrystals, *Acta Materialia*, 53(15) (2005) 4065-4077.
- [135] A. Kunz, S. Pathak, J.R. Greer, Size effects in Al nanopillars: Single crystalline vs. bicrystalline, *Acta Materialia*, 59(11) (2011) 4416-4424.
- [136] J.A. El-Awady, C. Woodward, D.M. Dimiduk, N.M. Ghoniem, Effects of focused ion beam induced damage on the plasticity of micropillars, *Physical Review B*, 80(10) (2009).
- [137] D. Kiener, C. Motz, M. Rester, M. Jenko, G. Dehm, FIB damage of Cu and possible consequences for miniaturized mechanical tests, *Mat Sci Eng A-Struct*, 459(1-2) (2007) 262-272.
- [138] A.T. Jennings, M.J. Burek, J.R. Greer, Microstructure versus size: mechanical properties of electroplated single crystalline Cu nanopillars, *Physical review letters*, 104(13) (2010) 135503.
- [139] S. Xu, Y.F. Guo, A.H.W. Ngan, A molecular dynamics study on the orientation, size, and dislocation confinement effects on the plastic deformation of Al nanopillars, *International Journal of Plasticity*, 43 (2013) 116-127.
- [140] A.B. Hagen, B.D. Snartland, C. Thaulow, Temperature and orientation effects on the deformation mechanisms of α -Fe micropillars, *Acta Materialia*, 129 (2017) 398-407.
- [141] C.P. Frick, B.G. Clark, S. Orso, A.S. Schneider, E. Arzt, Size effect on strength and strain hardening of small-scale [111] nickel compression pillars, *Materials Science and Engineering: A*, 489(1-2) (2008) 319-329.
- [142] A.S. Schneider, C.P. Frick, B.G. Clark, P.A. Gruber, E. Arzt, Influence of orientation on the size effect in bcc pillars with different critical temperatures, *Materials Science and Engineering: A*, 528(3) (2011) 1540-1547.

- [143] K.S. Ng, A.H.W. Ngan, Breakdown of Schmid's law in micropillars, *Scripta Materialia*, 59(7) (2008) 796-799.
- [144] Ø.G. O. R. Myhr, S. J. Andersen, Modelling of the age hardening behaviour of Al–Mg–Si alloys, *Acta Materialia*, 49 (2001) 65-75.
- [145] D.R. F. Roters, G. Gottstein, Work hardening in heterogeneous alloys—a microstructural approach based on three internal state variables, *Acta Materialia*, 48 (2000) 4181-4189.
- [146] C. Varvenne, G.P.M. Leyson, M. Ghazisaeidi, W.A. Curtin, Solute strengthening in random alloys, *Acta Materialia*, 124 (2017) 660-683.
- [147] W.S. Choi, B.C. De Cooman, S. Sandlöbes, D. Raabe, Size and orientation effects in partial dislocation-mediated deformation of twinning-induced plasticity steel micropillars, *Acta Materialia*, 98 (2015) 391-404.
- [148] J. Gong, T. Benjamin Britton, M.A. Cuddihy, F.P.E. Dunne, A.J. Wilkinson, $\langle a \rangle$ Prismatic, $\langle a \rangle$ basal, and $\langle c+a \rangle$ slip strengths of commercially pure Zr by microcantilever tests, *Acta Materialia*, 96 (2015) 249-257.
- [149] J. Gong, A.J. Wilkinson, A microcantilever investigation of size effect, solid-solution strengthening and second-phase strengthening for $\langle a \rangle$ prism slip in alpha-Ti, *Acta Materialia*, 59(15) (2011) 5970-5981.
- [150] B.D. Wirth, How does radiation damage, *Science*, 318 (2007) 923.
- [151] X. Xiao, D. Song, J. Xue, H. Chu, H. Duan, A size-dependent tensorial plasticity model for FCC single crystal with irradiation, *International Journal of Plasticity*, 65 (2015) 152-167.
- [152] R. Soler, J.M. Molina-Aldareguia, J. Segurado, J. Llorca, R.I. Merino, V.M. Orera, Micropillar compression of LiF [111] single crystals: Effect of size, ion irradiation and misorientation, *International Journal of Plasticity*, 36 (2012) 50-63.

- [153] S. Lee, J. Jeong, Y. Kim, S.M. Han, D. Kiener, S.H. Oh, FIB-induced dislocations in Al submicron pillars: Annihilation by thermal annealing and effects on deformation behavior, *Acta Materialia*, 110 (2016) 283-294.
- [154] D.M.D. M.D.Uchic, J.N.Florando, W.D.Nix, Sample Dimensions Influence strength and crystalline plasticity, *Science*, 305(5686) (2004) 986-989.
- [155] K.F. Gan, A.H.W. Ngan, The unusual size effect of eutectic Sn/Pb alloys in the micro regime: Experiments and modeling, *Acta Materialia*, 151 (2018) 282-292.
- [156] S.I. Rao, D.M. Dimiduk, T.A. Parthasarathy, M.D. Uchic, M. Tang, C. Woodward, Athermal mechanisms of size-dependent crystal flow gleaned from three-dimensional discrete dislocation simulations, *Acta Materialia*, 56(13) (2008) 3245-3259.
- [157] D.M. Norfleet, D.M. Dimiduk, S.J. Polasik, M.D. Uchic, M.J. Mills, Dislocation structures and their relationship to strength in deformed nickel microcrystals, *Acta Materialia*, 56(13) (2008) 2988-3001.
- [158] J.A. El-Awady, M. Wen, N.M. Ghoniem, The role of the weakest-link mechanism in controlling the plasticity of micropillars, *Journal of the Mechanics and Physics of Solids*, 57(1) (2009) 32-50.
- [159] A.A. Benzerga, An analysis of exhaustion hardening in micron-scale plasticity, *International Journal of Plasticity*, 24(7) (2008) 1128-1157.
- [160] J.R. Greer, W.D. Nix, Nanoscale gold pillars strengthened through dislocation starvation, *Physical Review B*, 73(24) (2006).
- [161] S.-W. Lee, S.M. Han, W.D. Nix, Uniaxial compression of fcc Au nanopillars on an MgO substrate: The effects of prestraining and annealing, *Acta Materialia*, 57(15) (2009) 4404-4415.
- [162] K.S. Ng, A.H.W. Ngan, Stochastic nature of plasticity of aluminum micro-pillars, *Acta Materialia*, 56(8) (2008) 1712-1720.

- [163] K.S. Ng, A.H.W. Ngan, Effects of trapping dislocations within small crystals on their deformation behavior, *Acta Materialia*, 57(16) (2009) 4902-4910.
- [164] R. Soler, A. Evirgen, M. Yao, C. Kirchlechner, F. Stein, M. Feuerbacher, D. Raabe, G. Dehm, Microstructural and mechanical characterization of an equiatomic YGdTbDyHo high entropy alloy with hexagonal close-packed structure, *Acta Materialia*, 156 (2018) 86-96.
- [165] K.S. Ng, A.H.W. Ngan, Deformation of micron-sized aluminium bi-crystal pillars, *Philosophical Magazine*, 89(33) (2009) 3013-3026.
- [166] X.W. Gu, C.N. Loynachan, Z. Wu, Y.W. Zhang, D.J. Srolovitz, J.R. Greer, Size-dependent deformation of nanocrystalline Pt nanopillars, *Nano Lett*, 12(12) (2012) 6385-6392.
- [167] B. Jelinek, S. Groh, M.F. Horstemeyer, J. Houze, S.G. Kim, G.J. Wagner, A. Moitra, M.I. Baskes, Modified embedded atom method potential for Al, Si, Mg, Cu, and Fe alloys, *Physical Review B*, 85(24) (2012).
- [168] P. Zhang, O.U. Salman, J.-Y. Zhang, G. Liu, J. Weiss, L. Truskinovsky, J. Sun, Taming intermittent plasticity at small scales, *Acta Materialia*, 128 (2017) 351-364.
- [169] S.-H. Li, W.-Z. Han, J. Li, E. Ma, Z.-W. Shan, Small-volume aluminum alloys with native oxide shell deliver unprecedented strength and toughness, *Acta Materialia*, 126 (2017) 202-209.
- [170] T. Hu, L. Jiang, H. Yang, K. Ma, T.D. Topping, J. Yee, M. Li, A.K. Mukherjee, J.M. Schoenung, E.J. Lavernia, Stabilized plasticity in ultrahigh strength, submicron Al crystals, *Acta Materialia*, 94 (2015) 46-58.
- [171] Q. Li, S. Xue, J. Wang, S. Shao, A.H. Kwong, A. Giwa, Z. Fan, Y. Liu, Z. Qi, J. Ding, H. Wang, J.R. Greer, H. Wang, X. Zhang, High-Strength Nanotwinned Al Alloys with 9R Phase, *Adv Mater*, 30(11) (2018).

- [172] K. Gan, R. Gu, A.H.W. Ngan, The weakest size of precipitated alloys in the micro-regime: The case of duralumin, *Journal of Materials Research*, 32(11) (2017) 2003-2013.
- [173] A.S. Schneider, D. Kiener, C.M. Yakacki, H.J. Maier, P.A. Gruber, N. Tamura, M. Kunz, A.M. Minor, C.P. Frick, Influence of bulk pre-straining on the size effect in nickel compression pillars, *Materials Science and Engineering: A*, 559 (2013) 147-158.
- [174] J.A. El-Awady, M.D. Uchic, P.A. Shade, S.-L. Kim, S.I. Rao, D.M. Dimiduk, C. Woodward, Pre-straining effects on the power-law scaling of size-dependent strengthening in Ni single crystals, *Scripta Materialia*, 68(3-4) (2013) 207-210.
- [175] A.S. Schneider, B.G. Clark, C.P. Frick, P.A. Gruber, E. Arzt, Effect of pre-straining on the size effect in molybdenum pillars, *Philosophical Magazine Letters*, 90(11) (2010) 841-849.
- [176] R. Gu, A.H.W. Ngan, Effects of pre-straining and coating on plastic deformation of aluminum micropillars, *Acta Materialia*, 60(17) (2012) 6102-6111.
- [177] J.A. El-Awady, Unravelling the physics of size-dependent dislocation-mediated plasticity, *Nat Commun*, 6 (2015) 5926.
- [178] Q. Jiao, G.-D. Sim, M. Komarasamy, R.S. Mishra, P.K. Liaw, J.A. El-Awady, Thermo-mechanical response of single-phase face-centered-cubic Al_xCoCrFeNi high-entropy alloy microcrystals, *Materials Research Letters*, 6(5) (2018) 300-306.
- [179] J.A. El-Awady, Unravelling the physics of size-dependent dislocation-mediated plasticity, *Nature Communications*, 6(1) (2015).
- [180] F. Roters, P. Eisenlohr, C. Kords, D.D. Tjahjanto, M. Diehl, D. Raabe, DAMASK: the Düsseldorf Advanced MATERIAL Simulation Kit for studying crystal plasticity using an FE based or a spectral numerical solver, *Procedia IUTAM*, 3 (2012) 3-10.

- [181] D. Raabe, D. Ma, F. Roters, Effects of initial orientation, sample geometry and friction on anisotropy and crystallographic orientation changes in single crystal microcompression deformation: A crystal plasticity finite element study, *Acta Materialia*, 55(13) (2007) 4567-4583.
- [182] Q.H. Qin, *Fracture mechanics of piezoelectric materials*, WIT Press, Southampton, 2001.
- [183] Q.H. Qin, S.W. Yu, An arbitrarily-oriented plane crack terminating at the interface between dissimilar piezoelectric materials, *International Journal of Solids and Structures*, 34(5) (1997) 581-590.
- [184] Q.H. Qin, Y.-W. Mai, A closed crack tip model for interface cracks in thermopiezoelectric materials, *International Journal of Solids and Structures*, 36(16) (1999) 2463-2479.
- [185] S. Yu, Q.H. Qin, Damage analysis of thermopiezoelectric properties: Part I—crack tip singularities, *Theoretical and Applied Fracture Mechanics*, 25(3) (1996) 263-277.
- [186] Q.H. Qin, Y. Mai, Crack growth prediction of an inclined crack in a half-plane thermopiezoelectric solid, *Theoretical and Applied Fracture Mechanics*, 26(3) (1997) 185-191.
- [187] Q.H. Qin, Y.-W. Mai, S.-W. Yu, Some problems in plane thermopiezoelectric materials with holes, *International Journal of Solids and Structures*, 36(3) (1999) 427-439.
- [188] Q.H. Qin, Y.-W. Mai, S.-W. Yu, Effective moduli for thermopiezoelectric materials with microcracks, *International Journal of Fracture*, 91(4) (1998) 359-371.
- [189] H. Wang, Q.H. Qin, Hybrid FEM with fundamental solutions as trial functions for heat conduction simulation, *Acta Mechanica Solida Sinica*, 22(5) (2009) 487-498.

- [190] Q.H. Qin, Hybrid-Trefftz finite element method for Reissner plates on an elastic foundation, *Computer Methods in Applied Mechanics and Engineering*, 122(3-4) (1995) 379-392.
- [191] H. Wang, Q.H. Qin, A meshless method for generalized linear or nonlinear Poisson-type problems, *Engineering Analysis with Boundary Elements*, 30(6) (2006) 515-521.
- [192] H. Wang, Q.H. Qin, Meshless approach for thermo-mechanical analysis of functionally graded materials, *Engineering Analysis with Boundary Elements*, 32(9) (2008) 704-712.
- [193] A. Jérusalem, A. Fernández, A. Kunz, J.R. Greer, Continuum modeling of dislocation starvation and subsequent nucleation in nano-pillar compressions, *Scripta Materialia*, 66(2) (2012) 93-96.
- [194] B.E. Schuster, Q. Wei, T.C. Hufnagel, K.T. Ramesh, Size-independent strength and deformation mode in compression of a Pd-based metallic glass, *Acta Materialia*, 56(18) (2008) 5091-5100.
- [195] R. Quey, P.R. Dawson, F. Barbe, Large-scale 3D random polycrystals for the finite element method: Generation, meshing and remeshing, *Computer Methods in Applied Mechanics and Engineering*, 200(17-20) (2011) 1729-1745.
- [196] D. Kupka, N. Huber, E.T. Lilleodden, A combined experimental-numerical approach for elasto-plastic fracture of individual grain boundaries, *Journal of the Mechanics and Physics of Solids*, 64 (2014) 455-467.
- [197] H. Ghassemi-Armaki, P. Chen, S. Bhat, S. Sadagopan, S. Kumar, A. Bower, Microscale-calibrated modeling of the deformation response of low-carbon martensite, *Acta Materialia*, 61(10) (2013) 3640-3652.

- [198] C.K. M. Asmani, A. Leriche, M. Ourak, Influence of porosity on Young's modulus and Poisson's ratio in alumina ceramics, *Journal of European Ceramic Society*, 21 (2001) 1081-1086.
- [199] R.S. J. Luo, Porosity-dependence of elastic moduli and hardness of 3Y-TZP ceramics, *Ceramics International*, 25 (1999) 281-286.
- [200] Q. Wang, H. Chen, P. Qiu, Z. Zhu, Residual Stress and Fatigue Strength of Hybrid Laser-MIG-Welded A7N01P-T4, *Metallurgical and Materials Transactions B*, 48(1) (2016) 591-601.
- [201] X. Cheng, Residual stress modification by post-weld treatment and its beneficial effect on fatigue strength of welded structures, *International Journal of Fatigue*, 25(9-11) (2003) 1259-1269.

List of publications

1. **Shaohua Yan**, Hui Chen, Chuanping Ma, Yuan Nie, Xiaomin Wang, Qing-Hua Qin. Local corrosion behavior of hybrid laser-MIG welded Al-Zn-Mg alloys joint. *Materials and Design* 61 (2015) 160-167.
2. Bobin Xing, **Shaohua Yan**, Wugui Jiang, Qing Hua Qin. Atomistic study for the vibrational properties on $\Sigma 5$ symmetric tilt bicrystal copper nanowires. *Applied Mechanics and Materials* 846 (2016) 193-198.
3. Bobin Xing, **Shaohua Yan**, Wugui Jiang, and Qing H. Qin. Deformation mechanism of kink-step distorted coherent twin boundaries in copper nanowire. *AIMS Materials Science*, 4(2016): 102-117.
4. Xing B., **Yan S.**, Jiang W., & Qin Q. Effect of Inclination Angle on Mechanical Behaviour and Deformation Asymmetry in Aluminium Bicrystal. *Journal of Integrated Design and Process Science*. DOI 10.3233/jid-2017-0009.
5. **Shaohua Yan**, Bobin Xing, Haiyang Zhou, Yi Xiao, Qing. H Qin, Hui Chen. Effect of filling materials on the microstructure and properties of hybrid laser welded Al-Mg-Si alloys joints. *Materials Characterization* 144 (2018) 205-218.
6. Bobin Xing, **Shaohua Yan**, Haiyang Zhou, Hua Chen, Qing Hua Qin. Qualitative and quantitative analysis of misaligned electrode degradation when welding galvanized steel. *The International Journal of Advanced Manufacturing Technology* 97 (2018) 629-640.
7. **Shaohua Yan**, Haiyang Zhou, Bobin Xing, Shuang Zhang, Li Li, Qing .H Qin. Crystal plasticity of fusion zone in a hybrid laser welded Al alloys joint: from nanoscale to macroscale. *Materials and Design* 160 (2018) 313-324.

8. *Shaohua Yan*, Haiyang Zhou, Qinghua Qin. Microstructure versus size: nano/microscale deformation of solute-strengthening Al alloys via pillar compression tests. *Materials Research Letters* 7 (2019) 53-59.
9. *Shaohua Yan*, Haiyang Zhou, Zheng Zhong, Qing. H. Qin. Bridging the gap between microscale and macroscale crystal plasticity of arc-laser welded joints: experiment and simulation. (Submitted).